

# Type Ia Supernovae: Explosions and Progenitors

Wolfgang Eitel Kerzendorf

A thesis submitted for the degree of

Doctor of Philosophy

of The Australian National University



Australian  
National  
University

Research School of Astronomy and Astrophysics  
The Australian National University  
Canberra ACT 0200  
Australia

July 2011

## **Disclaimer**

I hereby declare that the work in this thesis is that of the candidate alone, except where indicated below or in the text of the thesis.

Wolfgang E. Kerzendorf

29th July 2011

## Acknowledgments

  Lorem ipsum dolor sit amet, consectetur adipiscing elit. Donec tincidunt semper neque. Cum sociis natoque penatibus et magnis dis parturient montes, nascetur ridiculus mus. Donec cursus velit ut felis. Quisque tellus. Curabitur in leo. Suspendisse volutpat. Nunc sodales sagittis magna. In vehicula viverra elit. Donec dapibus cursus mauris. Maecenas volutpat, sapien eu dictum molestie, mi lectus tristique augue, eu lobortis tellus nisi nec urna. Phasellus at est nec odio ultricies consequat. Nam eu urna.

  Duis tempus imperdiet nunc. Integer vitae lorem. Sed id pede eu turpis rhoncus semper. Curabitur ante leo, facilisis vitae, interdum mollis, fermentum et, ipsum. Phasellus scelerisque, arcu et varius venenatis, lacus magna semper mauris, et aliquet augue nulla hendrerit libero. Suspendisse nec turpis et nisl congue posuere. Mauris sagittis ipsum nec lectus. Vestibulum nisl. Quisque ante. Nam accumsan, metus eu lobortis laoreet, massa velit elementum urna, ac tristique eros justo sit amet mauris. Vestibulum at arcu hendrerit massa placerat tristique. In magna velit, vestibulum eget, viverra ut, facilisis id, lectus. Cras justo lorem, varius non, tristique sit amet, lobortis nec, neque. Aenean cursus congue metus. Vestibulum id magna.

## **Abstract**

Lorem ipsum dolor sit amet, consectetuer adipiscing elit. Donec tincidunt semper neque. Cum sociis natoque penatibus et magnis dis parturient montes, nascetur ridiculus mus. Donec cursus velit ut felis. Quisque tellus. Curabitur in leo. Suspendisse volutpat. Nunc sodales sagittis magna. In vehicula viverra elit. Donec dapibus cursus mauris. Maecenas volutpat, sapien eu dictum molestie, mi lectus tristique augue, eu lobortis tellus nisi nec urna. Phasellus at est nec odio ultricies consequat. Nam eu urna.

Duis tempus imperdiet nunc. Integer vitae lorem. Sed id pede eu turpis rhoncus semper. Curabitur ante leo, facilisis vitae, interdum mollis, fermentum et, ipsum. Phasellus scelerisque, arcu et varius venenatis, lacinia magna semper mauris, et aliquet augue nulla hendrerit libero. Suspendisse nec turpis et nisl congue posuere. Mauris sagittis ipsum nec lectus. Vestibulum nisl. Quisque ante. Nam accumsan, metus eu lobortis laoreet, massa velit elementum urna, ac tristique eros justo sit amet mauris. Vestibulum at arcu hendrerit massa placerat tristique. In magna velit, vestibulum eget, viverra ut, facilisis id, lectus. Cras justo lorem, varius non, tristique sit amet, lobortis nec, neque. Aenean cursus congue metus. Vestibulum id magna.



---

# Contents

Disclaimer . . . . .	i
Abstract . . . . .	iii
<b>1 Introduction</b>	<b>1</b>
1.1 Ancient Supernovae . . . . .	1
1.2 Modern day supernova observations and surveys . . . . .	3
1.3 Observational Properties of Supernovae . . . . .	5
1.3.1 Supernova classification . . . . .	5
1.3.2 Supernova rates . . . . .	9
1.3.3 Light curves . . . . .	10
1.3.4 Spectra . . . . .	11
SNe Ia spectra . . . . .	12
SNe II Spectra . . . . .	14
1.3.5 X-Ray & Radio observations . . . . .	14
1.3.6 Supernova Cosmology . . . . .	14
1.4 Post-explosion observations of Supernovae . . . . .	16
1.5 Core-Collapse Supernova Theory . . . . .	18
1.5.1 Evolution of Massive Stars . . . . .	18
1.5.2 Core collapse . . . . .	19
1.5.3 Pair instability . . . . .	20
1.5.4 Type II Supernovae . . . . .	20
1.5.5 Type Ib/c supernovae . . . . .	21
1.6 Thermonuclear Supernova Theory . . . . .	21
1.6.1 White Dwarfs . . . . .	21

1.6.2	Pre-supernova evolution . . . . .	22
1.7	Progenitors of Type Ia Supernovae . . . . .	25
1.7.1	Single Degenerate Scenario . . . . .	25
	Accretion . . . . .	25
	Donor Stars . . . . .	26
1.7.2	Double Degenerate Scenario . . . . .	26
1.7.3	Constrains for different progenitor scenarios . . . . .	27
1.8	Thesis motivation . . . . .	29
<b>2</b>	<b>SN1572</b>	<b>31</b>
2.1	Introduction . . . . .	31
2.2	Observational Characteristics of the Tycho Remnant and Star-G . . . . .	33
2.3	Rapid Rotation: A Key Signature in SN Ia Donor Stars . . . . .	34
2.4	Subaru Observations . . . . .	36
2.5	Analysis and Results . . . . .	37
2.5.1	Rotational measurement . . . . .	37
2.5.2	Radial velocity . . . . .	37
2.5.3	Astrometry . . . . .	38
2.6	Discussion . . . . .	40
2.6.1	A Background interloper? . . . . .	40
2.6.2	Tycho-G as the Donor Star to the Tycho SN . . . . .	42
2.7	Outlook and Future Observations . . . . .	44
<b>3</b>	<b>Tycho's Six: High-Resolution spectroscopy search for the remaining donor for the Tycho supernova</b>	<b>47</b>
3.1	Introduction . . . . .	47
3.2	Observations and Data Reduction . . . . .	49
3.3	Analysis . . . . .	50
3.3.1	Astrometry . . . . .	50
3.3.2	Radial Velocity . . . . .	52
3.3.3	Rotational Velocity . . . . .	52
3.3.4	Stellar parameters . . . . .	53
3.3.5	Distance . . . . .	57
3.4	Discussion . . . . .	59
3.5	Conclusion . . . . .	60
3.6	Acknowledgments . . . . .	61
3.7	Line list . . . . .	61

<b>4 SN1006</b>	<b>63</b>
4.1 Introduction . . . . .	63
4.2 Observations and Data Reduction . . . . .	64
4.3 Analysis . . . . .	66
4.3.1 Photometry . . . . .	66
4.3.2 Proper motion . . . . .	66
4.3.3 Radial Velocity . . . . .	66
4.3.4 Rotational Velocity . . . . .	68
4.3.5 Stellar Parameters . . . . .	70
4.4 Conclusions . . . . .	71
<b>5 Automatic fitting of optical Type Ia Supernova spectra - the Dalek code</b>	<b>73</b>
5.1 The MLMC-Code . . . . .	74
5.1.1 Radiative Transfer . . . . .	74
5.1.2 Monte Carlo radiative transfer . . . . .	76
5.2 Manually fitting a Type Ia supernova . . . . .	77
5.3 Genetic Algorithms . . . . .	82
5.3.1 A simple example . . . . .	87
5.3.2 Convergence in Genetic Algorithms . . . . .	88
5.3.3 GA theory schemata theory . . . . .	88
5.4 Genetic Algorithms to fit Type Ia Supernovae: The Dalek Code . . . . .	89
5.4.1 The Dalek Code . . . . .	89
5.5 Conclusion . . . . .	94
<b>6 Conclusions and Future Work</b>	<b>97</b>
6.1 Single or Double Degenerate? . . . . .	97
6.2 The curious case of Kepler . . . . .	98
6.3 Divide et impera . . . . .	99
6.4 Dalek . . . . .	100
6.5 Trouble in Paradise . . . . .	100
<b>A Linear interpolation in N Dimensions</b>	<b>115</b>
A.1 Delauney triangulation . . . . .	116
A.2 Convex Hull . . . . .	117
A.3 Barycentric coordinates system . . . . .	119
A.4 Triangle Finding and Interpolation . . . . .	119
A.5 Conclusion . . . . .	120



---

# List of Figures

1.1	Chaco canyon petroglyphs show a hand, a moon and a bright celestial object. This could be SN1054 but it is ambiguous. (Source Wikipedia/ Photographer jamesdale10/ Creative Commons license)	2
1.2	<i>"I have indeed measured the distance of this star from some of the fixed stars in the constellation of Cassiopeia several times with an exquisit (optical) instrument, which is capable of all the fine details of measurement. I have further detected that it (the new star) is located 7 degrees and 55 minutes from the star at the breast of the Schedir designated by B."</i> translation kindly provided by Leonhard Kretzenbacher	3
1.3	.....	6
1.4	example caption	6
1.5	Estimated fractions for different SN Ia-classes for a purely magnitude limited search. Adapted from Li et al. (2011)	7
1.6	Lightcurve data taken from Li et al. (2011) templates. The time is relative to maximum light and the magnitude is the difference between maximum	8
1.7	Estimated fractions for different SN II-classes for a purely magnitude limited search. Adapted from Li et al. (2011)	8
1.8	The plot shows the estimated supernova rate per unit mass in different galaxy morphologies (Mannucci et al., 2005). ???Explain morphology ??? There have been no detections of SNe Ib/c and SNe II in old elliptical galaxies which suggests that these types only occur in galaxies with recent star-formation.	9
1.9	Lightcurves of SN 2002bo (data from Benetti et al., 2004)	11
1.10	Premaximum evolution of SN 2003du spectra from Tanaka et al. (2011).	12
1.11	Postmaximum evolution of SN 2003du from Tanaka et al. (2011).	13
1.12	example caption	13

1.13 Replace with some data. any suggestions . . . . .	16
1.14 Shell Burning of a massive star before SN II. (Source Wikipedia, Creative Commons License) . . . . .	18
1.15 Delayed detonation simulation from Röpke & Bruckschen (2008). The upper panels show the deflagrated interior (marked in blue) and the detonation ignition point (small white sphere). The detonation wave wraps around the deflagration ash and consumes the cold fuel. (Image reproduced with kind permission of Fritz Röpke) . . . . .	23
1.16 The ignition point of the helium shell is marked in the upper left image. We can follow the helium shell sending shock waves into the core of the white dwarf. They converge in the lower left image at the opposite site of the Carbon/Oxygen core (data from Fink et al., 2010, figure kindly provided by Michael Fink) . . . . .	24
2.1 Radio Contours (VLA Project AM0347) have been overlaid (Gooch, 1996) on an R-Band Image (NGS-POSS). The cutout is an INT image (see text). The stars marked in the figure are mentioned in this work and in RP04's work.	33
2.2 The expected rotation rate for a donor star as a function of its mass at the time of the explosion. The three curves show the results for 3 final space velocities of the donor star (similar to those suggested by RP04). It is assumed that the white dwarf has a mass of $1.4 M_{\odot}$ . . . . .	35
2.3 Six observed Fe I line profiles of Tycho-G are shown on the left panel. The right panel shows the combination of these line profiles after normalization to the same equivalent width and compares them to the spectrum of the Sun, which is convolved with 3 different values for the rotational broadening kernel. Tycho-G does not show significant rotation, indicating $v_{\text{rot}} \sin i \lesssim 7.5 \text{ km s}^{-1}$ . . . . .	37
2.4 The astrometric motions of 60 stars measured in the Tycho SNR center. The measurements have a RMS dispersion of $1.6 \text{ mas yr}^{-1}$ . Shown in grey is the proper motion of Tycho-G measured here and by RP04, showing a moderate discrepancy in the two measurements. Our measurement is consistent with no proper motion. . . . .	40
2.5 Besançon model for a metal rich ( $[\text{Fe}/\text{H}] > -0.2$ ) Galactic population between 0 and 7 kpc in the direction of Tycho SNR ( $l = 120.1$ , $b = 1.4$ ) with a solid angle of 1 square degree. The remnant's distance is represented by the black dashed lines (as calculated in section 2.2). The contours show the radial velocity distribution. Our measured radial velocity corrected to LSR and our distance are shown, with their respective error ranges, as the black rectangle. The distance range calculated by GH09 are indicated by the two solid lines. The observed LSR $v_r$ for Tycho-G is mildly unusual for stars at the remnant's distance, and is consistent with the bulk of stars behind the remnant. . . . .	41

3.1	The contours show the distribution of proper motion ( $1 - \sigma$ and $2 - \sigma$ ) excluding the named stars. We show the location of the candidate stars and their errors on top of this distribution. Tycho-2 was not shown in this figure as it is an extreme outlier with $\mu_\alpha = 75 \text{ mas yr}^{-1}$ and $\mu_\delta = -4.4 \text{ mas yr}^{-1}$ but also at a large distance to the center of the remnant's geometric center (46'').	51
3.2	The contours indicate 1, 2 and $3 - \sigma$ levels of the distance and radial velocity using the Besançon Model (Robin et al., 2003) with $\approx 60000$ stars in the direction of SNR1572 (only including star with a V between 10 and 20 as well as stars with a metallicity of $[\text{Fe}/\text{H}] > -1$ ). We have overplotted our candidate stars with error bars. One should note that the errors in distance are only an indication of the error, the proper error surfaces can be seen in Figure 3.6. The vertical gray shade shows the error range for the distance of SNR1572.	53
3.3	The figures show the combination of Fe-line profiles after normalization to the same equivalent width and compare them to synthetic line profiles created by MOOG. We convolved the synthetic lines first with a rotational kernel with three different values for rotation and then with the instrumental profile. All stars show rotation less than $6 \text{ km s}^{-1}$ which is equal to the instrumental profile at this resolution.	54
3.4	The background colour indicates the distribution is taken from Kobayashi et al. (2006). All of the measured candidates are consistent within the errors with stars of the same metallicity.	55
3.5	The plot shows the normalized spectrum of Tycho-B with the fit which excluded the spectral region between $3800 - 4500 \text{ \AA}$ (Best Fit 1) and the fit with the problematic region (Best Fit 2). The region is marked with a gray shade.	57
3.6	The figures show error contours for distance, extinction and mass of the candidates. The lower right shows the optimal isochrone (Pietrinferni et al., 2004) for the measured values of $T_{\text{eff}}$ and $\log g$ .	58
4.1	example caption	64
4.2	example caption	69
5.1	Spectrum of SN 2002bo (Benetti et al., 2004) with MLMC-fit by Hachinger (2007). The excess in redwards of $6500 \text{ \AA}$ is a common problematic features of these fits.	77
5.2	We have perturbed the luminosity around the best fit value. The most noticeable effect is the continuum offset. There is also a slight change in the overall slope of the spectrum.	79
5.3	The photospheric velocity has been perturbed around the bestfit. The slope of the spectrum changes a too small velocity produces a hot blue spectrum, a too large velocity a cold red spectrum.	79

5.4	When changing the IGE (in this case we have only changed iron and Nickel) the flux is altered in the blue and red part. Too much IGE's and there's not enough flux in the blue and too much flux in the red and vice versa. . . . .	80
5.5	We have identified some of the strongest lines that are scrutinized when fitting a SN Ia spectrum. . . . .	81
5.6	The death of the TSP with the advent of online sales. (reproduced with kind permission by xkcd.com) . . . . .	84
5.7	The individual fitnesses are assigned proportional fractions on the roulette wheel. The wheel is then spun and will slowly decelerate and stop at some point. Individuals with a higher fitness have a higher chance of being chosen with this method. . . . .	86
5.8	We assign new fitness values to individuals before assigning them probabilities on the roulette wheel. The fitnesses are assigned by location in an ordered list. The least fit individual gets assigned the value 1 the fittest individual the number $n$ , where $n$ is the population size. This is can be viewed as a special case of fitness scaling. After the new fitnesses have been chosen we use normal roulette wheel selection to select for the mating pool in the population. . . . .	87
5.9	In the single crossover a random point in the Individual is chosen. Before this point the genes are taken from the first parent and after that we use the genes from the second parent. Using the same random number it easily allows for the creation of two children by reversing the roles of first and second parent. The multi-point crossover employs multiple places in the genome where the crossover happens. . . . .	87
5.10	Estimated initial guess for photospheric velocity against days after explosion.	90
5.11	Evolution of fitness of in the generations. In later generations there is a clear divide between the members that have advanced through elitism and the bulk of the population. This suggests a too high mutationrate or the convergence of the algorithm. . . . .	93
5.12	The evolution of both luminosity and photospheric velocity shows that even at late phases of the algorithm there are still new combination that are being trialled. The very quick convergence in both cases however is a bit worrisome and will be analysed in future experiments. . . . .	93
5.13	The best individual of the first generation (left) and the best individual after 185 generations (right). This initial result demonstrates that GAs are able to conquer this problem. A more stable convergence and thorough exploration of the parameter space is however necessary to use this technique on a set of supernova spectra. . . . .	94
6.1	Overview of inner region of the remnant of SN1572. All labelled stars except Star-A2 have existing high-resolution spectra. Tycho-A2 is located very close to Tycho-A ( $0.6''$ ). Spectroscopy can only be obtained with adaptive optics in the infrared. . . . .	98

6.2	VLA contours of Kepler's remnant (SN1604) overlayed on a 2MASS image. The red rectangle show the overlapping north and south field of our WiFeS observing campaign. . . . .	99
A.1	Delauney Triangulation of 20 points in two dimensions. . . . .	116
A.2	The left figure shows an " <i>illegal</i> " triangulation of the 4 points. Both circles include all the points. With a so called edge flip one can arrive at a " <i>legal</i> " triangulation. . . . .	117
A.3	Stereogram (produced using a method described in <a href="#">Vogt &amp; Wagner, 2011</a> ) of the projection of the convex hull in three dimensions to form the delauney triangulation in two dimensions. . . . .	117
A.4	Determination of a convex hull in two dimensions. . . . .	118
A.5	The triangle and its barycenter marked by the intersection of lines. . . . .	119



---

# List of Tables

2.1	Proper motions of stars within 45'' of the Tycho SNR center.	39
3.1	Observations of Stars	49
3.2	Proper motion of Candidates	51
3.3	Radial velocities	52
3.4	Stellar Parameters	55
3.5	Tycho-B abundances	56
3.6	Distances, Ages and Masses of candidate stars	59
3.7	Measured equivalent widths from the Keck HIRES spectra	62
4.1	Flames Observations of SN1006 program stars	65
4.2	SN1006 photometry	67
4.2	SN1006 photometry	68
5.1	Abundance parameters for best fit	78



# CHAPTER 1

---

## Introduction

glossary add element description SDSS.

**F**OR millennia mankind has watched and studied the night sky. Apart from planets and comets it appeared an immutable canvas on which the stars rested. It comes as no surprise that for ancient civilizations supernovae (which were very rare events, occurring only every few centuries) were interpreted as important omens as they broke the paradigm of the unchanging night skies. As these events are so rare their origin remained a mystery until the middle of the last century. Baade & Zwicky (1934) suggested that "the phenomenon of a super-nova represents the transition of an ordinary star into a body of considerably smaller mass". For the last 85 years the "supernova-branch" in astronomy has been developing. There have been many advances, but there are still many unknowns. This work addresses two subfields of supernovae: The unsolved progenitor problem for Type Ia Supernovae as well as quantifying the nucleosynthetic yield and energies of Type Ia supernovae.

### 1.1. Ancient Supernovae

One of the earliest recorded supernovae is SN 185. It first appeared in December of 185 and was visible (however fading) till the August of 187. The main record is the *Houhanshu* (Zhao et al., 2006) which described SN 185 to be close to  $\alpha$  cen. Observational follow-up in modern times have revealed a supernova remnant in a distance of roughly 1 kpc near the  $\alpha$  cen (Zhao et al., 2006). SN 185 is often named as the oldest written record of a supernova, this however is sometimes contested as it is still not completely clear if the so called "guest star" was a comet or the supernova.

The oldest undisputed record of a supernova is SN 1006, which also coincides with the brightest ever recorded supernova. It was observed worldwide by asian, arabic and european astronomers. Goldstein (1965) gives a good summary of the observations and interpretation given by these ancient observers. Ali Ibn Ridwan was an Egyptian astronomer who recorded the appearance of SN 1006. He wrote in a comment on Ptolemy's Tetrabiblos: "*I will now describe for you a spectacle that saw at the beginning of my education.*

*This spectacle appeared in the zodiacal sign Scorpio in opposition to the sun, at which time the sun was in the 15th degree of Taurus, and the spectacle in the 15th degree of Scorpio. It was a large spectacle, round in shape and its size 2.5 or 3 times the magnitude of Venus. Its light illuminated the horizon and twinkled very much. . . This apparition was also observed at the time by (other) scholars just as I have recorded it."*

The next supernova happened only 50 years after SN 1006 in 1054. SN 1054, like SN 1006, was observed by many astronomers. One of the records is petroglyphs in the Chaco Canyon (see Figure 1.1) and was determined to have been produced around the time of the SN1054 explosion. It is still debated if SN1054 was the inspiration of the painting or the inspiration came from the passing of Hailey's comet in 1066. More than 900 years later Staelin & Reifenstein (1968) detected a pulsar in the center of SN1054. This was the first time that the stellar remnant of a supernova was found.

SN 1181 is a Galactic supernovae that has been mentioned in eight different texts by Chinese and Japanese astronomers. 3C58, a pulsar found in SN 1181, is suggested as the neutron star remnant of this stellar explosion.



**Figure 1.1** Chaco canyon petroglyphs show a hand, a moon and a bright celestial object. This could be SN1054 but it is ambiguous. (Source Wikipedia / Photographer jamesdale10 / Creative Commons license)

The supernova of 1572 has been reported by many astronomers. The most famous record, however, stems from the danish astronomer Tycho Brahe (Brahe & Kepler, 1602). The supernova was observed from November 1572 and monitored till March 1574 when it faded from visibility. Figure 1.2 shows the original chart produced by Tycho Brahe which shows the supernova in the constellation of Cassiopeia. Nearly 400 years later Hanbury Brown & Hazard (1952) discovered the radio emissions from the remnant of the SN1572.

32 years after the discovery of SN1572 Kepler and others observed SN1604 Kepler (1606) .

The supernova remained visible for about 18 month.

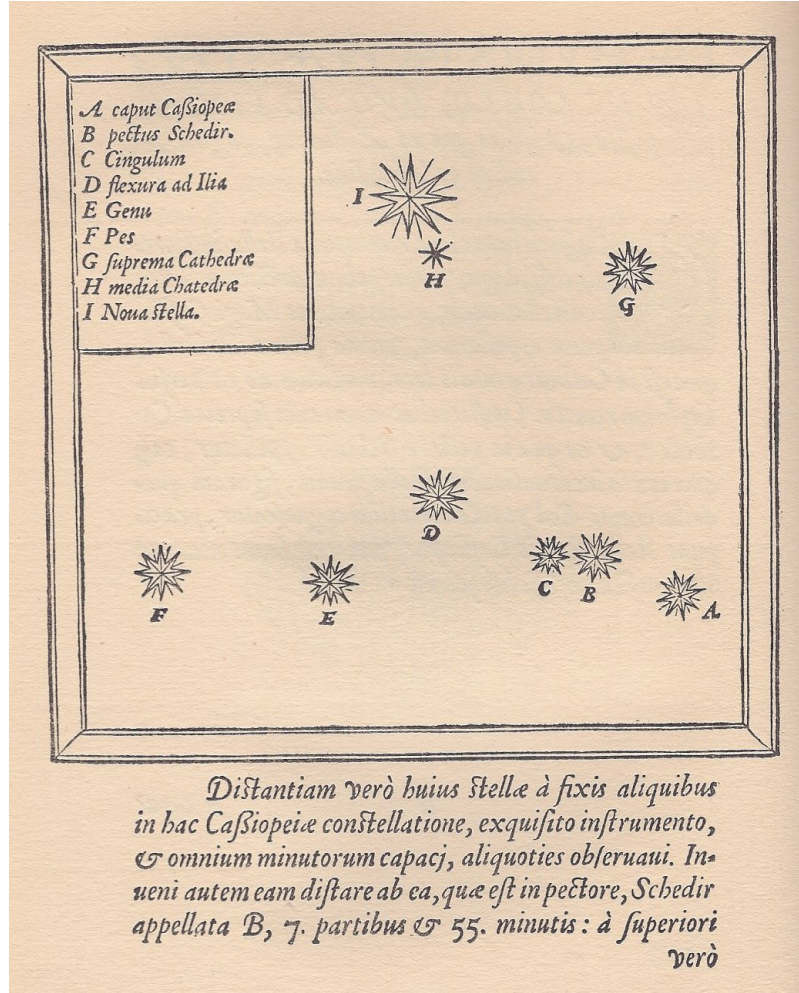


**Figure 1.2** “I have indeed measured the distance of this star from some of the fixed stars in the constellation of Cassiopeia several times with an exquisit (optical) instrument, which is capable of all the fine details of measurement. I have further detected that it (the new star) is located 7 degrees and 55 minutes from the star at the breast of the Schedir designated by B.” translation kindly provided by Leonhard Kretzenbacher

All of the ancient supernovae were observed only by the naked eye. Even in an era of 10-meter telescopes the records of these explosions remain useful.

## 1.2. Modern day supernova observations and surveys

The era of modern day supernova observations started with the discovery of SN 1885. SN 1885 (also known as S Andromedae) was first spotted by Isaac Ward in Belfast in August of 1885 ([Hartwig, 1885](#)) and was visible till February 1886. More than 50 years later [Baade & Zwicky \(1934\)](#) coined the term supernova and established the difference between common novae and supernovae. [Baade & Zwicky \(1934\)](#) also suggested that these luminous events are caused by the death of stars.

In order to understand the phenomenon of the supernova better, Zwicky began a supernova search with the 18-inch Schmidt telescope . Zwicky found several supernovae which in

turn inspired Minkowski to classify these supernovae by their spectra [Minkowski \(1941\)](#). He categorized the 14 known objects into two categories. Those without hydrogen he called 'Type I', those with hydrogen he called 'Type II' (see section [1.3.1](#) for a more detailed description about classification).

With the advent of affordable computing in the 1960s the first computer controlled telescopes were built. The 24-inch telescope was built by the Northwestern University and was deployed in Corralitos Observatory in New Mexico ([Colgate et al., 1975](#)). This search lead the way in computer controlled discovery and many later surveys would employ a similar design.

The Calán/Tololo supernova survey ([Hamuy et al., 1993](#)) ushered in the era of the modern automated supernova surveys in the 1990's. They provided a set of high-quality light curves and spectra of moderately distant ( $0.01 < z < 0.1$ ), where  $z$  means redshift, supernovae.

The Leuschner Observatory Supernova Survey began in 1992 followed shortly by the Berkeley Automatic Imaging Telescope (BAIT). These searches resulted in 15 supernovae by 1994 ([van Dyk et al., 1994](#)). One of the most well known discoveries is SN 1994D. This supernovae was observed with the Hubble Space Telescope and resulted in an image that is widely used today.

Having started in 1988 the supernova cosmology project (henceforth SCP) is the longest running supernova search which is still active today. Their main sample for the famous paper ([Perlmutter et al., 1999](#)) used the CTIO 4m telescope for discovery and many other telescopes for follow-up.

The High-Z team used the CTIO 4m telescope for discovery and follow-up of supernovae ([Schmidt et al., 1998](#)). Independently to SCP they discovered the accelerated expansion of the universe ([Riess et al., 1998](#)).

The Lick Observatory Supernova Search (LOSS) using the Katzman Automatic Imaging Telescope (KAIT) is one of the most successful supernovae searches. By the year 2000 it had found 96 supernovae ([Filippenko et al., 2001](#)).

After the turn of the millennium and following the discovery of the accelerated expansion of the universe a variety of groups started searching for supernovae and other transients. Among them were "The Equation of State: SupErNovae trace Cosmic Expansion (ESSENCE)"-project ([Garnavich et al., 2002](#)) and the Supernova Legacy Survey (SNLS) ([Pain & SNLS Collaboration, 2003](#)). Both these programs have either finished or are close to finishing.

Specialised surveys like the Nearby Supernova Factory ([Aldering et al., 2002](#)) and the Higher-z survey ([Strolger et al., 2004](#)) focused on a certain redshift range to obtain data on supernovae.

In recent years a multitude of large sky surveys has started (or are just about to). Some of these focus exclusively on transients and supernovae (e.g. PTF; [Rau et al., 2009](#)), whereas others like PanSTARRS ([Kaiser, 2004](#)) and SkyMapper ([Keller et al., 2007](#)) have a transient/supernova component. Upcoming surveys like the LSST [Pinto et al. \(2006\)](#) and the space-based GAIA mission [Perryman et al. \(2001\)](#) will provide unprecedented detail about current supernovae as well finding several new classes of transients.

In addition to the search in the optical new high-energy instruments like BATSE surveyed the sky from the beginning of the 1990's in gamma-rays. Meegan et al. (1992) showed that GRBs due to their isotropic distribution are events at cosmological distances rather than coming from our own Galaxy.

The Beppo-SAX satellite played a crucial role in resolving the origins of GRBs. The data from this mission was used to establish the connection between some GRBs and supernovae, the most famous example being GRB980425/SN 1998bw (Galama et al., 1998).

Among other discoveries the Hete-2 mission established a new class of transients called X-ray-flashes. These new objects are thought to be similar to GRBs in the physical nature but much less energetic (Zhang et al., 2004).

It was followed by the SWIFT telescope which provides, in addition to the gamma-ray-detector, an X-Ray telescope and UV/Optical telescope. It has been very successful at finding GRBs and providing targets for follow-up.

Almost all of the information about the universe we have deduced from observations of electro-magnetic waves. There are different physical phenomena which are much harder to observe than the electro-magnetic spectrum.

Gravitational waves, predicted by the theory of general relativity Einstein (1918), might provide us with another insight into supernovae. The most advanced detector today (LIGO Abramovici et al., 1992) has up till now not unambiguously detected gravitational waves. The sensitivity for this instrument is probably not low enough to detect these waves. Future instrumentation, like the impressive LISA-project (Jafry et al., 1994), are sensitive enough to detect the predicted gravitational waves. In the supernova field LISA might give us an estimate on the number of in-spiralling white dwarfs, which are suggested as progenitors of Type Ia supernovae (henceforth SNe Ia).

Bionta et al. (1987); Hirata et al. (1987); Alekseev et al. (1988) reported on neutrino detections from the very nearby supernova SN1987A. This was the first and last time that neutrino emission from a supernova was measured. New more sensitive detectors like ICECUBE (Karle, 2008) will hopefully enable us to do neutrino observations of more distant events.

For now the optical observations of supernovae provide the bulk of observations of these transients. Hopefully future instruments and capabilities will give us panchromatic observations as well as measurements from gravitational waves and particle fluxes. This will hopefully help to unlock more of the secrets of these still mysterious supernovae.

### 1.3. Observational Properties of Supernovae

#### 1.3.1. Supernova classification

The classification of supernovae started in the 1941 when Minkowski realized that there seem to be two main types (Minkowski, 1941). Those containing a hydrogen line (6563 Å) he called Type II supernovae and those showing no hydrogen he called Type I supernovae.

This basic classification has remained to this day, however the two main classes branched into several subclasses. During the 1980s the community discovered that most SNe Ia showed a broad Si II line at 6130 Å. There was, however, a distinct subclass of objects that

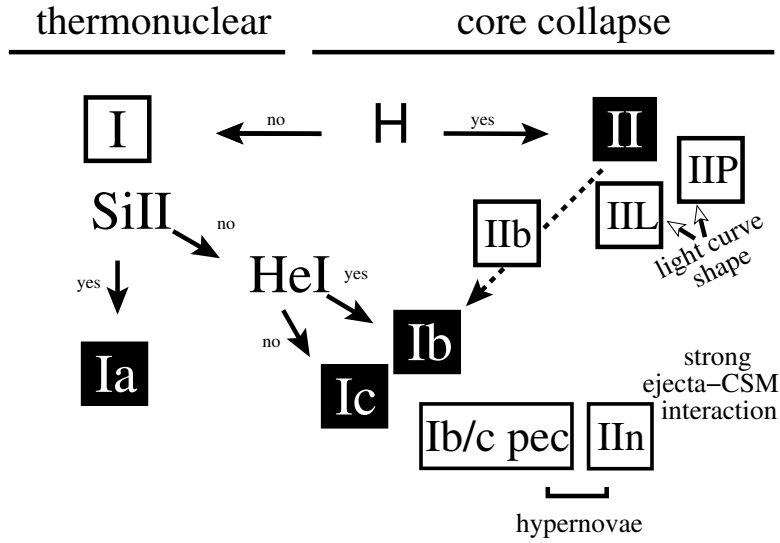


Figure 1.3

lacked this feature. These Silicon-less objects were then subclassed further into objects that showed helium – now known as Type Ib – and those that did not were called Type Ic (Harkness et al., 1987; Gaskell et al., 1986, see spectra in Figure 1.3). The classical Type I supernova was renamed to Type Ia.

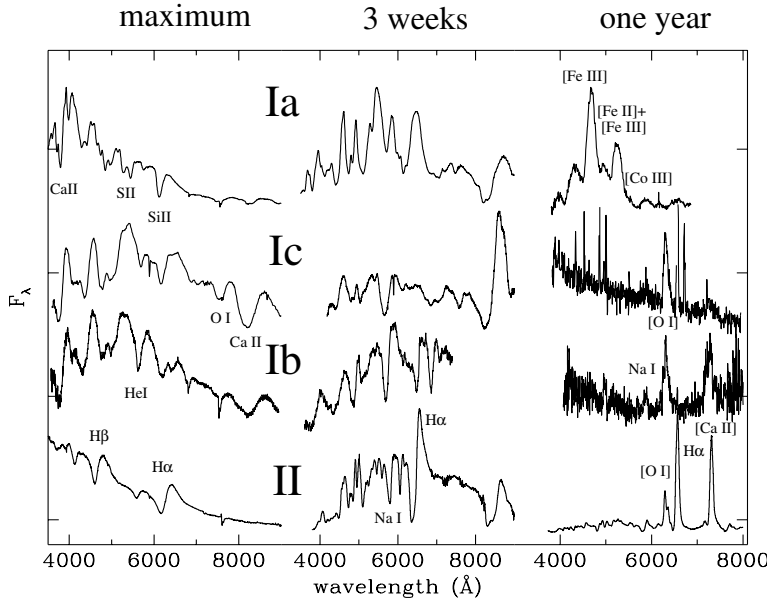
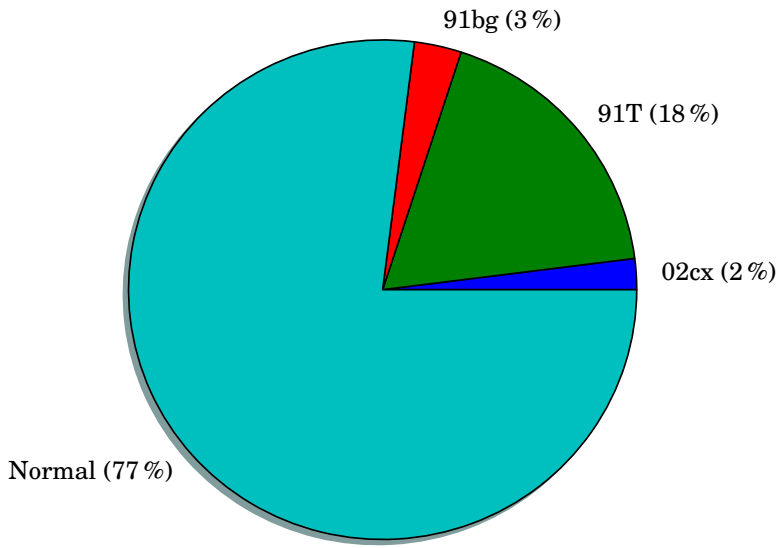


Figure 1.4 example caption

SNe Ia show a low intrinsic scatter in peak luminosity. Only in the past two decades have we been able to explore the finer details of the SNe Ia-class. Most objects have a small brightness scatter and are referred to as “Branch”-normal (Branch et al., 1993). There however seem to be two distinct subclasses with extreme luminosities. The overluminous class we call 91T s after the bright supernova SN 1991T Phillips et al. (1992); Schmidt et al. (1994) and the faint 91bg s named after the faint SN 1991bg (Filippenko et al., 1992). As a

further characteristic the community uses the velocity inferred from the Si II feature at 6130 Å. Faint supernovae are fast decliners both in velocity as well as luminosity Benetti et al. (2005). The bright supernovae do not seem to have such a preference. A third subclass named after SN 2002cx (Li et al., 2003) seems to contradict this theme. They decline slow and are faint. This subclass also shares spectral traits with the over luminous 91T s.

Li et al. (2011) have tried to measure the fraction of different subclasses from the Lick Observatory Supernova Search (LOSS). Figure 1.5 shows the fraction of the different subclasses that would be expected from a purely magnitude limited search.



**Figure 1.5** Estimated fractions for different SN Ia-classes for a purely magnitude limited search. Adapted from Li et al. (2011)

In summary, although there are several different subclasses, the **SN Ia** as a class itself is relatively homogenous when compared to the different Type II supernovae (henceforth SNe II).

SNe II span large ranges in observable parameters. We can divide the main class into four main subclasses. Type II Plateau Supernovae (henceforth Type IIP supernova (henceforth SN IIP); Barbon et al., 1979) have a relatively flat light curve after an initial maximum (see Figure 1.6). In contrast the Type II Linear Supernovae (henceforth Type IIL supernova (henceforth SN IIL); Schlegel, 1990) have a rapid linear decline after the maximum. The third subclass is the narrow-lined Type II Supernova (henceforth **SN III**) which is characterized by narrow emission lines, which are thought to come from interaction with the CSM. Finally the Type IIb supernovae (henceforth Type IIb supernova (henceforth SN IIb)) show strong hydrogen lines in their early spectrum, but evolve to become spectroscopically to be more like Type Ib supernovae with no hydrogen lines but strong Silicon and Helium lines. An interesting feature is the second maximum observed in the **SN IIb** SN 1993J (Figure 1.6). It is believed that many more **SN IIbs** exhibit this feature but are not detected early enough (this feature has also been seen in SN2008D a Type Ib supernova (henceforth SN Ib) Soderberg et al., 2008; Modjaz et al., 2009).

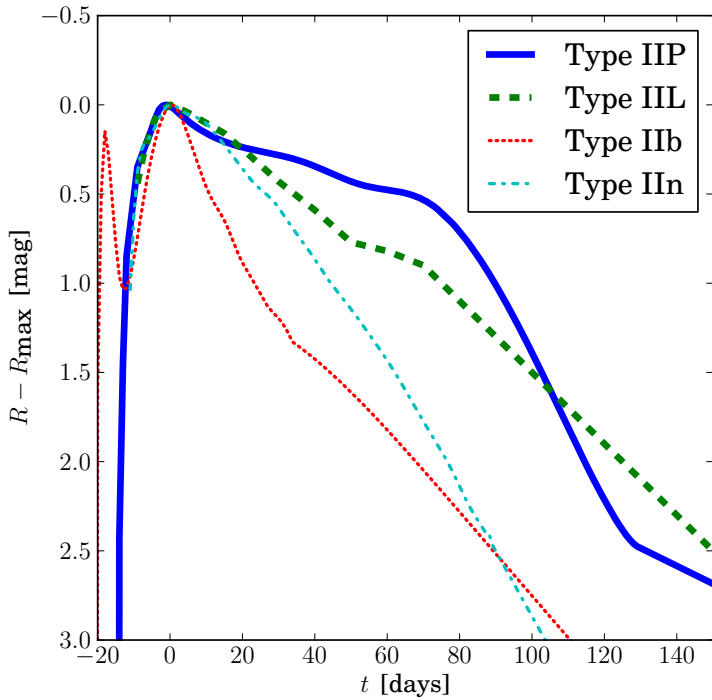


**Figure 1.6** Lightcurve data taken from [Li et al. \(2011\)](#) templates. The time is relative to maximum light and the magnitude is the difference between maximum

Figure 1.7 shows the estimated fractions of the different SNe II that would be expected from a purely magnitude limited survey.

Unlike the SNe Ia there are numerous intermediate objects among these three basic classes and some peculiar objects.

For a more comprehensive review of the classification of supernovae the reader should consult [Turatto \(2003\)](#) and [Turatto et al. \(2007\)](#).

### 1.3.2. Supernova rates

The observed supernova frequency carries important information about the underlying progenitor population. In this section we will concentrate more on SNe Ia-rates but will mention SNe II and Type Ib/c supernovae (henceforth SNe Ib/c) where applicable.

[Zwicky \(1938\)](#) was the first work that tried to measure the supernova rate. By monitoring a large number of fields monthly, they arrived at a supernova rate by merely dividing the number of supernova detection by the number of monitoring time and galaxies. This crude method resulted in a rate of one supernova per six centuries.

Over time many improvements were made to this first method. The rate was divided by galaxy morphological class as well as different supernova types. To normalise these quantities were then defined by the supernova rate as number of events per century per  $10^{10} L_\odot$  (e.g. [van den Bergh & Tammann, 1991](#); [Tammann et al., 1994](#)).

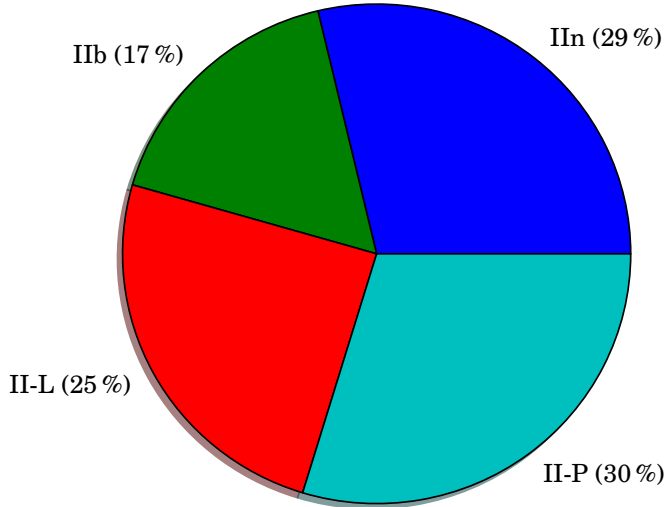


**Figure 1.7** Estimated fractions for different SN II-classes for a purely magnitude limited search. Adapted from Li et al. (2011)

In recent years, however, rate measurements have been in relation to star formation rather than galaxy luminosity (SN per century per  $10^{10} M_{\odot}$ ). The community (e.g. Mannucci et al., 2005) switched to the use of infrared photometry for the galaxy as it is thought to better represent star-formation rate than B-Band photometry (Hirashita et al., 2003) which had been used previously.

Figure 1.8 clearly shows that there is a strong connection between morphology and supernova rates. This suggests that SNe II and SNe Ib/c come from populations with recent star formation, which implies massive stars as progenitors. SNe Ia occur both in old elliptical galaxies and young spirals. It seems the progenitors occur in both of these environments. This could hint that there are two main progenitor types one which occurs soon after star-formation, whereas others take a long time between formation and explosion. The progenitors of SNe Ia are a highly debated topic (see Section ??).

To address this issue several groups have tried to measure a SNe Ia-rate that is completely independent of galaxy morphology (e.g. Mannucci et al., 2006; Maoz et al., 2010). This so called, delay time distribution (delay time distribution (henceforth DTD)), measures the supernova rate over time following a brief outburst of star formation. This technique requires a detailed knowledge of the star-formation history of these systems. Several new techniques are emerging that try to circumvent the intrinsically difficult task of determining star-formation for individual SNe Ia host galaxies (Maoz & Badenes, 2010; Barbary et al., 2010; Totani et al., 2008; Maoz et al., 2010).

Supernova rates and DTDs are a great tool to constrain progenitors. New upcoming surveys will provide an abundance of supernovae and measurements of their environments.

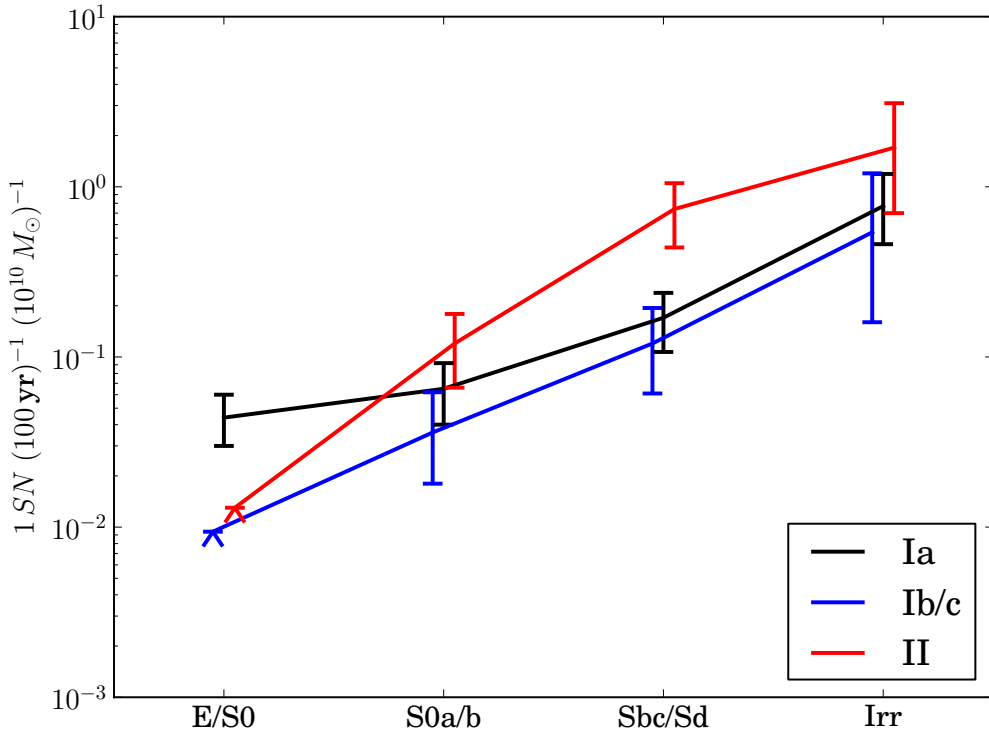


**Figure 1.8** The plot shows the estimated supernova rate per unit mass in different galaxy morphologies (Mannucci et al., 2005). ???Explain morphology ??? There have been no detections of SNe Ib/c and SNe II in old elliptical galaxies which suggests that these types only occur in galaxies with recent star-formation.

### 1.3.3. Light curves

Light curves give important insights into the physical reactions occurring during the evolution of the supernova. Arnett (1982) for example deduced from the light-curve shape that Type I supernova are eventually powered by the decaying  $^{56}\text{Co}$ .

For SNe Ia the light curve can be divided in four different phases (see Figure 1.9). In the first phase the SNe Ia rises to the maximum brightness. Although only a small fraction of SNe Ia have been observed in that phase, one can determine the time of the explosion by approximating the very early phase of a SNe Ia with an expanding blackbody. The luminosity of this blackbody is

$$L \propto v^2(t + t_r)^2 T,$$

where  $v$  is the photospheric velocity,  $T$  is the temperature of the fireball,  $t$  is the time relative to the maximum and  $t_r$  is the rise time. A rise time of 19.5 days (Riess et al., 1999) seems to fit most SNe Ia.

The rise is very steep and the brightness increases by a factor of  $\approx 1.5$  per day until 10 days before maximum.

The SN Ia reaches the maximum first in the NIR roughly 5 days before the maximum in the B-Band (Meikle, 2000). During the pre-maximum phase the color stays fairly constant

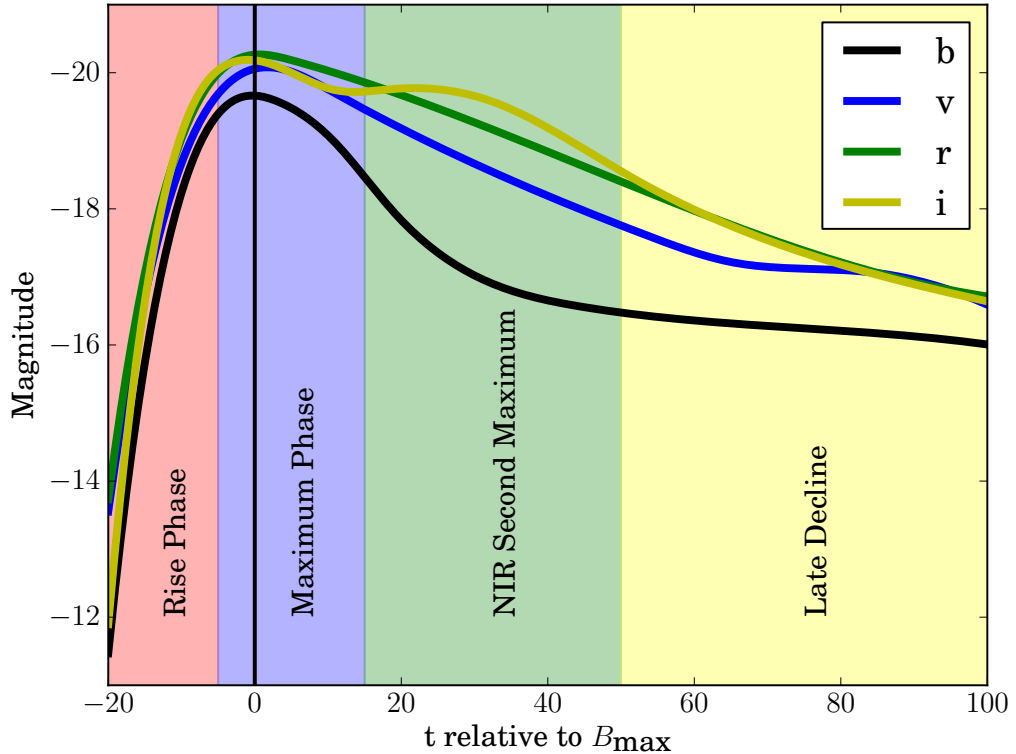


**Figure 1.9** Lightcurves of SN 2002bo (data from Benetti et al., 2004)

at  $B-V=0.1$ , but changes non-monotonically to  $B-V=1.1$  30 days after maximum.

The [SN Ia](#) starts to fade but a second maximum is observed in the NIR ([Wood-Vasey et al., 2008](#)). [Kasen \(2006\)](#) has successfully explained this by fluorescence of iron-peak elements in the NIR.

At roughly 600 days after maximum the light curve begins ??? 1991t had a foreground dust??? (how late do light curves go; a comment would be nice here brian ;-) )

Arguably the most important use of light curves is their application in normalizing [SNe Ia](#) to standard candles (see Figure 1.13). [Phillips \(1993\)](#) plotted the magnitude at maximum in different filters against the decline of the B-Band magnitude after 15 days ( $\Delta m_{15}(B)$ ). They found a strong linear relation with a very high correlation coefficient ( $> 0.9$ ). Dust extinction in the host is one of the major systematic problems and remains so to this day.

[Riess et al. \(1995\)](#) refined the method by using a linear estimation algorithm. This method would deliver a distance modulus by finding the offset between a template and the supernova lightcurve. They calibrated this method against a set of [SNe Ia](#) with known distances. Light curve fitting tools are still in active development (e.g. [Jha et al., 2007](#); [Guy et al., 2007](#)).

For description of lightcurves of [SNe II](#) please refer back to section 1.3.1.

#### 1.3.4. Spectra

Spectra are much more detailed measurements of Supernovae than just lightcurves. They are however, observationally much more expensive.

For all classes supernova spectra can be divided in two phases: the photospheric phase and the nebular phase. In the photospheric phase, the spectrum can be very well approximated by a dense optically thick core which has a black-body radiating surface with an optically thin expanding ejecta above. Photon creation is often negligible in the ejecta. The ejecta rather reprocesses the radiation field coming from the central photosphere. In the case of SNe Ia the core consists mainly of decaying  $^{56}\text{Ni}$  which produces the energy for the radiating photosphere. For SNe II the core mainly consists of ionized hydrogen.

As the supernova expands the photosphere recedes further into the core and the optically thin layer grows larger and larger. Once sufficiently expanded the entire SN ejecta becomes optically thin, which is known as the nebular phase. This phase is dominated by strong emission peaks and no continuum.

##### SNe Ia spectra

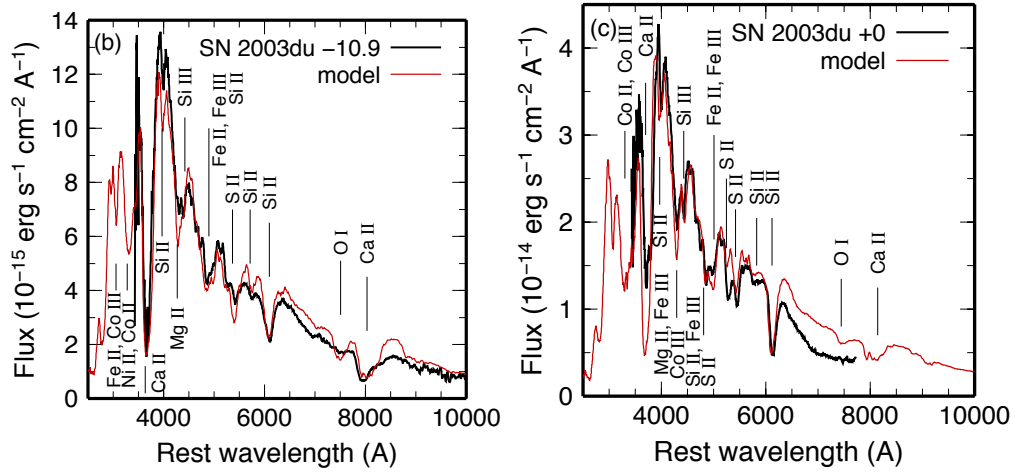
SNe Ia spectra help us understand the physical processes in the thermonuclear explosion. Shortly after the explosion the ejecta is in homologous expansion. Homologous expansion means  $v(r) = \frac{r}{t}$ . The observed spectra are characterized by an underlying continuum – emitted from the photosphere – and absorption features from the ejecta material above the photosphere. As time passes the photosphere recedes into the remnant and deeper layers of the exploded white dwarf become spectroscopically visible. Synthetic modelling of spectra is an important component to understanding SNe Ia and will be discussed in detail in Chapter 5.

This time-variability in the spectra is used to conduct tomography on SNe Ia (Stehle et al., 2005; Hachinger et al., 2009).

Similar to light-curves the spectra have different phases. We will use the “normal”-SN Ia SN 2003du to demonstrate the spectral evolution (Tanaka et al., 2011).

**Pre-Maximum Phase** In the pre-maximum phase the spectrum shows very high velocities (up to  $18\,000\,\text{km s}^{-1}$ ). There is a relatively well defined pseudo-continuum with strong P Cygni-profiles of IMEs and IGEs (see Figure ??). These IGEs are primordial as the burning in the outer layers (visible at these early times) is incomplete and does not produce these elements.

The CaII line is very prominent in the blue and often shows extremely high velocities at early times (in SN 2003du  $v \approx 25000\,\text{km s}^{-1}$ ). There have been multiple suggestion for the cause of this unusual velocity, including interaction with Calcium in the ISM or high-velocity ejecta blobs (Hatano et al., 1999; Gerardy et al., 2004; Thomas et al., 2004; Mazzali et al., 2005; Quimby et al., 2006; Tanaka et al., 2006; Garavini et al., 2007). There is a strong MgII feature at  $4200\text{\AA}$  which is contaminated by several iron lines. Silicon and Sulphur both have strong features  $5640\text{\AA}(\text{SII})$  and at  $6355\text{\AA}(\text{SiII})$ . The strong Silicon feature is the trademark for SNe Ia.



(a) SN 2003du 10 days before maximum light. The P Cygni-profiles of Silicon are clearly visible  
 (b) SN2003du spectrum at maximum light. The light in the UV is being suppressed and fluoresced into  
 (c) SN 2003du 10 days after maximum light. The red part of the spectrum.

**Figure 1.10** Premaximum evolution of SN 2003du spectra from [Tanaka et al. \(2011\)](#).

It is believed that in these early phases one should be able to see Carbon and Oxygen from the unburned outer layers. There is the CII-feature at 6578 Å but it is normally very weak (if visible at all). The Oxygen triple feature at 7774 Å is also seldom very strong.

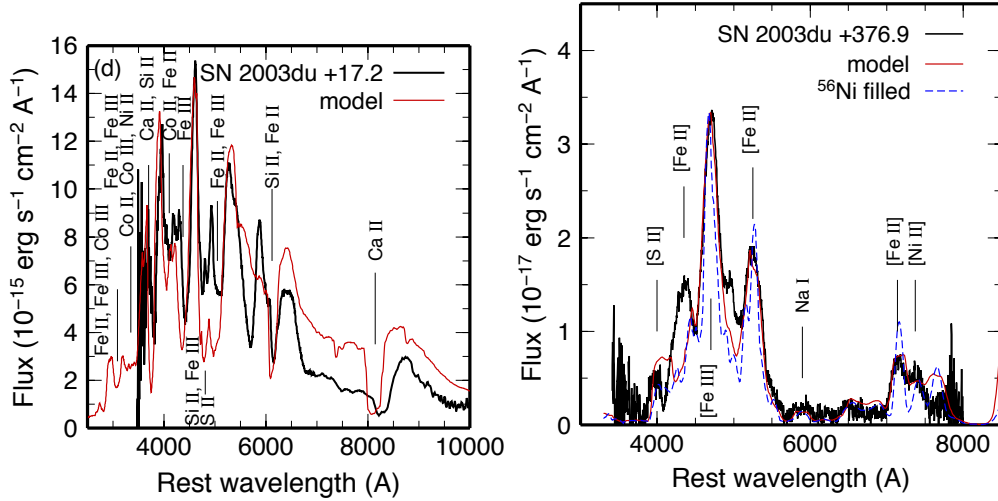
**Maximum Phase** As the supernova rises to the peak luminosity a large fraction of IGEs (especially  $^{56}\text{Ni}$ ) is suppressing flux in the UV and reemitting it in the visible (see Figure 1.10). The silicon lines become narrower as the photosphere reaches material deeper in the remnant. The ratio of the Silicon lines SiII 5972 Å and SiII 6355 Å is a good indicator for temperature ([Nugent et al., 1995](#)).

**Post-Maximum phase** The contribution from iron-group elements is still rising, while the photospheric velocity has decreased to less than 10000 km s<sup>-1</sup> (see Figure 1.11). The strong Calcium feature at 4000 Å is starting to disappear.

**Nebular-Phase** As the supernova fades, the photosphere disappears. At this stage the spectrum is now characterized by strong emission lines which are produced by the elements from the very core of the explosion (see Figure 1.12). The velocity has fallen under 5000 km s<sup>-1</sup>.

## SNe II Spectra

SNe II show much more variation in their spectra for each object than SNe Ia. In this section we will only give a very general and brief overview over SNe II spectra and spectral evolution. Compared to SNe Ia the initial spectrum is a relatively undisturbed continuum (see 1.4). The only strong lines visible are those of Hydrogen and Helium which are the



(a) SN 2003du 17 days past maximum light. The contribution of IGE is still rising.  
(b) In the nebular phase strong emission lines are visible. This phase is not observed very often but contains crucial information about the explosion physics.

**Figure 1.11** Postmaximum evolution of SN 2003du from [Tanaka et al. \(2011\)](#).

**Figure 1.12** example caption

elements present in the envelopes of the progenitors. As the photosphere recedes into the core heavier elements like Oxygen, Magnesium and Iron become visible.

The nebular spectra are characterized by  $H\alpha$ , Oxygen and Calcium emission lines.

Most knowledge we have about all classes of supernovae we have obtained through optical spectroscopy and photometry. Panchromatic studies of supernovae are for the moment rare.

### 1.3.5. X-Ray & Radio observations

Compared to the traditional optical astronomy X-Ray & Radio are relatively new fields. The information carried in the very high and low frequency photons is invaluable to understanding various transient events.

The long GRB-phenomenon has been suggested to be the relativistic jet launched in a SN Ib/c. It is believed that GRBs are visible when this jet points towards the observer (also known as on-axis). In their late phase the GRB's jet spreads and is thought to emit isotropically in radio frequency. This radio glow should be visible to both on-axis and off-axis observers, but has so far only been observed on-axis. [Soderberg et al. \(2006\)](#) have tried to find this isotropic radio emission at late times on SN Ib/c to see if they are off-axis GRBs. The study however remained inconclusive.

SNe II have long been theorized to emit X-rays at shock breakout ([Klein & Chevalier, 1978](#); [Colgate, 1974](#)). To observe shock breakouts is technically very challenging as the supernova needs to be detected very early. SN2008D was serendipitously discovered by observation with the Swift X-ray telescope. It was in the process of observing another supernova SN

2007uy in the same galaxy when picked up an extremely luminous source Soderberg et al. (2008). Subsequent ground based follow-up revealed a brightening optical counterpart which turned out to be a SN Ib/c. The X-ray-flash was the theorized shock breakout of a SN II.

Voss & Nelemans (2008) have suggested that they found the progenitor of the Type Ia SN 2007on in X-rays. The main caveat speaking against their find was the sizeable distance between the supernova and the X-ray-source. Their technique however is promising. Following up SNe Ia in X-ray-archives could detect potential SNe Ia progenitors in a pre-explosion X-ray phase.

Radio and X-ray observation of both kinds of supernovae are still in its infancy and will provide great help when solving the current mysteries surrounding all types of supernovae.

### 1.3.6. Supernova Cosmology

Early in the last century astronomers where trying to gauge our place in the universe. Hubble (1929) discovered that the Milky Way was not the only galaxy of the universe but found that there were several such galaxies much farther than previously suspected. He used, among other methods, the known intrinsic luminosity ( $L_0$ ) of Cepheid variables and determined the distance using the observed luminosity ( $L/L_0 \propto 1/r^2$ ). In addition he found that galaxies that were further away had a higher velocity from the Milky Way than close galaxies. He suggested that the universe was in a state of constant expansion. Cepheids distance measurements are only possible for very close-by galaxies and astronomers were feverishly searching for brighter more precise distance probes (also known as standard candles). The discovery that supernovae are distant objects (Baade & Zwicky, 1934) motivated many astronomers to use them as standard candles Baade (1938); van den Bergh (1960); Kowal (1968); Perlmutter et al. (1999).

This culminated nearly 70 years later in another paradigm changing discovery. The accelerating expansion universe was discovered, using the same principal but much more advanced technology, by two teams (Riess et al., 1998). Since then other techniques have come to the same conclusion (e.g. Blake et al., 2011). Both SNe Ia and SN II have been used as cosmological distance probes:

**SN II Cosmology** SN IIP have been first suggested as cosmological probes by Kirshner & Kwan (1974). It is important for cosmological distance probes to know the intrinsic luminosity precisely. In the plateau-phase of the supernova, caused by the recombination of ionized hydrogen, the temperature is well known ( $T=5000$  K). In addition it is assumed that the supernova is in free expansion, thus a measurement of the velocity and an assumption of the initial radius results in a known radius. Assuming the supernova to be a blackbody during plateau-phase one can then calculate a luminosity using the radius and the temperature. SN IIP as distance candles, however, are observationally expensive and not as accurate as SN Ia as standard candles (15% error for SN II vs 7% error for SN Ia (Nugent et al., 2006)).

**SN Ia Cosmology** SNe Ia have been one of the most successful distance probes. It is believed that SNe Ia are the explosion of C-O white dwarfs. The brightness of these objects

is powered by the decay of  $^{56}\text{Ni}$ . The quantity of  $^{56}\text{Ni}$  produced in the explosion can be gauged from the evolution of the light-curve which then in turn can be used to calibrate the intrinsic brightness (see Figure 1.13). In the late 1990s new detector technologies (CCDs), computing and new telescopes made it possible to measure the light curves of many SNe Ia accurately.

The amazing discovery that both [Riess et al. \(1998\)](#) and [Perlmutter et al. \(1999\)](#) made with SNe Ia was that the universe, in stark contrast to the earlier assumption, was expanding at an accelerating rate.

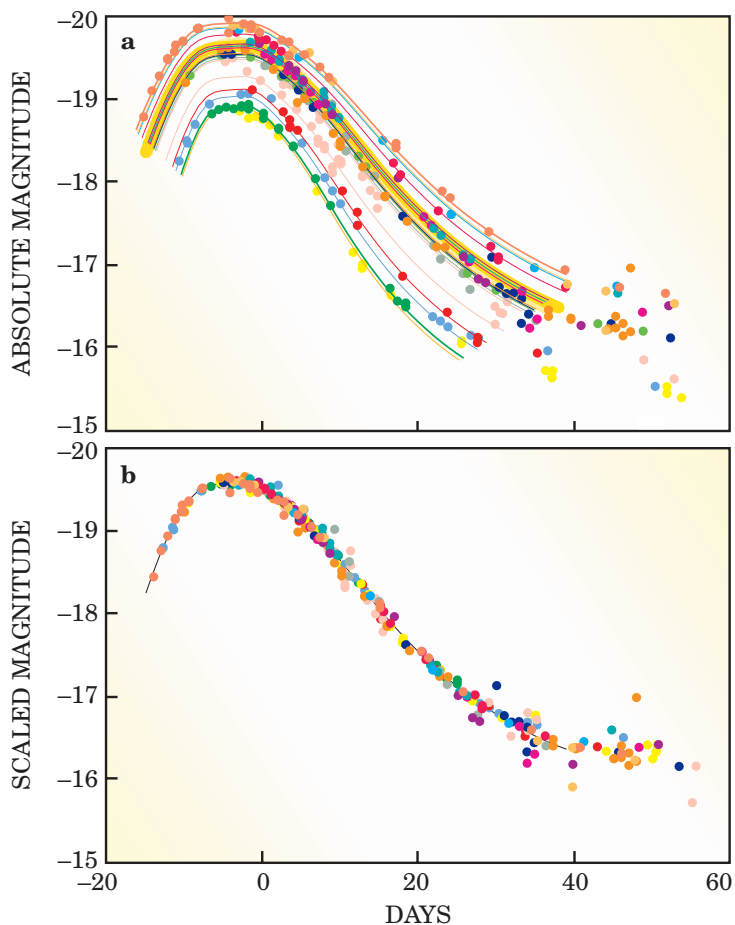


**Figure 1.13** Replace with some data. any suggestions

## 1.4. Post-explosion observations of Supernovae

In most cases for SNe Ia, SNe Ib/c and SNe II the distance to the supernova is too large to make detailed studies of these events post-explosion.

When supernovae, however, happen in nearby galaxies or in our own we have the chance of detailed post-explosion follow-up. SN 1987A, which exploded in the close LMC, provided an ideal candidate for follow-up post-explosion which revealed that a previously observed Blue Supergiant was not visible post-explosion [Walborn et al. \(1989\)](#). This suggests that

this star was the progenitor of SN 1987A. It was the first time a progenitor was identified with this “direct detection”-method and since then many more progenitors have been unearthed post-mortem (for a review see Smartt (2009)).

Modern X-Ray space telescopes provide data of exquisit detail to study the remnants of supernovae. Hydrodynamic and nonequilibrium ionization simulations of shocks from the supernova ejecta with the ISM can be used to measure temperature, elemental abundances and other parameters related to the state of the ejecta (Badenes et al., 2003; Sorokina et al., 2004; Badenes et al., 2005). This technique of modelling has been used to scrutinize ancient remnants. Kepler and Tycho remnants have been unambiguously identified using X-ray-spectroscopy to be remnants of SNe Ia (Badenes et al., 2006; Reynolds et al., 2007). This field is still at its infancy and future coupling of three dimensional models with X-ray-observations will help reveal the explosions mechanisms for both physical types of supernovae: thermonuclear explosions and core-collapse of massive stars.

Light-echoes are features that appear when light from a supernova scatters on dust in the ISM. This has been suggested by Zwicky (1940), but only advancements in imaging techniques as well as digital processing made it possible to detect these echoes. Rest et al. (2005) pioneered this technique and found several of these echoes in the LMC. Follow-up observations by Rest et al. (2008) showed that it is possible to obtain a spectrum and identify the type of supernova with it. Krause et al. (2008) subsequently observed the light-echo of Tycho’s supernova (SN 1572) and identified it as a “normal” SN Ia and confirmed the previous X-ray-spectroscopy result. Future wide-field surveys will hopefully reveal many more of these light-echoes. Light-echoes can not only be used for classification but also for a three dimensional spectroscopic view of supernovae (demonstrated on the example of Cassiopeia A remnant Rest et al., 2011).

Post-mortem observations of supernovae and their light-echoes provide us with unique insights into these events. For nearby galaxies like the LMC it is possible to scrutinize supernovae using their remnants and echoes which exploded over the last 20,000 years. This in turn can be used to infer rates and DTDs (Maoz & Badenes, 2010).

## 1.5. Core-Collapse Supernova Theory

All **SN II** and **SN Ib/c** are believed to be powered by the collapse of the electron-degenerate iron core of massive stars. For the iron core to form there had to be several prior stages of evolution.

### 1.5.1. Evolution of Massive Stars

To understand the state of the star shortly before supernova evolution it is imperative to follow its evolution. For the topic of core-collapse we will concentrate on the nuclear physics of a single massive star evolution. There has been ample suggestions that some **SN II** and **SN Ib/c** progenitors are binary ([Podsiadlowski et al., 1992](#)), but their evolution is much more complex and is outside the scope of this work. In this context massive stars are stars bigger than  $8 M_{\odot}$ . This is the minimum mass for a star that is believed to explode in a **SN II**. Like all stars massive stars spend most of their lives on the main-sequence burning hydrogen. This happens via the carbon-nitrogen-oxygen cycle and its various side-channels (e.g  $^{12}C(p, \gamma) \rightarrow ^{13}N(e^+\nu) \rightarrow ^{13}C(p, \gamma) \rightarrow ^{14}N(p, \gamma) \rightarrow ^{15}O(e^+\nu) \rightarrow ^{15}N(p, \alpha) \rightarrow ^{12}C$ ). For a  $20 M_{\odot}$  star this phase lasts for 8.13 Myr (see [Woosley et al. \(2002\)](#)).

As the star evolves it begins to ignite Helium which burns via the triple- $\alpha$  process to Carbon ( $3\alpha \rightarrow ^{12}C$ ) and then to Oxygen ( $^{12}C(\alpha, \gamma) \rightarrow ^{16}O$ ). Table 1 in [Woosley et al. \(2002\)](#) lists 1.17 Myr for this phase.

Due to neutrino losses the stellar evolution is qualitatively different after helium burning. A neutrino-mediated Kelvin-Helmholtz contraction of the carbon-oxygen core describes the advanced stages of nuclear burning in massive stars ([Woosley et al. \(2002\)](#)). This contraction is occasionally delayed when the burning of new fuel sources counter-acts the neutrino losses. The star in the end is composed of a series of shells that burn the above fuel and deposit the ashes on the shell below (see Figure 1.14). There are four distinct burning stages. Their principal fuels are carbon, neon, oxygen, magnesium and silicon.

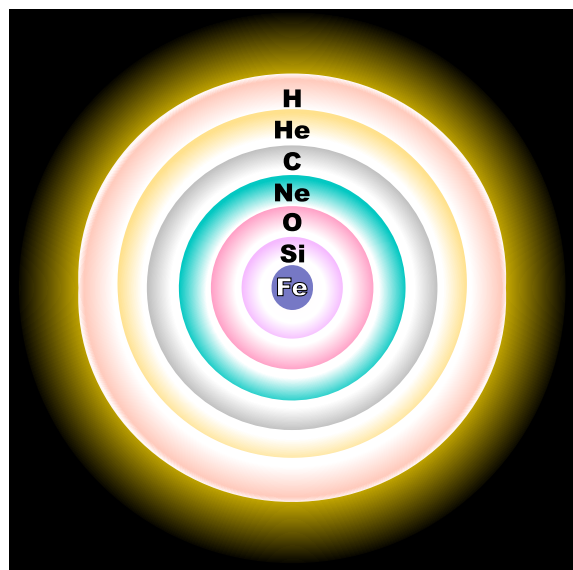
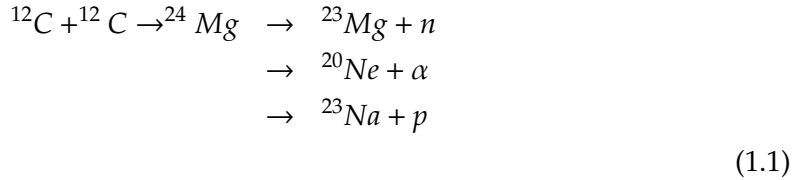


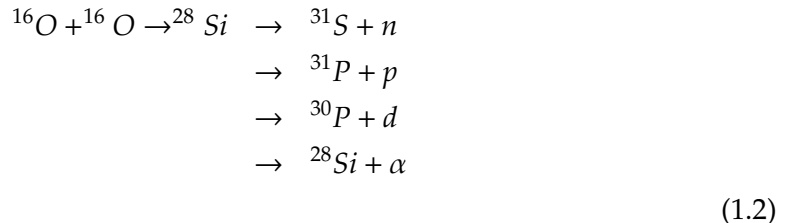
**Figure 1.14** Shell Burning of a massive star before SN II. (Source Wikipedia, Creative Commons License)

In the carbon burning stage two  $^{12}\text{C}$  nuclei are fused to an excited state of Magnesium which then decays slowly to  $^{23}\text{Na}$  (see Equation 1.2).



Although oxygen has a lower Coulomb barrier, the next nucleus to burn after Carbon is Neon. This layer is composed of  $^{16}\text{O}$ ,  $^{20}\text{Ne}$  and  $^{24}\text{Mg}$  and burns Neon with high-energy photons from the tail of the Planck distribution ( $^{20}\text{Ne}(\gamma, \alpha)^{16}\text{O}$ ).

In the next shell there is a composition of mainly  $^{16}\text{O}$ ,  $^{24}\text{Mg}$  and  $^{28}\text{Si}$ . The bulk nucleosynthetic reaction is shown in Equation 1.2.



The last shell is burning  $^{28}\text{Si}$  to  $^{56}\text{Ni}$ . The obvious reaction  $^{28}\text{Si} + ^{28}\text{Si} \rightarrow ^{56}\text{Ni}$  does not take place, but is replaced by a very complex network of isotopes to burn to  $^{56}\text{Ni}$ . In simulations this is computationally intensive and numerically unstable (e.g. [Weaver et al. \(1978\)](#) who carry a 128-isotope network). Following silicon burning the composition consists of mainly iron-group nuclei. At the end of silicon burning we are reaching nuclear statistical equilibrium.

### 1.5.2. Core collapse

Before the collapse, the core consists of iron peak elements. Neutrino losses during carbon and oxygen burning decreased the central entropy sufficiently so that the core becomes electron degenerate. Such a degenerate core, which is higher than the Chandrasekhar mass (adjusted for  $Y_e$ , entropy, boundary pressure and other parameters) will collapse.

There are two main instabilities that facilitate the collapse. As the density rises the Fermi-Energy becomes high enough for electrons to capture onto iron-group nuclei. This capture process removes electrons that were providing degeneracy pressure and reduces the structural adiabatic index.

The second instability is the rise to temperatures where the nuclear statistical equilibrium favours free  $\alpha$ -particles. The collapse eventually leads to nuclear densities, the hard-core potential acts as a stiff spring during the compressive phase. It stores up energy and eventually releases this energy resulting in a "core bounce". [Baron et al. \(1985, 1987\)](#) believed the core bounce to provide the energy for the ensuing supernova explosion. More recent simulations, however show that the bounce shock is not sufficient for a **SN II**

explosion. The bounce shock loses energy by photo disintegrating the nuclei it encounters (losing roughly  $10^{51}$  erg per  $0.1 M_{\odot}$ ).

The energy for a successful explosion is now thought to come from neutrino energy deposition. This reinvigorates the shock and leads eventually to an explosion which ejects the envelope of the massive star. [Burrows et al. \(2007\)](#) suggest that instead of neutrinos, acoustic waves might heat up the ejecta and cause the explosion. In any case a newly born neutron star is left behind.

The precise explosion mechanism is unknown. Using progenitor models with different parameters like rotation and mass lead to different outcomes. [Woosley et al. \(2002\)](#) provide a very comprehensive review of the theory of evolution and core collapse. In particular they go into more detail describing the scenarios after core-bounce.

### 1.5.3. Pair instability

One alternate explosion scenario is the pair-instability supernova. This scenario is believed to only happen in stars with a helium core of more than  $40 M_{\odot}$ . After core helium burning the star starts to contract at an accelerated rate. The energy release during this process is used to produce electron-positron pairs rather than raising the temperature. If significant densities are reached, oxygen fusion eventually halts the implosion and the collapse bounces to an explosion. For very high stellar masses it is believed that oxygen fusion does not provide enough energy to halt the contraction and the star collapses to a black hole.

### 1.5.4. Type II Supernovae

The observables of these stellar cataclysm are the light curve, spectra and for one case even the neutrino wind. The supernovae goes through three distinct phases which can be observed.

The shock-breakout is the first visible signal from the supernova. [Enzman & Burrows \(1992\)](#) calculated a duration for the shock breakout of SN1987A to 180 s three minutes, its luminosity of  $5 \times 10^{44} \text{ erg s}^{-1}$ . Thus far it has been observed only once in 2008D ([Soderberg et al., 2008](#)). They report a duration of 400 s with a luminosity of  $6.1 \times 10^{43} \text{ erg s}^{-1}$ .

The plateau seen in many [SN II](#) (see Figure 1.6) is produced by the recombination of hydrogen when hydrogen-rich zones cool to less than 5500 K. The radiation comes effectively from a blackbody, whose luminosity is determined by the radius of the photosphere. Supernovae of Type IIL do not show this behaviour and are thus thought to have no or a very small hydrogen envelope.

After the recombination of hydrogen the light-curve drops off linearly and we see radioactivity providing the main energy source.  $^{56}\text{Ni}$  decays to  $^{56}\text{Co}$  with a half-life of 6.1 d and then further to  $^{56}\text{Fe}$  with a half-life of 77 d. Most of the energy of the  $^{56}\text{Ni}$  decay is used to accelerate the expansion of the core. The tail of the light-curve after the plateau is mainly powered by the decay of  $^{56}\text{Co}$ . Some light might also be produced by shock interaction with the [CSM](#).

### 1.5.5. Type Ib/c supernovae

If the star lost all of its hydrogen envelope prior to core-collapse there is no plateau visible in the light-curve. Instead the light-curve is powered by radio-active decay after shock breakout. In addition, the hydrogen lines are not visible in the spectrum. This leads to the supernova being classified as Type Ib. If both hydrogen and helium envelopes are lost then the supernova is classified as Type Ic. This loss of envelope is presumed to be caused by stellar winds or binary interactions (Podsiadlowski et al., 1992).

## 1.6. Thermonuclear Supernova Theory

In this section we will discuss the theory of **SNe Ia** which are thought to be thermonuclear explosions of degenerate Carbon/Oxygen matter. The different progenitor scenarios leading to an explosion of a massive white dwarfs are discussed in Section 1.7.

### 1.6.1. White Dwarfs

Carbon/Oxygen white dwarfs are thought to be the progenitor stars of **SNe Ia**. White dwarfs are among the few stellar objects that do not hold hydrogen. This would explain the lack of hydrogen in **SN Ia**-spectra. It is general believed in the community that these objects accrete matter (for the possible scenarios see section 1.7) until they get close to the Chandrasekhar-mass  $M_{\text{Chan}}$ . It is a delicate balance between the ignition point that results in the thermonuclear run-away and the Chandrasekhar threshold which leads to a collapse of the star to a neutron star.

There are three main classes of white dwarfs: Helium White Dwarfs, CO-WDs and ONe-WDs. Helium white dwarfs would start burning their Helium to Carbon and Oxygen well before it gets near the Chandrasekhar mass. ???? In addition, these objects can also be ruled out as progenitors for **SNe Ia** as they produce copious amounts of **IGE** which are not consistent with the burning of a Helium white dwarf.????

The ultimate fate of an **ONe-WD** is thought to be the collapse into a neutron star. Once the **ONe-WD** is heavy enough electron capture begins in the core ( $^{20}\text{Ne}(e^-, \nu)^{20}\text{F}(e^-, \nu)^{20}\text{O}$ ). Heating by the resulting  $\gamma$ -rays starts explosive Oxygen burning. However, the electron-capture is much faster than the Oxygen burning and promotes the collapse to a neutron star (Nomoto & Kondo, 1991; Gutiérrez et al., 2005).

The favoured progenitor for a **SN Ia** are **CO-WDs**. Most of these objects are born, however, with a mass around  $0.6 M_\odot$  (Kepler et al., 2007). It is thought that they accrete mass until they are getting close to the Chandrasekhar mass and then explode as a **SN Ia**.

### 1.6.2. Pre-supernova evolution

The white dwarf gradually accretes more and more material. Close to  $M_{\text{Chan}}$  mild carbon burning ensues



, but is mediated by photon and neutrino losses (Lesaffre et al., 2005; Iliadis, 2007). As these cooling processes become less effective convection starts in the core. The energy output in the core increases. At this stage the thermal structure is largely controlled by Urca pairs. These reaction pairs consist of alternating electron captures and  $\beta^-$ -decays involving the same pair of parent and daughter nuclei. Two prominent examples which are important in pre-supernova evolution are  ${}^{21}\text{Ne}/{}^{21}\text{F}$ :



These processes can lead to either cooling or heating. Lesaffre et al. (2005) have modelled this process in a convective core.

Ultimately, the pre-supernova evolution is hard to model theoretically as it is likely to be nonlocal, time-dependent, three dimensional and stretches over hundreds of years. The exact conditions at the time of explosion are therefore unknown. All explosion models have to assume simple initial conditions. The main steps leading to the explosion are as follows:

**Ignition:** The Urca processes will dominate core evolution for the last thousand years until explosion. As the temperature rises to  $T \approx 7 \times 10^8 \text{ K}$  (Hillebrandt & Niemeyer, 2000) the convection time ( $\tau_c$ ) increases and becomes comparable to the burning time ( $\tau_b$ ). Consequently the convective plumes burn as they circulate. Once the temperature reaches  $T \approx 10^9 \text{ K}$   $\tau_b$  becomes very small compared to  $\tau_c$  and Carbon and Oxygen essentially burn in place. This is the moment of ignition. As the convective plumes burn while they rise it is likely that the initial flame seed does not start in the center of the core. Röpke & Hillebrandt (2005) have used multiple flame seeds in their three dimensional full star models.

**Thermonuclear Explosion:** From this point, initially there were two main options. The first option was the complete detonation (supersonic flame front) of the CO-WD (Arnett, 1969). It was quickly discovered, however that this method burns to NSE and thus produces no IME. These IME are observed in SN Ia.

For a long time it was then suspected that the star instead of detonating would deflagrate (subsonic flame wave, mediated by thermal conduction). The fuel in front of the deflagration gets rarefied by the energy from the flame. Hot light burning bubbles rise into the cold dense fuel and create Rayleigh-Taylor instabilities (see Figure 1.15 at  $t=0.72 \text{ s}$ ). Once the deflagration wave has run through the star, the resulting production of  ${}^{56}\text{Ni}$  is not enough

to explain the light curve of normal **SN Ia**. The deflagration produces roughly  $0.3 M_{\odot}$  of  $^{56}\text{Ni}$ , to power the light curve of normal **SNe Ia** one needs  $0.6 M_{\odot}$  (Mazzali et al., 2007).

The currently favoured scenario is the one of delayed detonation. The star initially burns like in the deflagration scenario, then inhomogeneities in the deflagration front produce hotspots. In these hotspots the temperature gradients are so high that detonation waves form. The ensuing detonation front can only burn the cold unburnt-fuel and does not penetrate the ashes of the deflagration. Figure 1.15 shows clearly how the detonation wave wraps around the cold ashes over the course of the detonation.

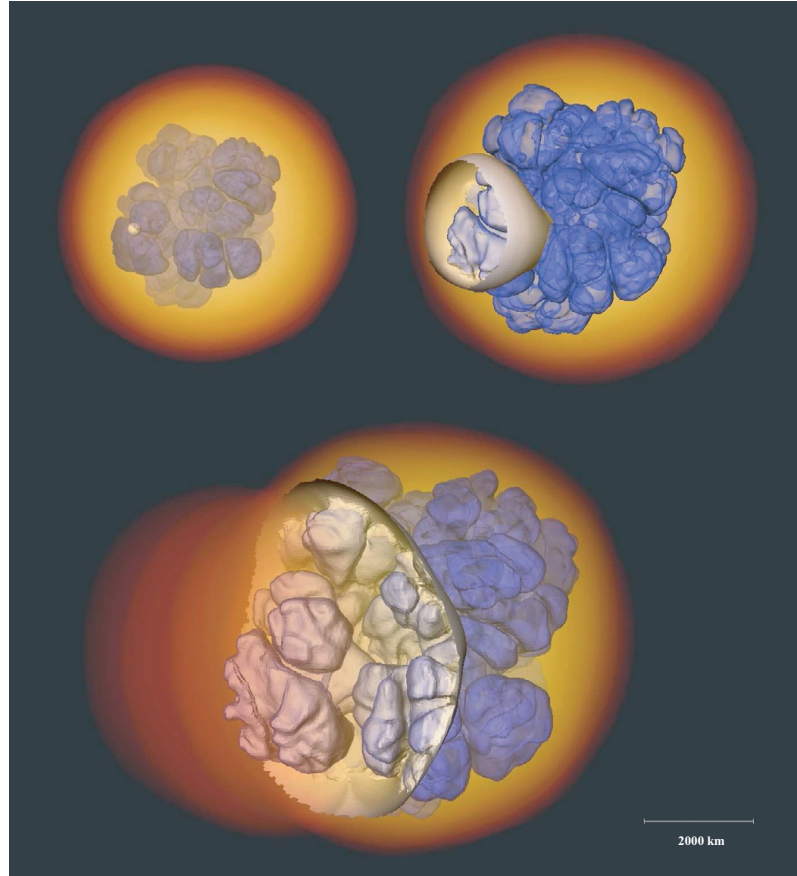


**Figure 1.15** Delayed detonation simulation from Röpke & Bruckschen (2008). The upper panels show the deflagrated interior (marked in blue) and the detonation ignition point (small white sphere). The detonation wave wraps around the deflagration ash and consumes the cold fuel. (Image reproduced with kind permission of Fritz Röpke)

An open question is if and how these transitions from deflagration to detonation occur in **SNe Ia**. This scenario reproduces the light curves and spectra reasonably well (Kasen et al., 2009).

**sub-Chandrasekhar-mass detonations** Shigeyama et al. (1992) and Sim et al. (2010) have explored the detonation of CO-WDs at sub-Chandrasekhar masses. Sim et al. (2010) show that the detonation of a sub-Chandrasekhar-mass CO-WD reproduce observed light-curves and early-time spectra of **SNe Ia** fairly well.

The main issue in this scenario is the ignition. Fink et al. (2010) have suggested an explosion

mechanism in which a surface detonation of a Helium shell drives a shock-wave into the core. In the core this shockwave triggers an ignition by compression. As an initial model they use a CO-WD accreting from a helium rich companion building a thin helium shell around its CO interior (described in [Bildsten et al., 2007](#)). This helium shell is ignited and sends out a shockwave. As the helium flame spreads on the shell around the star it sends a shockwave into the core. Once the shockwaves converge off-center they create a the right environment for the ignition of a detonation wave (see Figure 1.16.)

This scenario reproduces the intrinsic luminosity variability in the class of [SN Ia](#) as each exploding white dwarf can have a different mass.

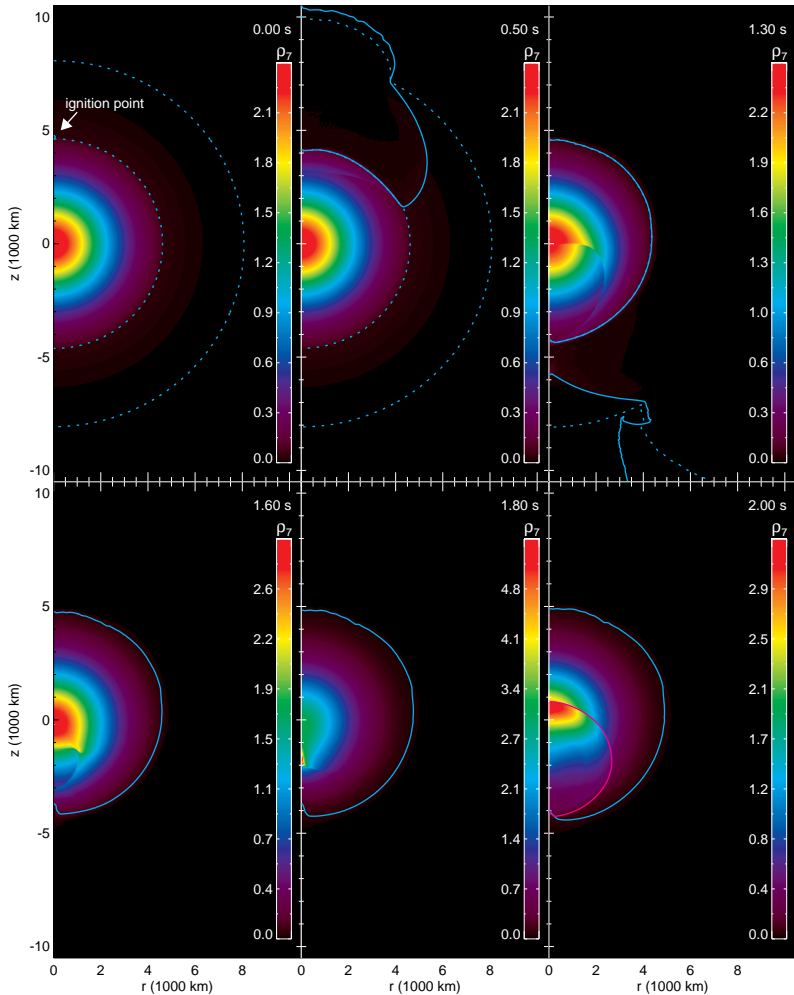


**Figure 1.16** The ignition point of the helium shell is marked in the upper left image. We can follow the helium shell sending shock waves into the core of the white dwarf. They converge in the lower left image at the opposite site of the Carbon/Oxygen core (data from [Fink et al., 2010](#), figure kindly provided by Michael Fink).

**White dwarf mergers ????** CO-WD mergers for a long time were thought to lead to a gravitational collapse (same mechanism as the ONe-WD [Saio & Nomoto, 1985](#)). [Pakmor et al. \(2010\)](#) has, however, successfully simulated the explosion of two merging CO-WDs. The initial model was two equal mass  $0.8 M_{\odot}$  CO-WDs. The merging process created a

hotspot from which a detonation wave emanates. The resulting light-curves and spectra are faint and are similar to the class of sub-luminous **SN Ia**.

## 1.7. Progenitors of Type Ia Supernovae

**Whelan & Iben (1973)** first introduced the modern binary evolution paradigm for **SN Ia**-progenitors. In their model a **CO-WD** accretes matter from a red giant. A degenerate **CO-WD** accreting from a non-degenerate companion is now known as the single degenerate scenario.

**Webbink (1984); Iben & Tutukov (1984)** were the first to suggest that the merging of two **CO-WDs** could also produce **SNe Ia**. This scenario is now commonly referred to as the double degenerate scenario.

### 1.7.1. Single Degenerate Scenario

The single degenerate scenario assumes a binary system with one evolved white dwarf and one non-degenerate companion. In most cases this non-degenerate companion is thought to be main-sequence to red giant. There are scenarios that involve "exotic" companions such as helium stars. The companion (or donor) star is believed to have filled its Roche-Lobe and lose mass via Roche-Lobe-Overflow (henceforth RLOF).

#### Accretion

The main problem of the SD-scenario is the accretion process. As most white dwarfs are born with masses around  $0.6 M_{\odot}$  they need to accrete mass to reach the critical  $1.38 M_{\odot}$ . The process needs to be efficient as well as burn most accreted hydrogen to explain its lack in the spectrum. If the mass-accretion rate is too low it causes nova explosions which are thought to eject more mass than they had accreted prior (**Nomoto, 1982**). There are however systems (e.g. RS Oph, U Sco) that have white dwarf masses close to  $1.4 M_{\odot}$  which have recurrent nova outbursts. It is very likely that these systems weren't born with a white dwarf that massive, but that these white dwarfs accreted the material. This suggests that despite nova outbursts efficient accretion is possible.

Too high accretion rates would engulf the binary in an extended red giant envelope which would promote a merger of the two compact objects. Debris of such an envelope is not seen in **SN Ia**-explosions. To avoid this merger the system would have to lose the excess mass in a wind. This again results in a low accretion rate. There is only a very narrow range of accretion rates that allows the white dwarf to accrete hydrogen, stably burn it and efficiently accrete to **M<sub>Chan</sub>**. **Yoon & Langer (2004)** have suggested that rotation of the accreting white dwarfs might increase this very narrow parameter range.

A class of binaries called SSS might accrete hydrogen at a sufficiently high rate. At this rate hydrogen and helium burn hydrostatically, if retained, make these objects very strong contenders for **SN Ia** progenitors (**Di Stefano et al., 2006**, and references therein).

Another subclass of SD-progenitors are AM CVn stars (**Nelemans, 2005**). These type of cataclysmic variable accretes from a helium star **van den Heuvel et al. (1992)**. This scenario

would very conveniently explain the lack of hydrogen in **SN Ia**-explosions. [Fink et al. \(2010\)](#) have found a way that such systems can explode in a **SN Ia**(see Section ??).

## Donor Stars

???? radial velocity???? The SD-scenario requires a secondary companion (also known as donor) star. If this companion survives the explosion it would be a calling card for the SD-scenario.

[Marietta et al. \(2000\)](#) have simulated the impact of **SN Ia**-ejecta on main-sequence, sub-giant and red-giant companion. In the case of the main-sequence companion the supernova ejecta heats a small fraction (1-2%) of the envelope which is lost post-explosion. [Pakmor et al. \(2008\)](#) have repeated the simulations for the main-sequence companion and find similar results, but suggest that less mass is lost. Post-explosion the star could be very luminous ( $500 - 5000 L_{\odot}$ ). It is expected to cool down between 1400 – 11000 yrs and follow the main-sequence track.

For the sub-giant companion the simulations show very similar results to the main-sequence companion. In summary, the subgiant loses only a small fraction of the envelope (10 – 15%) and similar to the main-sequence star will be very luminous shortly after the explosion. After thermal equilibrium is established the companion will return to a post-main-sequence track.

The case of the red-giant, however, is very different. [Marietta et al. \(2000\)](#) suggest that it will loose most of its loosely bound envelope. Post-explosion the remaining core rises contracts and the temperature rises to more than  $3 \times 10^4$  K. The object may appear as an under luminous main-sequence O or B star.

[Justham et al. \(2009\)](#) have suggested low-mass single white dwarfs to be the remaining cores of red-giant donor stars. This would result in a convenient explanation for the existence of these objects.

One feature of surviving companions may be an unusually large rotational velocity post-explosion ([Kerzendorf et al., 2009](#), chapter ?? of this work). Due to tidal coupling during the **RLOF**-phase one calculate the expected rotational velocity from the escape velocity of the donor (see Figure 2.2). Late-type stars usually don't display such high rotational velocities. Thus this feature is a very useful discriminant when looking for donor stars.

Most simulations suggest that the donor-star would survive the explosion one way or another. There have been several attempts to find these objects in ancient supernova remnants. [Schweizer & Middleditch \(1980\)](#) found a OB subdwarf star located 2.5 'from the center of the remnant of SN1006 and suggested this as the donor star. Subsequent analysis by [Wu et al. \(1997, 1983\)](#) have however revealed however strong red and blue shifted iron lines. The velocities of these lines are on order of  $5000 \text{ km s}^{-1}$  which is the same as the velocity of the freely expanding remnant of SN 1006. This suggests the star to be located behind the remnant and not the donor.

The search of donor stars in ancient remnants is one of the main parts of this thesis and we direct the reader to chapter ?? and chapter 3.

### 1.7.2. Double Degenerate Scenario

Webbink (1984) and Iben & Tutukov (1984) were the first to suggest merging white dwarfs as progenitors for SN Ia. There are several advantages to the DD-scenario. For example, it naturally explains the lack of hydrogen in SN Ia-spectra. The accretion problem encountered in the SD-scenario are also elevated with DD-scenario, as long as the sum of masses of both CO-WD's is above  $M_{\text{Chan}}$ .

The problem, however, is that most SN Ia are relatively homogeneous. It is hard to reconcile this fact with the merger of two white dwarfs with different initial masses, composition, angular momenta and different impact parameters. Another caveat, however, is that the accretion of the disrupted lighter white dwarf onto the more massive white dwarf might lead to the transformation into a ONe-WD (see section 1.6.1)

Pakmor et al. (2010) have simulated the merger of two equal-mass white dwarfs ( $0.8 M_{\odot}$ ) and conclude that the outcomes of these mergers might be subluminous SNe Ia.

In summary, mergers of white dwarfs might be able to explain some of SN Ia. It is however still debated if these events are responsible for the “normal” SNe Ia.

### 1.7.3. Constraints for different progenitor scenarios

???? structure issues????? Radio observations in the case of SNe Ia can for example reveal the shock interaction of the ejecta with the CSM. The single degenerate scenario predicts more CSM than the double degenerate scenario. Hancock et al. (2011) have stacked radio observations of SNe Ia in the visibility plane. They can not detect any source. This could hint that the double degenerate scenario is the more common, but many caveats remain.

On the other hand however Patat et al. (2007) have found variable Sodium features using high-resolution spectra of SNe Ia. These hint at the evolution of the Sodium ionization state in the CSM caused by the variable SN Ia radiation field. A wind from the donor star would provide material with the right geometric distribution to reproduce these features. Recently Patat et al. (2011) have seen similar features in the recurrent nova RS Ophiuchi. This could hint that recurrent novae with red giant donor stars might be responsible for some SNe Ia.

Kasen (2010) predicts excess in UV flux in the SN Ia light curve at early times. This effect depends on orientation of the system to the line of sight and the state of the donor. The effect would be biggest for a giant donor. Hayden et al. (2010) do not see this excess in the SDSS supernova set. This suggests that the red giant channel is not common for SNe Ia and might suggest that DD-scenario is predominant. There remain, however, many caveats. The orbits of the SD-system might be closer than expected (suggesting that the existing light-curve data is not early enough) or the effect overestimated.

It remains a mystery that SNe Ia do not show lines of Hydrogen which might be expected from the wind or stripped envelope in the SD-model. Leonard (2007) have searched in the nebular spectra of two SNe Ia for hydrogen and place an upper limit of  $0.1 M_{\odot}$  for both these explosions. One might take this as a further hint against the SD-scenario. On the other hand Justham (2011) suggest that a red giant donor could significantly shrink during the RLOF. This would place the the stripped hydrogen below the current detection limit.

[Di Stefano](#) (2010) have not found enough [SSS](#), which are suggested [SN Ia](#)-progenitors for the SD-scenario. In addition, [Gilfanov & Bogdán](#) (2010) have not found enough accumulated X-ray flux from elliptical galaxies if all [SN Ia](#)-progenitors were [SSS](#) (assuming the X-Ray flux calculated for these objects is correct). The main caveats are that the [SN Ia](#)-progenitors might only be in the [SSS](#)-phase for a moderate amount of time. In addition, these objects could be engulfed in a envelope, which would reprocess the produced X-rays to optical or infrared wavelengths.

Finding a donor star of the SD-scenario in a supernova remnant (henceforth SNR) post-explosion, would resolve the question for the progenitor system at least in the searched remnant. The main work of this thesis investigates this technique and we will refer the reader to Chapters ??.

Population synthesis together with observations of [DTDs](#) are an important step in exploring the different progenitor scenarios. [Hachisu et al.](#) (2008); [Han & Podsiadlowski](#) (2004) and suggest when compared to observations that the SD-scenario is not far from explaining the observed [DTD](#) (for references on [DTD](#) see section 1.3.2). [Ruiter et al.](#) (2009); [Mennekens et al.](#) (2010), however, have explored the [SN Ia](#)-rate using several progenitor scenarios (SD, DD and [AM CVn](#)). Both suggest that the SD-scenario on its own can not explain the observed [SNe Ia](#)-rate. The DD-rate seems to be much closer to the observed frequency. Possibly a mix of all channels is required to explain the observed rate.

In summary, the question of the progenitors is currently one of the most highly debated in [SNe Ia](#) research. There exist multiple arguments for both the SD-scenario and DD-scenario. In addition, new scenarios like the core-degenerate system in which a white dwarf merges with the hot core of a massive AGB star [Ilkov & Soker](#) (2011) are emerging. [Di Stefano et al.](#) (2011) and [Justham](#) (2011) suggest that the accreting white dwarf would be spun-up during accretion. The ignition of these highly spinning white dwarfs would be delayed and the companion might have time to evolve. This might possibly forfeit some of the arguments brought against the SD-scenario. [van Kerkwijk et al.](#) (2010) on the other hand suggests the merger of two equal mass white dwarfs with a total mass less than [M<sub>Chan</sub>](#). There remain still many caveats, but coupled with the work on sub-Chandrasekhar mass detonations by [Sim et al.](#) (2010), this might provide an interesting scenario. The main advantage is the predicted rate of these low-mass white dwarf mergers might be high enough to reproduce the observations. More and novel observations of [SNe Ia](#) and [SNR](#) will hopefully help constrain the progenitor scenario. In the community some astronomers are now suggesting a multi-channel approach to explain [SNe Ia](#) phenomenon.

## 1.8. Thesis motivation

One of the most pivotal moments in astronomy in recent years was the discovery of the accelerating expansion of the universe by Riess et al. (1998) and Perlmutter et al. (1999). This discovery catapulted SNe Ia into the limelight of the astronomical community. There has been many advances in recent years in the understanding of these cataclysmic events (explosion models, rates, etc.). One critical piece of the puzzle, however, has so far eluded discovery: The progenitors of SNe Ia. This work's main aim is to find evidence for one SN Ia-progenitor scenario. The SD-scenario proposes a white dwarf accreting from a non-degenerate donor star. To the best of our knowledge this donor star is thought to survive the explosion and would be visible thereafter. We have tried to find this companion in two of three easily accessible ancient supernova remnants (SN1572 and SN1006). In chapter ?? we have obtained spectra of Tycho-G which had been suggested as the donor star of SN1572 (Ruiz-Lapuente et al., 2004). Although we confirmed some of the suggested parameters we could not reproduce the unusually high radial velocity which led to the claim.

We revisited SN1572 in chapter ?? with new observations of Tycho-G and five other stars in the neighbourhood of SN1572. This resulted in Tycho-G to be not a very viable donor star (it is hard to completely rule stars out). We discovered a curious A-Star located serendipitously right in the center of SN1572. Despite its bizarre parameters we could not reconcile this star (Tycho-B) with any feasible progenitor model. We, however, found a scenario which explains Tycho-B's features but does not involve it in SN1572.

SN1006 provides a perfect opportunity to search for progenitor stars. It is the closest known remnant of a SN Ia (2 kpc). We have obtained 80 spectra of stars close to the center of the remnant and present them in chapter ???. Again we did not find any obvious donor stars.

We have obtained spectra of stars around SN1604 but these are not presented in this work. Progenitor hunts provide us with information of the scenarios pre-explosion. Spectra on the other hand help to unravel the happenings during and post-explosion. Mazzali et al. (2008) have developed a code that can produce synthetic SN Ia-spectra from fundamental input parameters. Fitting an observed SN Ia is for the moment a manual task. This requires many days, if not weeks, of tweaking. The deluge of spectroscopically well-sampled SNe Ia from surveys is already hitting us. Manual analysis of all these spectra is impossible. The information about the explosion hidden in the spectra is, however, crucial to our understanding of these events. In chapter 5 we present our work towards automating this fitting process. We have tried a variety of algorithms to explore the vast and extremely complex search space. Working together with members of the computer science community we are exploring the use of genetic algorithms to solve this problem. This work is not finished yet, but we present preliminary methods in SN Ia-fitting in chapter 5. Once finished we can apply this method not only in fitting SN Ia, but fitting other supernovae and in other areas of astronomy.

In summary, this work explores two areas of supernova physics: progenitors and explosion physics. The hunt for progenitors has not yielded obvious candidates, but may suggest a rethinking of the "normal" SD-scenario. The automated fitting of supernova spectra is in its infancy stage. We have however shown that it is possible to explore the parameter space

in an automated fashion. This will hopefully yield elemental abundances and energies for many thousand supernovae. The close collaboration with computer science community was very helpful and shows how important cross-disciplinary research is in this era of science.

# CHAPTER 2

---

## SN1572

### 2.1. Introduction

Type Ia supernovae (SNe Ia) are of broad interest. They serve as physically interesting end points of stellar evolution, are major contributors to galactic chemical evolution, and serve as one of astronomy's most powerful cosmological tools.

It is therefore unfortunate that the identity of the progenitors of SNe Ia is still uncertain. For example, without knowing the progenitors, the time scales of SNe Ia enriching the interstellar medium with iron remains highly uncertain. But it is the crippling impact on the cosmological application of these objects which is especially profound; it is impossible to predict the consequences of any cosmological evolution of these objects or even gauge the likelihood of such evolution occurring.

There is broad agreement that the stars which explode as SNe Ia are white dwarfs which have accreted material in a binary system until they are near the Chandrasekhar mass, then start to ignite carbon explosively, which leads to a thermonuclear detonation/deflagration of the star. It is the identity of the binary companion that is currently completely undetermined. Suggestions fall into two general categories ([Iben, 1997](#)):

- Single degenerate systems in which a white dwarf accretes mass from a non-degenerate companion, where the companion could be a main-sequence star, a subgiant, a red giant, or possibly even a subdwarf.
- Double degenerate systems where two CO white dwarfs merge, resulting in a single object with a mass above the Chandrasekhar limit.

The detection of circumstellar material around SN 2006X ([Patat et al., 2007](#)) has provided support for the single degenerate model in this case, although the lack of substantial hydrogen in several other SNe Ia ([Leonard, 2007](#)) poses more of a challenge to this scenario.

These models also make different predictions for the nature of the system following the explosion. In the double degenerate case, no stellar object remains, but for a single white dwarf, the binary companion remains largely intact.

In the single degenerate case, the expected effect of the SN on the donor star has been investigated by Marietta, Burrows, & Fryxell (2000), who have calculated the impact of a SN Ia explosion on a variety of binary companions. Canal, Méndez, & Ruiz-Lapuente (2001) have explored many of the observational consequences of the possible scenarios, and Podsiadlowski (2003) has presented models that follow both the pre-supernova accretion phase and the post-explosion non-equilibrium evolution of the companion star that has been strongly perturbed by the impact of the supernova shell. To summarize these results, main-sequence and subgiant companions lose 10–20 % of their envelopes and have a resulting space velocity of  $180\text{--}320 \text{ km s}^{-1}$ . Red-giant companions lose most of its hydrogen envelope, leaving a helium core with a small amount of hydrogen-rich envelope material behind, and acquire a space velocity of about  $10\text{--}100 \text{ km s}^{-1}$ . Pakmor et al. (2008) have used a binary stellar evolution code on a main-sequence star and exposed the evolved star to a SN Ia. Their simulations show that even less material is stripped due to the compact nature of a star that evolved in a binary. We will use their results where applicable.

Ruiz-Lapuente et al. (2004, henceforth RP04) have identified what might be the donor star to Tycho’s SN, a SN Ia which exploded in the Milky Way in 1572. These authors presented evidence that this star, Tycho-G by their naming convention, is at a distance consistent with the Tycho supernova remnant (henceforth SNR), has a significant peculiar radial velocity and proper motion, roughly solar abundance, and a surface gravity lower than a main-sequence star. However, Tycho-G is located at a significant distance from the inferred center of the remnant, and any process that has displaced the star must preserve the remnant’s nearly perfectly circular projected shape. During the final stages of refereeing of this paper we were made aware of the article by Hernandez et al. (2009, henceforth GH09), who used Keck HIRES data to better constrain Tycho-G’s stellar parameters, and in addition, found an enhancement in Nickel abundance, relative to normal metal rich stars.

Ihara et al. (2007) have looked for Fe absorption lines from the remnant, using nearby stars as continuum sources, with the hope to better constrain the distance of these stars to the SNR. With their technique, stars in the remnant’s center should show strong blue-shifted Fe absorption lines, formed by material in the expanding shell of Fe-rich material from the SN, moving towards the observer. Stars in the foreground would show no Fe absorption, and background stars both red- and blue-shifted absorption. Their study shows that Tycho-G does not contain any significant blue-shifted Fe absorption lines, suggesting that Tycho-G is in the remnant’s foreground. However, these observations and their analysis, while suggestive, cannot be considered a conclusive rebuttal of Tycho-G’s association with the remnant; this technique requires a significant column depth of Fe which is not guaranteed. A lack of Fe column depth may be indicated by the fact that no stars were found in the vicinity of the remnant that showed both blue- and red-shifted absorption lines.

To further examine the RP04 suggested association of Tycho-G with the SN Ia progenitor, we have obtained a high-resolution spectrum of the star using Subaru and its High Dispersion Spectrograph (Noguchi et al., 1998).

We summarize, in section 2, the observational circumstances of the Tycho remnant and any donor star, and argue in section 3 that rapid rotation is an important, previously unrealised signature in a SN Ia donor star. In section 4 we describe our Subaru observations. Section 5 covers the analysis of data and the results of this analysis. Section 6 compares the relative

merit for Tycho-G being the donor star to the Tycho SN or being an unrelated background star, and in section 7 we summarize our findings and motivate future observations.

## 2.2. Observational Characteristics of the Tycho Remnant and Star-G

RP04 have done a thorough job summarizing the relevant details of the Tycho remnant. The remnant shows the characteristics expected of a SN Ia based on its light curve (measured by Tycho Brahe himself), chemical abundances, and current X-ray and radio emission (Ruiz-Lapuente, 2004). In figure 2.1 we have overlaid radio contours<sup>1</sup> on an optical image and have marked the position of the stars mentioned in this and RP04's work.

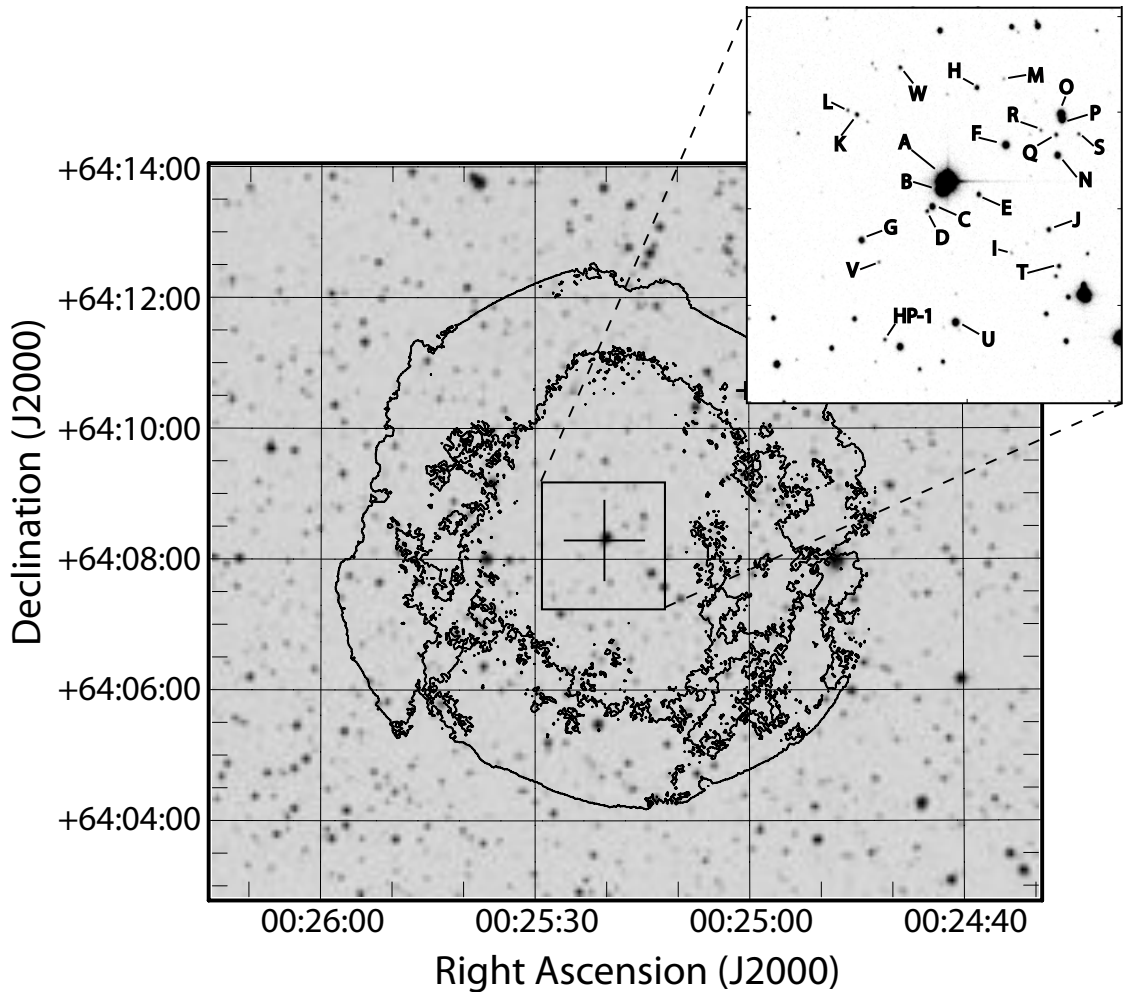


**Figure 2.1** Radio Contours (VLA Project AM0347) have been overlaid (Gooch, 1996) on an R-Band Image (NGS-POSS). The cutout is an INT image (see text). The stars marked in the figure are mentioned in this work and in RP04's work.

Although it is not easy to measure the remnant's distance precisely, RP04 estimated Tycho's

---

<sup>1</sup>The National Radio Astronomy Observatory is a facility of the National Science Foundation operated under cooperative agreement by Associated Universities, Inc.

SNR distance to be  $2.8 \pm 0.8$  kpc, using the ratio of the SN 1006 and Tycho SNR's angular sizes and their relative ages, and the direct distance measure of SN 1006 by Winkler, Gupta, & Long (2003). Krause et al. (2008) have recently shown, from a spectrum of a light echo associated with the SN1572, that this SN was a normal SN Ia. Using Tycho's observed light curve, the properties of SN Ia as standard candles, and an extinction value they find a distance to the SN of  $3.8^{+1.5}_{-1.1}$  kpc. Updating their values for the extinction values determined in this paper (section 2.6.1), as well as using an absolute magnitude for SN Ia of  $-19.5 \pm 0.25$  (Altavilla et al., 2004), we find a distance of  $3.4^{+1.3}_{-1.0}$  kpc. In summary, we believe the remnant's distance is poorly constrained, but probably between 2 and 4.5 kpc. RP04 also report the spectroscopic and photometric properties for the bright stars near the center of the Tycho remnant and find a uniform value of approximately  $E(B - V) = 0.6$  for stars more distant than 2 kpc. GH09 have revised the  $E(B - V)$  value for Tycho-G to 0.76.

In addition, for a select list of stars, RP04 provide radial velocities and proper motions. For Tycho-G, RP04 report a value of  $v_r = -99 \pm 6$  km s $^{-1}$  for the radial velocity in the Local Standard of Rest (henceforth LSR), a proper motion of  $\mu_b = -6.1 \pm 1.3$  mas yr $^{-1}$ ,  $\mu_l = -2.6 \pm 1.3$  mas yr $^{-1}$ ,  $\log g = 3.5 \pm 0.5$ , and  $T = 5750$  K. Using HIRES data GH09 have improved the measurements of Tycho-G's stellar parameters, finding  $v_r \approx -80$  km s $^{-1}$ ,  $\log g = 3.85 \pm 0.3$ ,  $T = 5900 \pm 100$  K, and [Fe/H] =  $-0.05 \pm 0.09$  dex. We note that Ihara et al. (2007) have classified Tycho-G as an F8V star ( $T \approx 6250$  K,  $\log g \approx 4.3$ , Aller et al. 1982), in significant disagreement with the RP04 temperature and gravity. We believe the GH09 values are based on by far the best data, and for the purpose of this paper, we will adopt their values.

Based on the observations, RP04 asserted that Tycho-G was located at approximately  $3 \pm 0.5$  kpc – consistent with the remnant's distance. They note that this star has solar metallicity, and therefore its kinematic signature was not attributable to being a member of the Galactic halo. They further argued that Tycho-G's radial velocity and proper motion were both inconsistent with the distance, a simple Galactic rotation model, and the star being part of the disk population of the Milky Way. The derived physical characteristics of the system were nearly identical to what was proposed by Podsiadlowski (2003) for a typical SN Ia donor star emerging from a single degenerate system (e.g., U Sco; also see Hachisu et al., 1996; Li & van den Heuvel, 1997; Hachisu et al., 1999a; Han & Podsiadlowski, 2004; Han, 2008). The revision in the stellar parameters by GH09 leads to different distance with a larger uncertainty, but by and large, has not altered the conclusions above. Taken in total, the data provide a rather convincing case for the association of Tycho-G with the Tycho SN.

### 2.3. Rapid Rotation: A Key Signature in SN Ia Donor Stars

In the single degenerate SN Ia progenitor channel, mass is transferred at a high rate from a secondary star onto a white dwarf (Nomoto, 1982; Nomoto et al., 2007). These high mass-transfer rates require that the secondary star overflows its Roche lobe. Due to the strong tidal coupling of a Roche-lobe filling donor, the secondary is expected to be tidally locked to the orbit (i.e., have the same rotation period as the orbital period). At the time of the SN explosion, the donor star is released from its orbit, but will continue with the same

space velocity as its former orbital velocity and continue to rotate at its tidally induced rate.

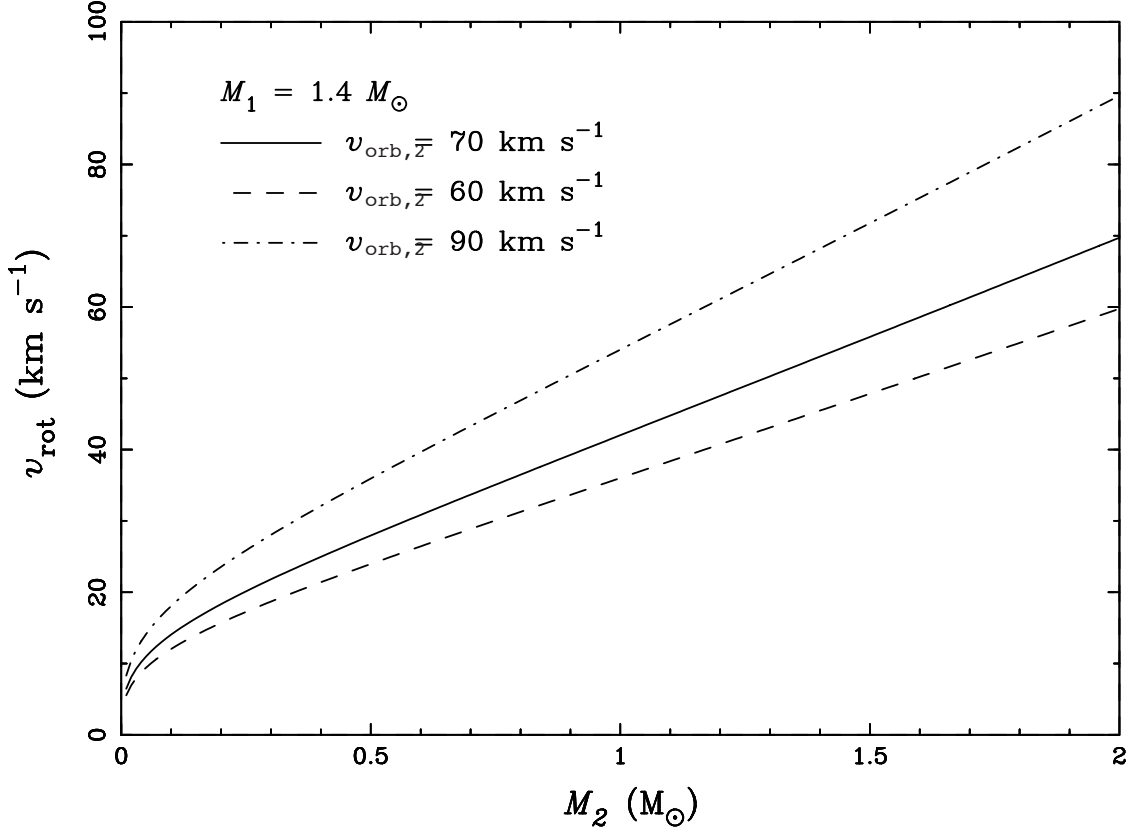


**Figure 2.2** The expected rotation rate for a donor star as a function of its mass at the time of the explosion. The three curves show the results for 3 final space velocities of the donor star (similar to those suggested by RP04). It is assumed that the white dwarf has a mass of  $1.4 M_\odot$ .

There is a simple relationship between the secondary's rotation velocity ( $v_{\text{rot}}$ ) and its orbital velocity:

$$v_{\text{rot}} = \frac{M_1 + M_2}{M_1} f(q) v_{\text{orb},2},$$

where  $f(q)$  is the ratio of the secondary's Roche-lobe radius to the orbital separation (e.g., given by [Eggleton, 1983](#)) and  $q = M_1/M_2$  is the mass ratio of the components at the time of the explosion. Figure 2.2 shows the rotational velocity as a function of secondary mass for several values of  $v_{\text{orb},2}$  (consistent with RP04's measurement, and at the low end of values expected for a subgiant star), where we assumed that the exploding white dwarf had a mass of  $1.4 M_\odot$ .

This estimate is strictly speaking an upper limit, as it does not take into account the angular-momentum loss associated with the stripping of envelope material by the supernova and any bloating due to the supernova heating. The latter would reduce the rotational velocity to first order by a factor equal to the bloating factor (i.e. the ratio of the new to the old radius), but the star would likely find itself in a state where its radius and temperature was atypical of a normal star.

According to the results of [Marietta et al. \(2000\)](#), mass stripping is not likely to be significant if the companion is a main-sequence star or a subgiant. Furthermore, following binary evolution of a main-sequence star, [Pakmor et al. \(2008\)](#) have shown that even less material is stripped. However, if the companion is a giant, it would be stripped of most of its envelope. Such a star would not show any signs of rapid rotation since the initial giant would have been relatively slowly rotating; e.g., if one assumes solid-body rotation in the envelope, the rotation velocity at  $\sim 1 R_\odot$  will only be  $\sim 0.5 \text{ km s}^{-1}$  for a pre-SN orbital period of 100 d. Moreover, the material at the surface may have expanded from its original radius inside the giant, further reducing the rotational velocity. However, if the stripping is less than estimated by [Marietta et al. \(2000\)](#), then it is possible for the signature of rotation to persist for a giant, albeit at a much lower velocity.

[Marietta et al. \(2000\)](#) also showed that due to the interaction of the SN blast wave with the companion, the secondary may receive a moderate kick of up to a few  $10 \text{ km s}^{-1}$ , but this kick is generally much lower than  $v_{\text{orb},2}$  and therefore does not significantly affect the resulting space velocity.

Finally, we note that the observed rotation velocities are reduced by a factor  $\sin i$ , where  $i$  is the inclination angle. However, because the donor star's rotational axis can be assumed to be parallel to its orbital axis, a minimum observed rotation speed can be computed from the observed peculiar radial velocity (observed radial velocity minus the expected radial velocity of an object at that distance and direction). It is only if the orbital motion (and hence final systemic velocity) is solely in the plane of the sky, that  $\sin i$ , and therefore, the observed rotation, approaches zero.

## 2.4. Subaru Observations

To investigate the rotational properties of Tycho-G, we were granted time with the Subaru telescope. Our observations of Tycho-G were taken in service mode on the nights of 2005 10 17 and 2005 10 18. 9 spectra were taken with the High Dispersion Spectrograph (HDS, [Noguchi et al., 1998](#)) with a resolution of  $R \approx 40000$  (measured using the instrumental broadening of the Thorium-Argon arc lines), an exposure time of 2000 seconds each (totalling to 5 hours) and a signal to noise ratio of about 10 per pixel (measured at  $8300 \text{ \AA}$  with  $0.1 \text{ \AA pixel}^{-1}$ ). The HDS features two arms, with each arm feeding a 2-chip CCD mosaic. The blue arm covers  $6170 \text{ \AA}$  to  $7402 \text{ \AA}$  and the red arm  $7594 \text{ \AA}$  to  $8818 \text{ \AA}$ . An OG530 filter was used to block contamination from light blueward of our observing window, and data were binned by 4 in both the spatial and spectral directions, resulting in a pixel size of  $0.1 \text{ \AA}$  (at  $8000 \text{ \AA}$ ) by  $0.55''$ .

Data were pre-processed using tools provided by the HDS team and then bias-subtracted. We created a mask from bias and flatfielded frames, where we isolated the echelle orders and flagged bad pixel regions. The data were flatfielded using internal quartz flats, and the 2-D images cleaned of cosmic rays (and checked carefully by eye to ensure there were no unintended consequences) using an algorithm supplied by M. Ashley (private communication). The spectrum of each echelle order was extracted using IRAF<sup>2</sup> echelle

---

<sup>2</sup>IRAF is distributed by the National Optical Astronomy Observatory, which is operated by the Association of Universities for Research in Astronomy (AURA) under cooperative agreement with the National Science Foundation.

routines, with wavelength calibrations based around low-order fits of a Thorium-Argon arc. Wavelength calibration of each extracted spectrum was checked against atmospheric O<sub>2</sub>, and our solutions were found to be accurate in all cases to within 1 km s<sup>-1</sup> (Caccin et al., 1985). Unfortunately, we lacked a smooth spectrum standard star for setting the continuum, and we resorted to calculating a median of the spectra (6 Å window) and dividing the spectra through this smoothed median. This unusual method was chosen over the common approach of fitting the spectrum with a polynomial, due to the special characteristics of this observation (low signal to noise ratio, and a complex instrumental response). While this does not affect the narrow lines our program was targetting, it does affect broad lines such as the H $\alpha$  and the CaII IR triplet. The final step was to combine all spectra and remove any remaining cosmic rays (in the 1D spectra) by hand.

## 2.5. Analysis and Results

### 2.5.1. Rotational measurement

To attain the rotational velocity of the candidate star, we measured several unblended and strong (but not saturated) Fe I lines in the spectrum (Wehrse, 1974). Since our spectrum only had a combined signal to noise ratio of approximately 10, we added the spectra of the lines after normalizing them to the same equivalent width. As a reference we created three synthetic spectra (one broadened only with the instrumental profile, the others with the instrumental profile and  $v_{\text{rot}} \sin i$  of 10 and 15 km s<sup>-1</sup> respectively) with the 2007 version of MOOG (Sneden, 1973), using GH09's temperature, gravity and metallicity. We use a standard value of  $\beta = 3/2$  for the limb darkening although the choice of this value is not critical, which we confirmed by checking our results using significantly different values of  $\beta$ . Figure 2.3 shows the comparison between the synthetic spectra of different rotational velocity and the spectrum of Tycho-G. We have scaled the synthetic spectrum using the equivalent width. This comparison indicates that the stellar broadening (rotational, macro turbulence, etc.) is less than broadening due to the instrumental profile of 7.5 km s<sup>-1</sup>, and therefore we adopt 7.5 km s<sup>-1</sup> as our upper limit to the rotation of the star. If one were to adopt RP04's measurements of the peculiar spatial motion, it could be concluded that  $\sin i$  is much closer to 1 than 0 (see the end of section 2.3 for further explanation) and thus that the rotational speed is  $v_{\text{rot}} \lesssim 7.5$  km s<sup>-1</sup>.

### 2.5.2. Radial velocity

To determine the radial velocity, we used 63 lines to measure the shift in wavelength. We find a radial velocity in the topocentric (Mauna Kea) frame of reference of  $v_{\text{top}} = -92.7 \pm 0.2$  km s<sup>-1</sup> (the error being the standard deviation of 63 measurements). The conversion from the topocentric to the Galactic LSR for our observations was calculated to be 13.6 km s<sup>-1</sup> (IRAF task rvcorrect) using the IAU standard of motion. Including the uncertainty in the LSR definition, we find a radial velocity in the LSR for Tycho-G of  $v_{\text{LSR}} = -79 \pm 2$  km s<sup>-1</sup>. This is in significant disagreement with that reported by RP04, but agrees with the revised value published by GH09.

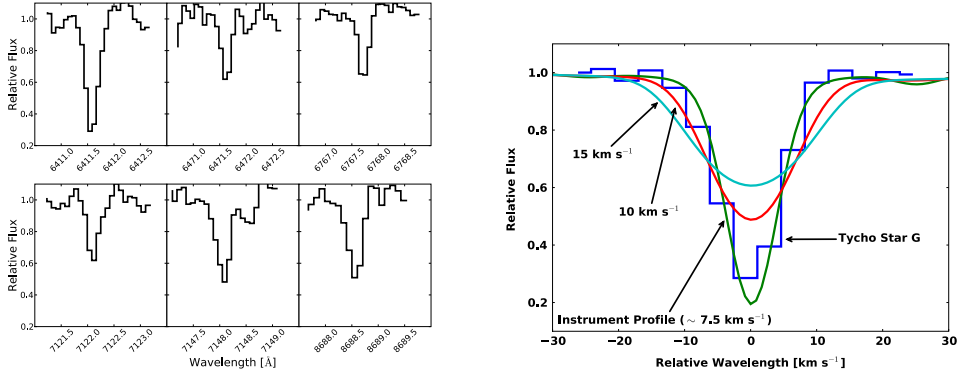


**Figure 2.3** Six observed Fe I line profiles of Tycho-G are shown on the left panel. The right panel shows the combination of these line profiles after normalization to the same equivalent width and compares them to the spectrum of the Sun, which is convolved with 3 different values for the rotational broadening kernel. Tycho-G does not show significant rotation, indicating  $v_{\text{rot}} \sin i \lesssim 7.5 \text{ km s}^{-1}$ .

### 2.5.3. Astrometry

RP04 have measured a significant proper motion for Tycho-G of  $\mu_b = -6.1 \pm 1.3 \text{ mas yr}^{-1}$ ,  $\mu_l = -2.6 \pm 1.3 \text{ mas yr}^{-1}$ . Because Tycho-G is metal rich, and at a distance of  $D > 2 \text{kpc}$ , this measurement provides one of the strongest arguments for Tycho-G being the donor star to Tycho SN. It is almost impossible to account for this proper motion, equivalent to a  $v_b = 58 \left( \frac{D}{2 \text{kpc}} \right) \text{km s}^{-1}$  or 3 times the disk's velocity dispersion of  $\sigma_z = 19 \text{km s}^{-1}$ , except through some sort of strong binary star interaction.

However, the HST data present an especially difficult set of issues in obtaining astrometry free of systematic errors. For Tycho-G these issues include the PSF on the first epoch WFPC2 image being grossly undersampled, both the ACS and WFPC2 focal planes being highly distorted, poor and different charge transfer efficiency across the two HST images, and that Tycho-G was, unfortunately, located at the edge of one of the WFPC2 chips, making it especially difficult to understand the errors associated with it. Smaller issues include the small field of overlap between the two images, making the measurement subject to issues of the correlated motions of stars, especially in the  $\mu_l$  direction.

To cross-check RP04's proper motion of Star-G, we have scanned a photographic plate taken in September 1970 on the Palomar 5 meter, and compared this to an Isaac Newton 2.5 m Telescope (INT) CCD archive image (INT200408090414934) of the remnant taken in August 2004. The Palomar plate has an image FWHM of 1.7'', and the INT image 0.88''. While our images have a much larger PSF than the HST images, the images have significantly less distortion, are matched over a larger field of view with more stars, have fully sampled PSFs, and were taken across nearly an 8 times longer time baseline. The photographic nature of the first epoch does add complications not present in the HST data. The non-linear response of photographic plates causes their astrometry to have systematic effects as a function of brightness (Cannon et al., 2001), especially affecting objects near the plate limit, where single grains are largely responsible for the detection of an object.

The position of stars on the INT image were matched to the 2MASS point source catalog (Skrutskie et al., 2006) to get a coordinate transformation (pixel coordinates to celestial

coordinates) using a 3rd-order polynomial fit with an RMS precision of 40 mas with 180 stars. This fit is limited by precision of the 2MASS catalog and shows no systematic residuals as a function of magnitude, or position. Using this world coordinate system (WCS) transformation, we then derived the positions of all stars on the INT image. The coordinates of 60 uncrowded stars on the Palomar plate were matched to the INT-based catalog, and a 3rd-order polynomial was used to transform the Palomar positions to the INT-based positions. The fit has an RMS of 65 mas in the direction of galactic longitude, and 45mas in the direction of galactic latitude. We believe the larger scatter in the direction of Galactic longitude is due to the shape of the PSF being slightly non-symmetric in the direction of tracking on the Palomar plate. This tracking (in RA, which is close to the direction of galactic longitude), causes the position of stars to depend slightly on their brightness. This explanation is supported by a small systematic trend in our astrometric data in  $\mu_l$ , not seen in  $\mu_b$ , as a function of  $m_R$ . An alternative explanation is that the trend in  $\mu_l$  is caused by the average motion of stars changing due to galactic rotation as a function of distance, which is proxied by  $m_R$ . We have used the Besançon Galactic model (Robin et al., 2003) to estimate the size of any such effect, and find the observed effect is an order of magnitude larger than what is expected. The systemic difference between assuming either source of the observed effect is less than 1 mas yr<sup>-1</sup> in  $\mu_l$ , and has no effect in our  $\mu_b$  measurement. In our final proper motions, presented in table 2.1, we remove the systematic trend as a function of  $m_R$  with a linear function.

**Table 2.1** Proper motions of stars within 45'' of the Tycho SNR center.

$\alpha$ [hh:mm:ss.ss]	$\delta$ [dd:mm:ss.ss]	$\mu_l$ [mas yr <sup>-1</sup> ]	$\mu_b$ [mas yr <sup>-1</sup> ]	$m_R$ [mag]	$\theta$ [arcsec]	Name
00:25:20.40	+64:08:12.32	-0.90	-0.56	17.05	08.9	c
00:25:18.29	+64:08:16.12	-4.25	-0.81	18.80	10.0	e
00:25:17.10	+64:08:30.99	-1.82	1.78	16.87	20.3	f
00:25:23.58	+64:08:02.02	-1.58	-2.71	17.83	31.1	g
00:25:15.52	+64:08:35.44	1.94	0.83	20.28	31.4	r
00:25:15.08	+64:08:05.95	-0.67	1.49	18.86	33.3	j
00:25:23.89	+64:08:39.33	-0.31	1.08	19.20	33.5	k
00:25:14.74	+64:08:28.16	2.60	1.46	17.45	33.5	n
00:25:14.81	+64:08:34.22	4.05	-2.05	19.35	35.0	q
00:25:13.79	+64:08:34.50	2.32	1.01	19.90	41.3	s
00:25:14.59	+64:07:55.10	-3.94	2.35	19.23	41.7	t
00:25:19.25	+64:07:38.00	1.75	-3.43	16.86	42.1	u
00:25:22.45	+64:07:32.49	81.29	-2.68	19.81	48.7	HP-1

To measure the proper motion of each star, we exclude each star from the astrometric transformation fit so as not to bias its proper motion measurement. Comparing the stellar positions in the 34 year interval we find that these 60 stars show an RMS dispersion  $\sigma_{\mu_l} = 2.1 \text{ mas yr}^{-1}$ ,  $\sigma_{\mu_b} = 1.6 \text{ mas yr}^{-1}$ . For Tycho-G we measure  $\mu_l = -1.6 \pm 2.1 \text{ mas yr}^{-1}$ ,  $\mu_b = -2.7 \pm 1.6 \text{ mas yr}^{-1}$ ; this implies that no significant proper motion is detected. We do note that this measurement has a similar precision to that of RP04, is consistent with no observed motion, and is in moderate disagreement with the RP04 measurement.

In table 2.1 we present our astrometric measurements of all stars listed by RP04 for which

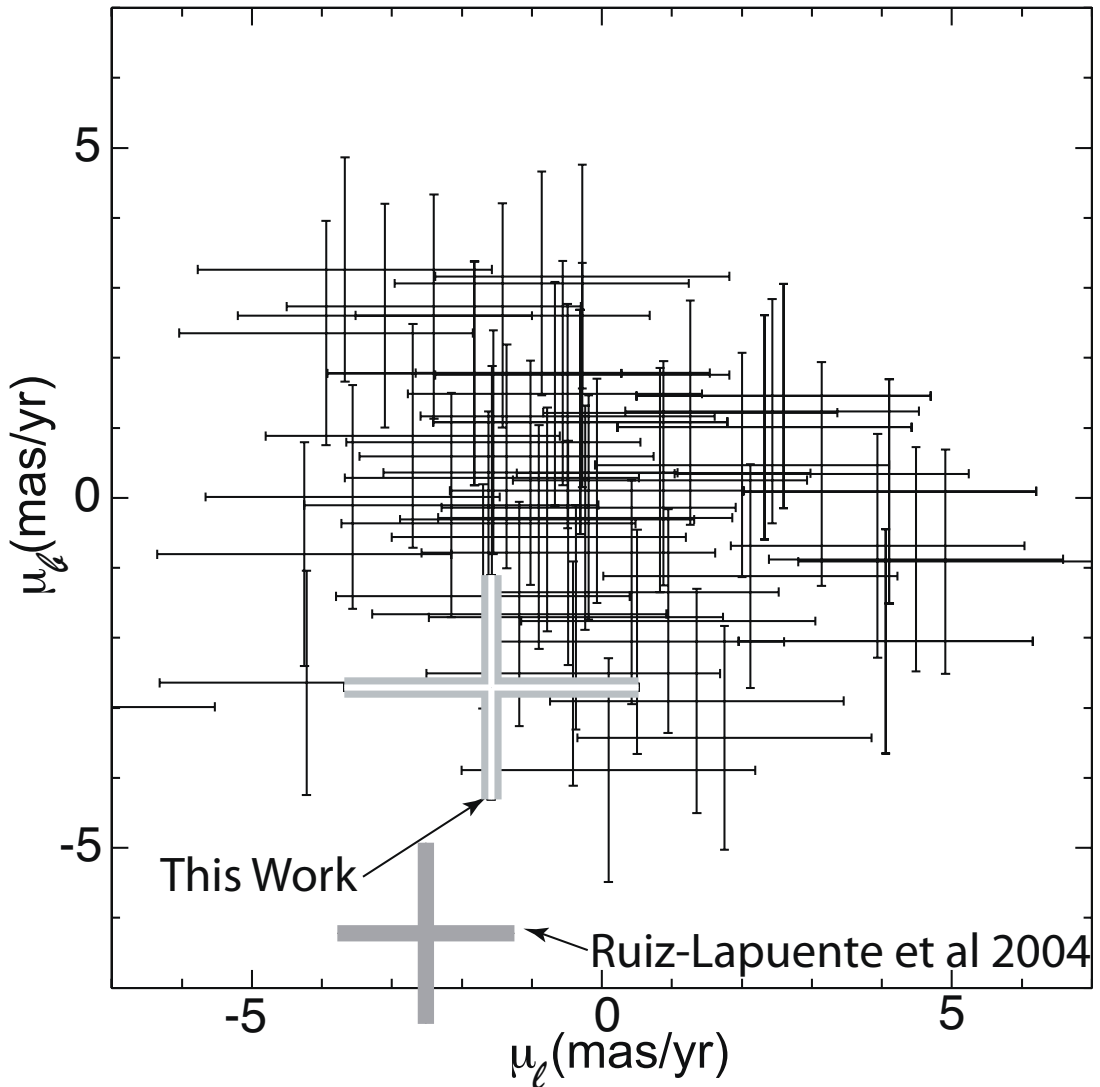


**Figure 2.4** The astrometric motions of 60 stars measured in the Tycho SNR center. The measurements have a RMS dispersion of  $1.6 \text{ mas yr}^{-1}$ . Shown in grey is the proper motion of Tycho-G measured here and by RP04, showing a moderate discrepancy in the two measurements. Our measurement is consistent with no proper motion.

we were able to measure proper motions. We also give the apparent magnitudes in R (partly measured by this work and partly by RP04) and the distance from center  $\theta$ . Due to crowding caused by the relatively poor resolution of the first epoch photographic plate, several stars are not included that could be measured using HST. We include an additional star, not cataloged by RP04, which exhibits high proper motion. This high proper motion star, which was off the WFPC2 images of RP04, we designate HP-1, and has a proper motion of  $\mu_l = 81.3$ ,  $\mu_b = -2.7 \text{ mas yr}^{-1}$ . Due to the distance from the remnant's center, (we estimate HP-1 would have been located  $51''$  from the remnant's center in 1572), we doubt this star is connected to the Tycho SN, but we include it for the sake of completeness.

## 2.6. Discussion

### 2.6.1. A Background interloper?

A previously unrecognized property for many progenitor scenarios is the rapid post-explosion rotation of the donor (as described in Section 2.3). The expected rotation as calculated in Figure 2.2 is large compared to that expected of stars with a spectral type later than F and should be easily observable. We have shown Tycho-G’s rotation to be less ( $v_{\text{rot}} \sin i \lesssim 7.5 \text{ km s}^{-1}$ ) than what is expected of an associated star if the companion was a main-sequence star or subgiant. A red giant scenario where the envelope’s bloating has significantly decreased rotation could be consistent with our observation of Tycho-G, and this will be discussed in section 2.6.2.

The primary basis for which RP04 selected Tycho-G as a candidate for the donor star to the Tycho SN was the combination of its large peculiar radial velocity and its observed proper motion. In Figure 2.5 we use the Besançon Galactic model (Robin et al., 2003) to construct an expected set of radial velocities for metal-rich stars in the direction of SN1572.

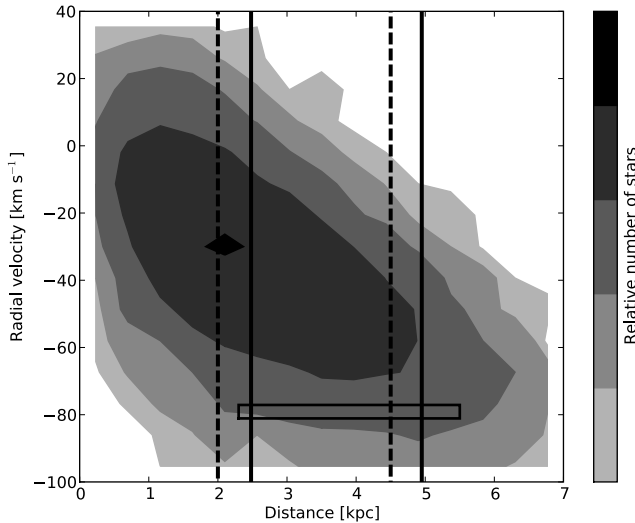


**Figure 2.5** Besançon model for a metal rich ( $[\text{Fe}/\text{H}] > -0.2$ ) Galactic population between 0 and 7 kpc in the direction of Tycho SNR ( $\ell = 120.1$ ,  $b=1.4$ ) with a solid angle of 1 square degree. The remnant’s distance is represented by the black dashed lines (as calculated in section 2.2). The contours show the radial velocity distribution. Our measured radial velocity corrected to LSR and our distance are shown, with their respective error ranges, as the black rectangle. The distance range calculated by GH09 are indicated by the two solid lines. The observed LSR  $v_r$  for Tycho-G is mildly unusual for stars at the remnant’s distance, and is consistent with the bulk of stars behind the remnant.

Measuring the distance to Tycho-G is a key discriminant in associating the star to the SN explosion. To improve the uncertainty of the distance to the star, due both to temperature and extinction uncertainty, we base our distance on the observed  $m_K$  (Skrutskie et al., 2006) and  $(V - K)$  color (RP04). We interpolate ATLAS9 models without overshoot (Bessell, Castelli, & Plez, 1998) to find a theoretical  $V - K$  and absolute magnitude for the GH09’s values of temperature and gravity. Using a standard extinction law (Cardelli, Clayton, &

(Mathis, 1989) ( $A_V = 3.12E(B-V)$  and  $A_K/A_V = 0.109$ ) to match the theoretical and observed colors, we find  $A_V = 2.58 \pm 0.08$  mag,  $A_K = 0.28 \pm 0.01$  mag, and  $E(B-V) = 0.84 \pm 0.05$ . To better show the uncertainties, we present our distance moduli scaled to the observed and derived values of extinction, temperature and gravity. The temperature coefficients were determined by integrating blackbodies of the appropriate temperature with a filter bandpass and fitting a powerlaw to the resulting flux.

$$(m_V - M_V) = 12.93 - 3.12(E(B-V) - 0.84) - 2.5(\log g - 3.85) + \\ + 2.5 \log\left(\frac{M}{1 M_\odot}\right) + 2.5 \log\left(\frac{T_{\text{eff}}}{5900}\right)^{4.688} \quad (2.1)$$

$$(m_K - M_K) = 12.93 - 0.275(E(B-V) - 0.84) - 2.5(\log g - 3.85) + \\ + 2.5 \log\left(\frac{M}{1 M_\odot}\right) + 2.5 \log\left(\frac{T_{\text{eff}}}{5900}\right)^{1.937} \quad (2.2)$$

Assuming a companion mass of  $1 M_\odot$  we find a  $(m-M) = 12.93 \pm 0.75$  mag. This uncertainty is dominated by the precision of  $\log g$ , and equates to a distance of  $D = 3.9 \pm 1.6$  kpc. Tycho-G, within the errors, is at a distance consistent with the remnant. As seen in Figure 2.5, the observed radial velocity of Tycho-G is consistent with a significant fraction of stars in its allowed distance range. We also note that if Tycho-G is indeed associated with the SN, that it is likely that Tycho-G could have a mass considerably less than  $1 M_\odot$ , due to mass transfer and subsequent interaction with the SN, although in this case, the distance to the star would still be consistent with SNR distance.

Ihara et al. (2007) looked for absorption due to Fe I in the remnant's expanding ejecta for 17 stars within the Tycho remnant. No such absorption was seen in the spectrum of Tycho-G, potentially placing it in front of the remnant. However, the amount of Fe I currently within the remnant is uncertain with predicted column densities spanning several orders of magnitude ( $0.02 - 8.9 \times 10^{15}$  cm $^{-2}$ ; Hamilton & Fesen, 1988; Ozaki & Shigeyama, 2006). Therefore, we do not believe the lack of significant Fe I 3720 absorption in Tycho-G to be significant.

In summary, we find that Tycho-G's radial velocity, distance, and stellar parameters are all consistent with an unrelated star, but also with it being the donor star. There is disagreement in Tycho-G's measured proper motion. The measurements of RP04 are inconsistent with normal disk stars at the known distance and strongly point to Tycho-G being associated with the SN, whereas the measurements presented here are consistent with a normal disk star, unrelated to the SN. In addition, we have shown the rotation of Tycho-G is low (confirmed by GH09;  $v_{\text{rot}} \leq 6.6$  km s $^{-1}$ ), arguing against association with the SN, as does its off center placement in the remnant. Finally, GH09 have presented evidence that Tycho-G is strongly enhanced in Nickel, an observation that, if confirmed, would strongly point to an association of the star with the SN. If either the high proper motion, or significant Nickel enhancement can be confirmed, then it is likely that Tycho-G is the SN donor star. Otherwise, we believe it is much more likely that Tycho-G is simply an interloper.

### 2.6.2. Tycho-G as the Donor Star to the Tycho SN

While the case for Tycho-G’s association with the SN is not conclusive, it is intriguing, and we believe it is worthwhile to look for a consistent solution assuming the association is true. While not apriori probable, a self-consistent model can be constructed in which Tycho-G was the companion, as we shall discuss now.

To make such a model work, Tycho-G has to be a stripped giant that presently mimics a G2IV star. At the time of the explosion, the star would have been a moderately evolved giant (in a binary with an orbital period  $\sim 100$  d). The SN ejecta will strip such a giant of almost all of its envelope (Marietta et al., 2000) due to its low binding energy; only the most tightly bound envelope material outside the core will remain bound. Due to the heating by the SN, even this small amount of material (perhaps a few  $\times 0.01 M_{\odot}$ ) will expand to giant dimensions, and the immediate-post-SN companion will have the appearance of a luminous red giant. However, because of the low envelope mass, the thermal timescale of the envelope is sufficiently short that it can lose most of its excess thermal energy in 400 years and now have the appearance of a G2IV star (Podsiadlowski, 2003).

A lower mass for Tycho-G ( $0.3 - 0.5 M_{\odot}$ ) also reduces the distance estimate, and makes the observed radial velocity more unusual for stars at this distance. The expected spatial velocity depends on the pre-SN orbital period and should be in the range of  $30 - 70 \text{ km s}^{-1}$  for a period range of  $20 - 200$  d (Justham et al., 2008). These velocities are consistent with the inferred spatial velocity of the object relative to the LSR if Tycho-G is at the distance of the remnant, even if no significant proper motion has been measured (see Figure 2.5).

A stripped-giant companion would link the progenitor to the symbiotic single-degenerate channel (Hachisu et al., 1999b) for which the symbiotic binaries TCrB and RS Oph are well studied candidates. Indeed, (Justham et al., 2008) argued that the ultracool low-mass helium white dwarfs (with masses  $> 0.3 M_{\odot}$ ) that have been identified in recent years are most likely the stripped-giant companions that survived SN Ia explosions, which could provide some further possible support for such a scenario for Tycho-G.

If the association is real, Tycho-G’s displacement to the SE of the geometric center of the remnant as defined by radio and X-ray observations might be interpreted as being due to the remnant’s interaction with an inhomogeneous ISM. Deep optical images of the remnant do show extended diffuse emission along the eastern and northeastern limbs interpreted as shock precursor emission (Ghavamian et al., 2000). This along with an absence of detected Balmer-dominated optical emission along the whole of the western and southern limbs suggests a density gradient of the local interstellar medium with increasing density towards the NE. An east-west density gradient has also been inferred from detailed radio expansion rate measurements (Reynoso et al., 1997). Such an E-W density gradient could have led to a more rapid expansion toward the west giving rise to a small shift in the apparent geometric center away from the SE without creating a highly distorted remnant. However, there are problems with this explanation. Deviations from spherical symmetry in both radio and X-ray images of the remnant are relatively small (Reynoso et al., 1997; Cassam-Chenai et al., 2007), and the remnant is most extended along the eastern and northeastern limbs, just where one finds the greatest amount of extended diffuse optical emission. Moreover, the remnant’s expansion rate appears lowest toward the northeast (PA = 70 degrees), not the southeast (Reynoso et al., 1997). Although the

argument that Tycho-G’s SE displacement from the remnant’s current geometric center is a result of an asymmetrical expansion is not strong, it remains a possibility.

The most conclusive way of confirming a stripped-giant scenario for Tycho-G would be an independent, precise measurement of the distance to Tycho-G which in combination with measurements of the gravity and effective temperature would help to constrain Tycho-G’s mass. Unfortunately, such a measurement will most likely have to wait for the advent of the GAIA satellite. Alternatively, one may be able to single out a stripped giant from a normal G2IV star through nucleosynthesis signatures, specifically evidence for CNO-processed material (or other nucleosynthetic anomalies). While a normal G2IV star is unlikely to show CNO-processed material at the surface, a stripped giant is likely to do so. Unfortunately, the data presented here are not of adequate quality to explore the detailed properties of Tycho-G’s atmosphere.

## 2.7. Outlook and Future Observations

Presently, we believe the evidence for Tycho-G’s association with the Tycho SN is interesting, but not conclusive. A possible scenario if Tycho-G is the donor star, would be that of a stripped giant scenario discussed in section 6. However, there are still other stars that have not been adequately scrutinized. [Ihara et al. \(2007\)](#) have found a star (RP04 Star-E) which may contain blueshifted Fe I lines, indicating their association with the remnant. Unfortunately, the star has neither a significant peculiar radial velocity ([Ihara et al. 2007](#); RP04) nor a significant peculiar proper motion (RP04 and confirmed by our work; see Table 2.1).

High-resolution spectroscopy of each candidate in the remnant’s center is necessary to precisely determine each star’s physical parameters. However, the small observed velocities of the remaining stars suggest that the donor star would have needed to be a giant at the time of explosion. Using RP04’s observed values, none of the stars in the remnant’s center appear consistent with what is expected of a giant star as the donor star except possibly for Star-A. We also note that there is an additional star present in archived HST images, not cataloged in RP04, offset from RP04’s star A by 0.5'' E and 0.2'' N at  $m_V = 16.8$ ,  $(B-V) = 1.0$ . This star, near the remnant’s centre, has a color consistent with an F-star (assuming that it is behind the bulk of the line of sight reddening), but it will require adaptive optics to obtain its spectrum given its proximity to the 13th magnitude Star-A. This star could potentially be a non-giant progenitor.

If future observations are unable to pinpoint a viable donor star, other progenitor scenarios will have to be considered. These include the double degenerate scenario, or a scenario where there is a long time delay between the accretion phase of a donor star onto the white dwarf, and the ultimate supernova explosion.

We would like to thank the Subaru HDS team for taking these observations in service mode. This paper makes use of data obtained from the Isaac Newton Group Archive which is maintained as part of the CASU Astronomical Data Centre at the Institute of Astronomy, Cambridge. This publication makes use of data products from the Two Micron All Sky Survey, which is a joint project of the University of Massachusetts and the Infrared

Processing and Analysis Center/California Institute of Technology, funded by the National Aeronautics and Space Administration and the National Science Foundation. This work also makes use of POSS-I data. The National Geographic Society - Palomar Observatory Sky Atlas (POSS-I) was made by the California Institute of Technology with grants from the National Geographic Society. WEK, BPS and MA are supported by the Australian Research Council (grant numbers DP0559024, FF0561481). This paper was conceived as part of the Tokyo Think Tank collaboration, and was supported in part by the National Science Foundation under Grant No. PHY05-51164. This work was supported in part by World Premier International Research Center Initiative (WPI Program), MEXT, Japan, and by the Grant-in-Aid for Scientific Research of the Japan Society for the Promotion of Science (18104003, 18540231, 20540226) and MEXT (19047004, 20040004). Additionally we would like to thank Pilar Ruiz Lapuente and her team for the valuable discussions we had in regards to the manuscript. We would also like to thank our referee, who provided us with a very detailed and thorough analysis of the first manuscript and subsequent revisions.



# CHAPTER 3

---

## Tycho's Six: High-Resolution spectroscopy search for the remaining donor for the Tycho supernova

### 3.1. Introduction

Type Ia Supernovae (**SNe Ia**) are of great interest for astronomy. They represent some of the most extreme physical situations in stellar astronomy, produce substantive amounts of Iron group elements which impacts the chemical evolution of galaxies and the Universe, and are uniquely powerful probes of Cosmic distance. applications in stellar and galactic astronomy as well as in cosmology. Despite their wide ranging significance, fundamental uncertainties remain around progenitor of these cataclysmic events.

There is general consensus that **SNe Ia** are caused by the deflagration/detonation of a Carbon/Oxygen white dwarf which is accreting material from a binary companion. Scenarios exists where the explosion can be initiated from a detonation on the surface of the star (reference of Livne, and Sim), through runaway carbon burning in the white dwarfs interior, or through a cataclysmic merger of objects.

Observationally, two main scenarios for this accretion process can be identified.. The first scenario sees the accretion process occurring through Roche Lobe Overflow (henceforth RLOF) of a close non-degenerate companion (also known as donor star). This companion, which has undergone common envelope evolution with the white dwarf, can be a helium, main-sequence, sub-giant, or red giant star. is a main-sequence to red giant star at the time of the explosion (SD scenario). In all cases the donor star should survive the explosion and remains visible post-explosion.

The second scenario is the dynamical merger of two white dwarfs (DD scenario). In this scenario, the co-evolution of two stars eventually leads to a close binary of two white dwarfs, which are able, through the emission of gravitational radiation, to merge over a

wide range of times after the initial formation of the system. In most cases this would leave no remaining star (e.g. Pakmor et al., 2010).

Both scenarios have support in observation and theory. The detection of circum-stellar material around certain SN Ia, such as SN 2006X (Patat et al., 2007), provides support for the SD model. On the other hand the lack of substantial hydrogen in in the majority of other SNe Ia (Leonard, 2007) poses a challenge to the SD scenario.

Kasen (2010) suggests that the interaction with the non-degenerate companion should imprint an observable signature on a SN Ia light curve, depending on viewing angle, and radius of the companion. Such an excess has not yet been observed (Hayden et al., 2010; Tucker, 2011; Bianco et al., 2011).which is at odds with Red Giant companions forming the majority of SNe Ia.

Population synthesis calculations are challenging, with various authors getting different results for the same inputs (Nelemans paper). However there is a general trend from these calculations that neither single-degenerate nor double degenerate stars can provide enough systems to explain the SN Ia rate (Ruiter et al., 2009; Mennekens et al., 2010; Yu & Jeffery, 2010; Han, 2008). Several authors suggest the population might comprise both single and double degenerate systems.

The physics of white dwarf mergers is challenging to numerically simulate, but in the simplest calculations, these mergers will lead to the formation of a neutron star (Saio & Nomoto, 1985). Recently Pakmor et al. (2010) have shown that for certain parameters (white dwarf binaries with a mass ratio very close to one) the merger may explain sub-luminous supernovae.

To investigate the nature of progenitors observationally Ruiz-Lapuente et al. (2004, henceforth RP04) have tried to directly detect donor stars in SN Ia remnants within the Milky Way. They have identified two historical Galactic SN well suited to this task - SN 1006 and Tycho's SN (SNR1572 henceforth). Both remnants are young (440 and 1000 years old, respectively), almost certainly SN Ia from both their observational signatures (RP 04 but not RP04), Badenes et al. (look it up), and not overwhelmed by Galactic extinciton. In this paper, we will focus on SN1572.

SNR1572 is relatively close ( $2.8 \pm 0.8$  kpc), very young and has been confirmed as a normal SN Ia remnant (Badenes et al., 2006; Krause et al., 2008). While the star has an unusual spatial motion compared to other stars in the field, its current location and proper motion place it a significant distance from the remnants center - a feature difficult to explain in connecting Tycho-G to SNR1572.

RP04 investigated most bright stars in the central regions of SN1572 and found a star with an unusual spatial motion (Tycho-G by their nomenclature) and suggested this as a possible donor star for SN1572. One consequence of RLOF is a rotational velocity induced on the donor star by tidal locking in the system. This results in an unusually large rotationally velocity, related to the orbital velocity of the binary system and can be used to single out donor stars against nearby unrelated stars. (Kerzendorf et al., 2009, ,henceforth WEK09) investigated rotation for Tycho-G but found no excess rotation velocity compared to a normal star. WEK09's measurements of Tycho-G, including a revised radial velocity, compared to a Galactic models, showed it is statistically consistent with an interloping star.

However, WEK09 were able to provide an a priori unlikely scenario, where the star was able to lose its rotational signature.

Hernandez et al. (2009, henceforth GH09) analysed a spectrum of Tycho-G observed with the HIRES-instrument on the Keck telescope. GH09 confirmed WEK09's radial velocity for Tycho-G and determined its stellar parameters and metallicities. GH09 in addition to refining the metallicity, Temperature and Gravity measurements for Tycho-G, concluded concluded that Tycho-G has an unusually large amount of Ni. GH09 claim that this Ni measurement could be attributed to the accretion of ejecta material on the donor star.

In this paper we analyse HIRES spectra of the 6 bright stars in SNR1572 center. These spectra were taken by the same program that obtained the data used by GH-09, and we independently reanalyze this spectrum as part of our program.

We describe the observational data and our data reduction procedures in Section 3.2. Section 3.3 is divided into five subsections detailing the measurements of proper motion, radial velocity, rotation, stellar parameters and abundances. In Section 3.4 we analyse the measurements of each star to investigate its potential association with SNR1572, and present our conclusion in section 3.5.

## 3.2. Observations and Data Reduction

We obtained spectra with the High Resolution Echelle Spectrograph (HIRES Vogt et al., 1994) on the Keck 10m telescope in Mauna Kea. The observations were made on two nights on 2006 September 10 and 2006 October 11. The slits B5 and C1 (with the same width of 0.86'' but different lengths, B5 length 3.5'', C1 length 7.0'') were used resulting in a wavelength coverage of 3930 – 5330 Å, 5380 – 6920 Å and 6980 – 8560 Å with  $R \approx 50,000$ , providing us with the necessary spectral resolution and wavelength coverage to determine stellar parameters. The spectra were reduced using the MAKEE package. All spectra were corrected to heliocentric velocities, using the MAKEE skyline method. The spectra were not corrected for telluric lines as they will not influence our analysis of the stellar parameters. The final exposure times of the combined spectra for each candidate and signal to noise ratio at 4000-4100 Å are shown in Table 3.1. Finally we normalized the spectrum using the IRAF-Task continuum. We note that Tycho-C and Tycho-D were observed on the same slit (C1) with a separation of 2.1''.

**Table 3.1** Observations of Stars

Name designation	RA (J2000) (hh:mm:ss.ss)	Dec (J2000) (dd:mm:ss.ss)	Date (dd/mm/yy)	Slit	$t_{\text{exp}}$ (s)	S/N
Tycho-A	00:25:19.73	+64:08:19.6	10/09/06	B5	900	$\approx 65$
Tycho-B	00:25:19.95	+64:08:17.11	10/09/06	B5	1200	$\approx 50$
Tycho-C	00:25:20.40	+64:08:12.32	11/10/06	C1	10800	$\approx 10$
Tycho-D	00:25:20.60	+64:08:10.82	11/10/06	C1	10800	$\approx 5$
Tycho-E	00:25:18.29	+64:08:16.12	11/10/06	C1	9000	$\approx 15$
Tycho-G	00:25:23.58	+64:08:02.06	10/09/06 & 11/10/06	B5&C1	24000	$\approx 30$

In addition, we obtained low-resolution spectroscopy ( $R \approx 1200$ ) of Tycho-B with the dual-arm Low-Resolution Imaging Spectrometer (LRIS; [Oke et al., 1995](#)) mounted on the 10-m Keck I telescope. The observations were taken on one run on 2010 November 07, using only the blue arm with the 600/4000 grism and the 1'' wide slit. This resulted in a wavelength coverage of 3200 – 5600 Å. These observations were taken to obtain a precise measurement of the surface gravity for Tycho-B using the size of the Balmer decrement. The spectrum of Tycho-B was reduced using standard techniques (e.g. [Foley et al., 2003](#)). Routine CCD processing and spectrum extraction were completed with IRAF<sup>1</sup>, and the data were extracted with the optimal algorithm of [Horne \(1986\)](#). We obtained the wavelength scale from low-order polynomial fits to calibration-lamp spectra. Small wavelength shifts were then applied to the data after measuring the offset by cross-correlating a template sky to the night-sky lines that were extracted with the star. Using our own IDL routines, we fit a spectrophotometric standard-star spectrum to the data in order to flux calibrate Tycho-B and remove telluric lines ([Horne, 1986](#); [Matheson et al., 2000](#)).

### 3.3. Analysis

#### 3.3.1. Astrometry

Proper motions can be used to identify potential donor stars because donor stars freely travel with their orbital velocity after the SN explosion disrupts the system. RP04 suggested Tycho-G as a possible donor due to its unusually high proper motion and unusually high radial velocity. For this work we measured proper motions for 201 stars within one arcminute of the remnant's center. We used archival HST images for three different epochs (HST Program ID 9729 & 10098; November 2003, August 2004, May 2005) each consisting of three exposures (1 s, 30 s and 1440 s) in the F555W using the Advance Camera for Surveys (ACS). The pixel size in each exposure is 50 mas pixel<sup>-1</sup>. This dataset results in a maximum baseline of 30 months.

We used an image from the middle epoch (2004) to establish a reference frame and oriented the pixel coordinate system with the equatorial system. We then applied a distortion correction for the F555W filter ([Anderson & King, 2006](#)) to each images and then calculated transformations (order xxxx) between all other images and the reference image. We then used these transformations to calculate the position of all stars in the reference coordinate system with the overall uncertainty of each position estimated (How?). Some faint stars where not detected in the shorter exposures and were thus excluded from proper motion measurements (with 114 Stars remaining).

For each star, we fit a linear regression for the stellar positions over time in the pixel coordinates (which were aligned with the equatorial system). The x and y data were treated as independent measurements, with separate regressions solved for each axis directions. Errors were estimate using standard least squares analysis and the individual error estimates each object's positions.

---

<sup>1</sup>IRAF: the Image Reduction and Analysis Facility is distributed by the National Optical Astronomy Observatory, which is operated by the Association of Universities for Research in Astronomy (AURA) under cooperative agreement with the National Science Foundation (NSF).

**Table 3.2** Proper motion of Candidates

Name designation	RA (J2000) (hh:mm:ss.ss)	Dec (J2000) (dd:mm:ss.s)	$\mu_\alpha$ mas yr $^{-1}$	$\mu_\delta$ mas yr $^{-1}$	$\Delta\mu_\alpha$ mas yr $^{-1}$	$\Delta\mu_\delta$ mas yr $^{-1}''$	$r$
B	0:25:19.97	64:08:17.1	-1.24	0.56	0.62	0.64	4.86
A	0:25:19.73	64:08:19.8	-0.09	-0.89	1.17	0.90	6.21
A2	0:25:19.81	64:08:20.0	-0.71	-3.60	0.69	0.64	6.58
C	0:25:20.38	64:08:12.2	-0.21	-2.52	0.65	0.65	6.66
E	0:25:18.28	64:08:16.1	2.04	0.54	0.66	0.69	7.60
D	0:25:20.62	64:08:10.8	-1.12	-1.99	1.01	0.86	8.60
1	0:25:16.66	64:08:12.5	-2.27	-1.37	1.60	1.15	18.00
F	0:25:17.09	64:08:30.9	-4.41	0.20	0.70	0.71	22.69
J	0:25:15.08	64:08:05.9	-2.40	-0.25	0.62	0.62	29.44
G	0:25:23.58	64:08:01.9	-2.50	-4.22	0.60	0.60	29.87
R	0:25:15.51	64:08:35.4	0.28	0.24	0.89	0.80	33.23
N	0:25:14.73	64:08:28.1	1.18	0.89	0.86	0.98	33.66
U	0:25:19.24	64:07:37.9	0.01	-3.04	0.73	0.75	36.06
Q	0:25:14.81	64:08:34.2	1.45	3.07	0.64	0.72	36.19
T	0:25:14.58	64:07:55.0	-3.85	0.52	0.72	0.62	36.78
K	0:25:23.89	64:08:39.3	0.18	0.17	0.73	0.69	38.73
L	0:25:24.30	64:08:40.5	0.16	-0.44	0.75	0.82	41.59
S	0:25:13.78	64:08:34.4	4.16	0.58	0.83	0.84	42.09
2	0:25:22.44	64:07:32.4	74.85	-4.43	0.82	0.83	46.09

There are three measurements of the geometric center of SN1572 using different data-sets. [Reynoso et al. \(1997\)](#) using VLA data determined the center to R.A. 00:25:14.95 Dec +64:08:05.7 J2000, [Hughes \(2000\)](#) using ROSAT data got R.A. 00:25:19 Dec +64:08:10 J2000 and [Warren et al. \(2005\)](#) with Chandra data determined the center to R.A. 00:25:19.40 Dec +64:08:13.98 J2000.

Table 3.2 lists the proper motions and errors of all stars mentioned in RP04 (19 stars) which were analyzed in this work as well as the distance to the geometric X-Ray center measured by Chandra.

We compared the distribution of proper motions of all measured stars to ours candidates in Figure 3.1.

### 3.3.2. Radial Velocity

The radial velocity of each star was measured using the IRAF task *fxcor* ([Tonry & Davis, 1979](#)). MAKEE was used to calculate an intrinsic velocity shift by comparing offsets of the nightsky-lines. The radial velocity standards were reduced in the same fashion.

Each order of each star was then cross-correlated with at least two other radial velocity standards (HR6349, HR6970, HR1283) which had been observed on the same night.

The radial velocity for Tycho-B was measured in the course of determining the stellar

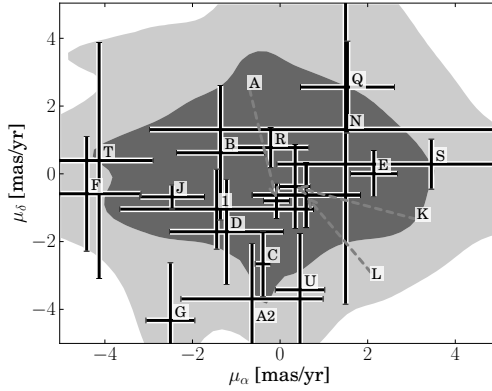


**Figure 3.1** The contours show the distribution of proper motion ( $1 - \sigma$  and  $2 - \sigma$ ) excluding the named stars. We show the location of the candidate stars and their errors on top of this distribution. Tycho-2 was not shown in this figure as it is an extreme outlier with  $\mu_\alpha = 75 \text{ mas yr}^{-1}$  and  $\mu_\delta = -4.4 \text{ mas yr}^{-1}$  but also at a large distance to the center of the remnant's geometric center (46'').

**Table 3.3** Radial velocities

Name designation	Date (dd/mm/yy)	$v_{\text{helio}}$ (km s $^{-1}$ )	$v_{\text{LSR}}$ (km s $^{-1}$ )	$\Delta v$ (km s $^{-1}$ )
Tycho-A	09/09/06	-36.79	-28.5	0.23
Tycho-B	09/09/06	-55.0	-57.0	$\approx 2$
Tycho-C	11/10/06	-58.78	-50.49	0.75
Tycho-D	11/10/06	-58.93	-50.64	0.78
Tycho-E	11/10/06	-64.2	-55.91	0.27
Tycho-G	09/09/06	-87.12	-78.83	0.25
Tycho-G	11/10/06	-87.51	-79.22	0.78

parameters for Tycho-B with the stellar parameter fitting package *sfit* (Jeffery et al., 2001). The *sfit* result consistently gives  $v_{\text{helio}} = -55 \text{ km s}^{-1}$  for different stellar parameters with an error of  $\approx 2 \text{ km s}^{-1}$ .

In Table 3.3 we have listed all the radial velocities both in a heliocentric frame and a local-standard-of-rest (henceforth LSR) frame. We will be referring to the heliocentric measurements from here on. The listed error is the standard deviation of the radial velocity measurement of all orders added in quadrature to the error of the radial velocity standards.

In Figure 3.2 we have compared the radial velocity of our sample stars to radial velocities of stars in the direction of Tycho's SNR using the Besançon Model (Robin et al., 2003). The distance as well as the error in distance are taken from Section 3.3.5. The candidates radial velocities are all typical for their distance. Finally, we note the measurement of Tycho-G is consistent with WEK09 and GH09.

### 3.3.3. Rotational Velocity

We have measured rotational velocities of all stars except Tycho-B in the same fashion as described in WEK09. We selected several unblended and strong (but not saturated) FeI

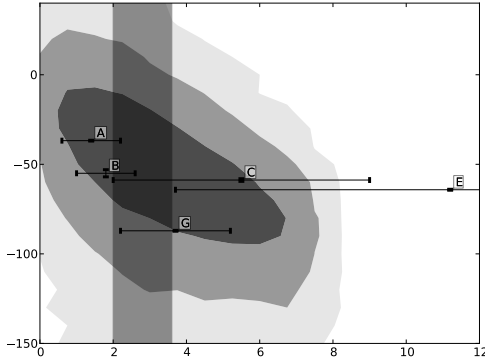


**Figure 3.2** The contours indicate 1, 2 and  $3 - \sigma$  levels of the distance and radial velocity using the Besançon Model (Robin et al., 2003) with  $\approx 60000$  stars in the direction of SNR1572 (only including star with a V between 10 and 20 as well as stars with a metallicity of  $[Fe/H] > -1$ ). We have overplotted our candidate stars with error bars. One should note that the errors in distance are only an indication of the error, the proper error surfaces can be seen in Figure 3.6. The vertical gray shade shows the error range for the distance of SNR1572.

lines in the stellar spectra . We added these lines after shifting them to the same wavelength and scaling them to the same equivalent width. This was done to improve the signal to noise ratio for the faint stars as well as providing consistency throughout all stars.

As a reference we created three synthetic spectra for each star (one broadened only with the instrumental profile, the others with the instrumental profile and  $v_{\text{rot}} \sin i$  of 10 and  $13 \text{ km s}^{-1}$  respectively) with the 2010 version of MOOG (Sneden, 1973), using our derived temperature, gravity and metallicity. As input data to MOOG we used the Castelli & Kurucz (2004) atmospheric models and a line list from Kurucz & Bell (1995). We then applied the same process of line selection and adding as for the lines in the observed spectra.

Figure 3.3 shows the comparison between the synthetic spectra of different rotational velocity and the observed spectra. This comparison indicates that the stellar broadening (rotational, macro turbulence, etc. ) is less than broadening due to the instrumental profile of  $6 \text{ km s}^{-1}$  for each star. We adopt  $6 \text{ km s}^{-1}$  as an upper limit to the rotation for all stars.

Due to its high temperature and rotation, we fit the rotational velocity for Tycho-B with the program *sfit* (Jeffery et al., 2001, described in section 3.3.4) as part of the overall fit for this star's stellar parameters. We find  $v_{\text{rot}} = 171^{+16}_{-33} \text{ km s}^{-1}$ . While Tycho-B's rotation is very high compared to the other candidate stars, for stars of this temperature and gravity a high rotation is not unusual.

In summary, none of the stars show rotation which is measurable at this resolution.

### 3.3.4. Stellar parameters

The stellar parameters are presented in Table ?? and were determined using a traditional spectroscopic approach based on the equivalent widths of lines of different excitation and ionization levels. . These measurements exclude Tycho-B, due to its hot temperature, and we measure its stellar parameters by direct comparison to models, in a separate procedure.

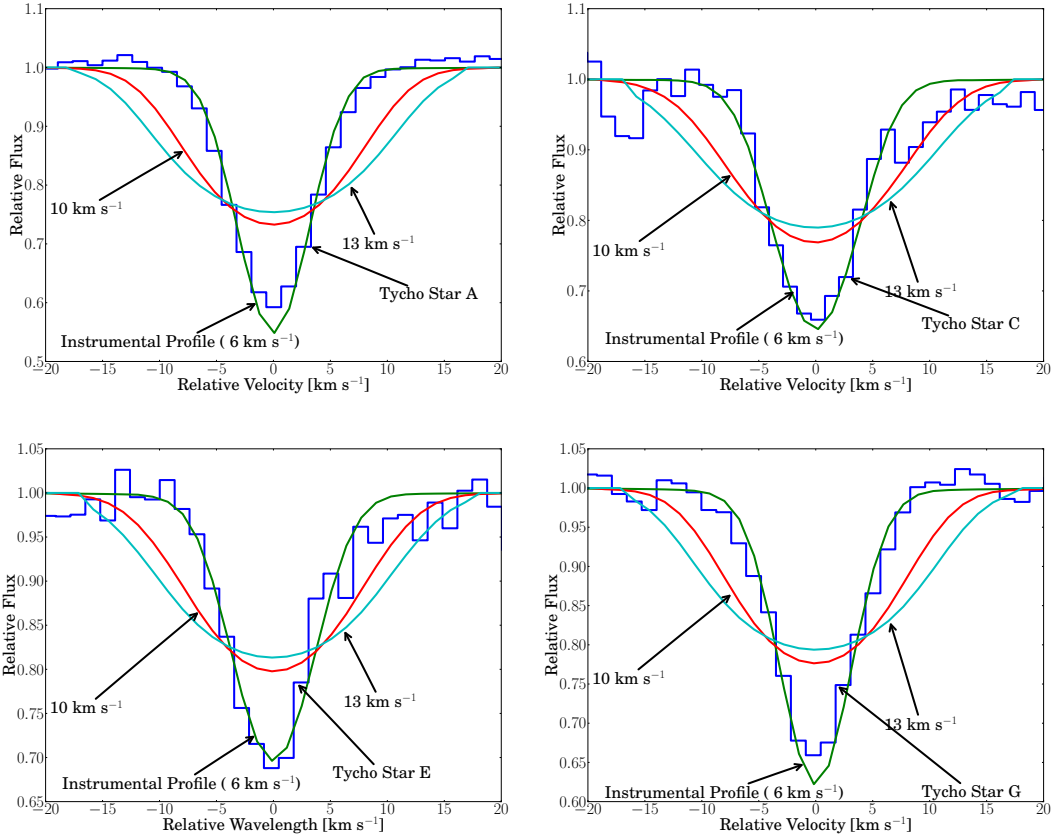


**Figure 3.3** The figures show the combination of Fe-line profiles after normalization to the same equivalent width and compare them to synthetic line profiles created by MOOG. We convolved the synthetic lines first with a rotational kernel with three different values for rotation and then with the instrumental profile. All stars show rotation less than  $6 \text{ km s}^{-1}$  which is equal to the instrumental profile at this resolution.

Equivalent widths (EWs) for a set of Fe lines were measured using routines in IRAF (compiled from Reddy et al. (2003, henceforth Reddy03) and Ramírez & Cohen (2002, henceforth RC02) Table ?? shows the EWs measured for each of the stars. Missing values indicate that the line was not detected.

We used the local thermodynamic equilibrium (LTE) stellar line analysis program MOOG (Sneden, 1973) and LTE model atmospheres from the Castelli & Kurucz (2003) grid to derive an abundance for a given line. The effective temperature,  $T_{\text{eff}}$ , was adjusted until the abundances from FeI lines displayed no trend as a function of excitation potential. The surface gravity,  $\log g$ , was adjusted until the abundances from FeI and FeII lines were in agreement. The microturbulent velocity,  $\xi_t$ , was adjusted until there was no trend between the abundances from the FeI lines and EW. This process was iterated until self consistent stellar parameters were obtained for each star. In our analysis, we explored stellar parameters at discrete values. For  $T_{\text{eff}}$ , we considered values at every 25 K (e.g., 4000, 4025 K, etc.), for  $\log g$ , we considered values at every 0.05 dex (e.g., 1.00, 1.05 dex, etc.), and for  $\xi_t$ , we considered values at every 0.05 km s<sup>-1</sup> (e.g., 1.70, 1.75 km s<sup>-1</sup>, etc.). We assumed that excitation equilibrium was satisfied when the slope between  $\log \epsilon(\text{FeI})$  and lower excitation potential ( $\chi$ ) was  $\leq 0.004$ . We assumed that ionization equilibrium was

**Table 3.4** Stellar Parameters

Name designation	$T_{\text{eff}}$ (K)	$\log g$ (dex)	[Fe/H] (dex)	$\Delta[\text{Fe}/\text{H}]$ (dex)	[Ni/H] (dex)	$\Delta[\text{Ni}/\text{H}]$ (dex)	[Li/H] (dex)
Tycho-A	4975	2.9	0.02	0.16	0.05	0.025	0.09
Tycho-C	4950	2.9	-0.57	0.23	-0.14	-0.17	0.11
Tycho-E	5825	3.4	-0.16	0.21	0.2	0.0	0.131
Tycho-G	6025	4	-0.15	0.18	0.14	0.08	0.11

achieved when  $|\log \epsilon(\text{FeI}) - \log \epsilon(\text{FeII})| \leq 0.02$  dex. The microturbulent velocity was set when the slope between  $\log \epsilon(\text{FeI})$  and reduced equivalent width ( $\log W/\lambda$ ) was  $\leq 0.004$ . In all cases we found appropriate solutions in which the trends between Fe I, Fe II, EW and excitation potentials were small. We estimate that the internal errors are typically  $T_{\text{eff}} \pm 100$  K,  $\log g \pm 0.3$  dex, and  $\xi_t \pm 0.3$  km s $^{-1}$ . For further details regarding the derivation of stellar parameters, see [Yong et al. \(2008\)](#).

The final iron measurements are the average of FeI and FeII assuming the solar abundances of [Asplund et al. \(2009\)](#). In addition, we measured abundance for the Elements Ni and Li via EW analysis. We could not see any unusual abundance pattern for any of the sample stars (see Figure 3.4; Tycho-B's abundances are not presented on the plot as they were measured in a different fashion).

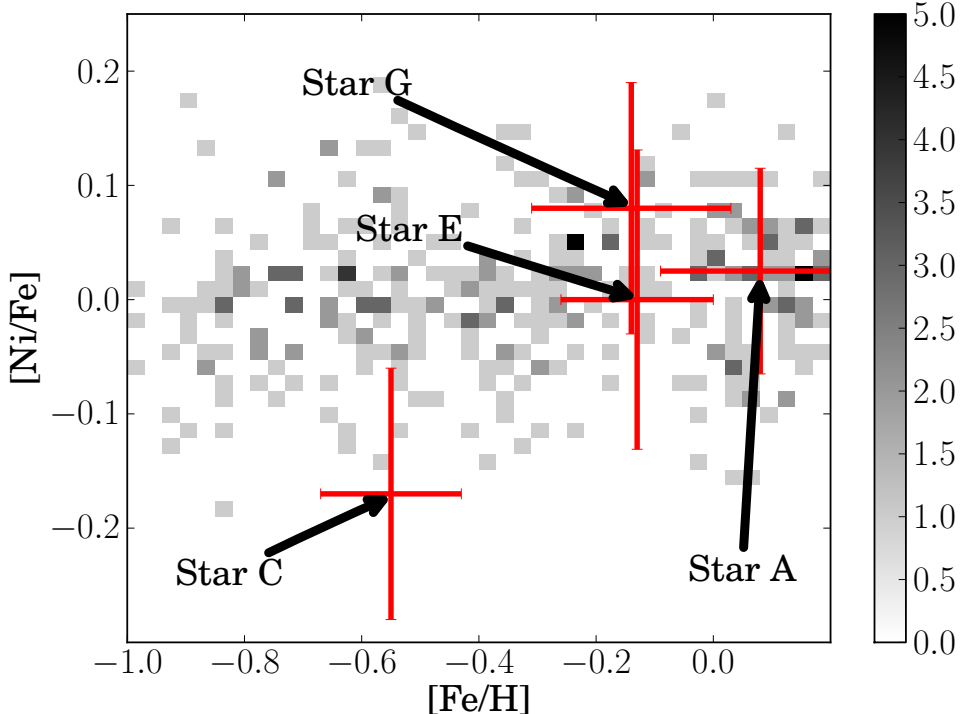


**Figure 3.4** The background colour indicates the distribution is taken from [Kobayashi et al. \(2006\)](#). All of the measured candidates are consistent within the errors with stars of the same metallicity.

In summary, the inferred metallicities for all candidates show that the candidates are of

**Table 3.5** Tycho-B abundances

Ion designation	$\lambda$ Å	$W_\lambda$ Å	$\epsilon$ dex	[X/H]	$\frac{\partial \epsilon}{\partial \log g}$	$\frac{\partial \epsilon}{\partial T_{\text{eff}}}$ K $^{-1}$
MgII	4481.13+4481.33	$220 \pm 15$	$6.18 \pm .08$	-1.40	0.08	$8 \times 10^{-5}$
SiII	6347.1	$140 \pm 5$	$6.96 \pm .18$	-0.59	-0.02	$1 \times 10^{-4}$
OI	7771.9+7774.2+7775.4	$460 \pm 30$	$8.43 \pm .10$	-0.58	0.24	$-4 \times 10^{-5}$

roughly solar metallicities with the exception of the metal-poor Tycho-C. The range of metallicities spanned by the program stars is compatible with membership of the thin disk (REFERENCE). Based on metallicity alone, we do not regard any of the program stars to be unusually metal-poor or metal-rich. Additionally, we find the [Ni/Fe] abundance to be consistent with stars of similar metallicity (see Figure 3.4). The stellar parameters and elemental abundances are listed in Table 3.4.

Because Tycho B has a temperature greater than 9000 K and is quickly rotating, the process described above cannot be used to measure stellar parameters. Instead we used the program *sfit* (Jeffery et al., 2001) to match the HIRES-spectrum to a grid of model spectra. To determine the stellar parameters for Tycho-B we have used a model grid with  $[\text{Fe}/\text{H}] = -1.0$ ,  $8000 < T_{\text{eff}} < 16000$ ,  $7 < \log g < 2$ . This low metallicity is suggested by a very weak Calcium K line and Mg II lines, but is hard to measure. We can not measure Helium directly in this spectrum and thus adopt  $N(\text{He}) = 0.1$  as this is empirically a very common Helium abundance in stars.

This analysis resulted in  $T_{\text{eff}} = 10000^{+400}_{-200}$  K,  $\log g = 3.67$  with slope  $\partial \log g / \partial T_{\text{eff}} = 0.27/500$  K $^{-1}$ , rotational velocity  $v \sin i = 171$  km s $^{-1}$  with slope  $\partial v \sin i / \partial T_{\text{eff}} = -41/500$  km s $^{-1}$  K $^{-1}$ . From qualitative analysis this object seems metal poor (e.g. in comparison to stars of similar stellar parameters but solar metallicity), but its high rotation and temperature make it hard to determine this parameter precisely. For the present, we assume  $[\text{Fe}/\text{H}] = -1.0$  unless otherwise noted.

In addition, using the high-resolution spectrum, we measured the equivalent widths of several lines predicted to be strong in the VALD database (Kupka et al., 2000). The abundances were deduced from the equivalent widths using a model atmosphere having  $T_{\text{eff}} = 10000$  K,  $\log g = 3.67$  and  $[\text{Fe}/\text{H}] = -1.0$  (see Table 3.5).

One caveat regarding these abundances is the use of equivalent widths from single lines with large rotational broadening, since the effect of blending with nearby weak lines cannot be taken into account. A second is that these abundances invariably rely on the strongest lines, which are precisely those most susceptible to departures from local thermodynamic equilibrium. Nevertheless, they do confirm the earlier impression that the star is metal-poor, and justify the adoption of  $[\text{Fe}/\text{H}] = -1.0 \pm 0.4$ .

As a second approach to determine the stellar parameters of Tycho-B we used the low resolution spectra observed with LRIS. The observation range of LRIS was chosen to be centered around the Balmer jump as this feature is sensitive to the surface gravity (Bessell, 2007). We fitted the spectra to a grid of model spectra (Munari et al., 2005) using a spectrum fitting tool described below. The final grid we used covered  $\log g$  from 3.5 to 4.5 in steps of 0.5 and  $T_{\text{eff}}$  from 9000 to 12000 K in steps of 500 K. In addition we expanded

the grid by reddening the spectra with the *pysynphot*-package<sup>2</sup>. We also added diffuse interstellar bands (Beals & Blanchet, 1937; Herbig, 1966, 1967, 1975, 1995; Hibbins et al., 1994; Jenniskens & Desert, 1994; Wilson, 1958) to the synthetic spectra , which were scaled with reddening . The included E(B-V) ranged from 0.5 to 1.3 in steps of 0.2. We assumed a rotation of 171 km s<sup>-1</sup> in the grid (see section 3.3.3).

We used  $\chi^2$  as a figure of merit in our fitting procedure. To find the best fit for Tycho-B we used the MIGRAD algorithm provided by *MINUIT* (James & Roos, 1975) and linearly interpolated between the grid points using *LinearNDInterpolator* provided by the *scipy*-package Jones et al. (2001). The fit of Tycho-B results in  $T_{\text{eff}}=10570$  K,  $\log g=4.05$ ,  $[\text{Fe}/\text{H}]=-1.1$  and  $E(\text{B}-\text{V})=0.85$ . The model fits the synthetic spectrum poorly in the wavelength region between 3800 – 4280 Å in (see Figure 3.5). The adopted mixing length parameter used in 1D model atmospheres used to construct the spectralgrid influences the fluxes in that region as well as affecting the hydrogen line profiles. Heiter et al. (2002) and others show that a mixing length of 0.5, rather than 1.25 as used in the Kurucz/Munari grid, better fits the violet fluxes and the hydrogen line profiles. Spectra using a mixing length parameter of 0.5 are brighter in the violet and the H <sub>$\gamma$</sub> , H <sub>$\delta$</sub>  and H <sub>$\beta$</sub>  profiles give the same  $T_{\text{eff}}$  as the H <sub>$\alpha$</sub>  profiles. We have chosen, however, to fit the spectrum and ignore the problematic spectral region (3800 – 4280 Å) to avoid a systematic error. This yields  $T_{\text{eff}}=10722$  K,  $\log g=4.13$ ,  $[\text{Fe}/\text{H}]=-1.1$  and  $E(\text{B}-\text{V})=0.86$ . The differences are indicative of a systematic error in the model. We adopt the fit excluding the problematic wavelength region in the further analysis. Exploring the complex search space we estimate the error to be  $\Delta T_{\text{eff}}=200$  K,  $\Delta \log g=0.3$  and  $\Delta [\text{Fe}/\text{H}]=0.5$ , but acknowledge that the parameters are correlated.

### 3.3.5. Distance

To measure the distance to the candidate stars we used colours and absolute magnitude from isochrones by Pietrinferni et al. (2004). We used the MIGRAD algorithm (James & Roos, 1975) to find close matches of the measured values to  $T_{\text{eff}}\text{-}\log g$  isochrones by varying the age of the isochrone. Subsequently we calculate E(B-V) using the isochrone's colour and we extract a mass from the isochrone. The results can be seen in Table 3.7. To estimate the errors in all distance, reddening and mass we employed the Monte-Carlo method with 10,000 samples of  $T_{\text{eff}}$ ,  $\log g$ ,  $[\text{Fe}/\text{H}]$ , B- and V-magnitude (see Figure 3.6). Errors included in Table 3.7 are the standard deviations of the Monte-Carlo sample. The data shows that all stars are compatible with the distance of the remnant. This is not unexpected as the uncertainties of the measurements in stellar parameters are relatively large.

---

<sup>2</sup>pysynphot is a product of the Space Telescope Science Institute, which is operated by AURA for NASA.

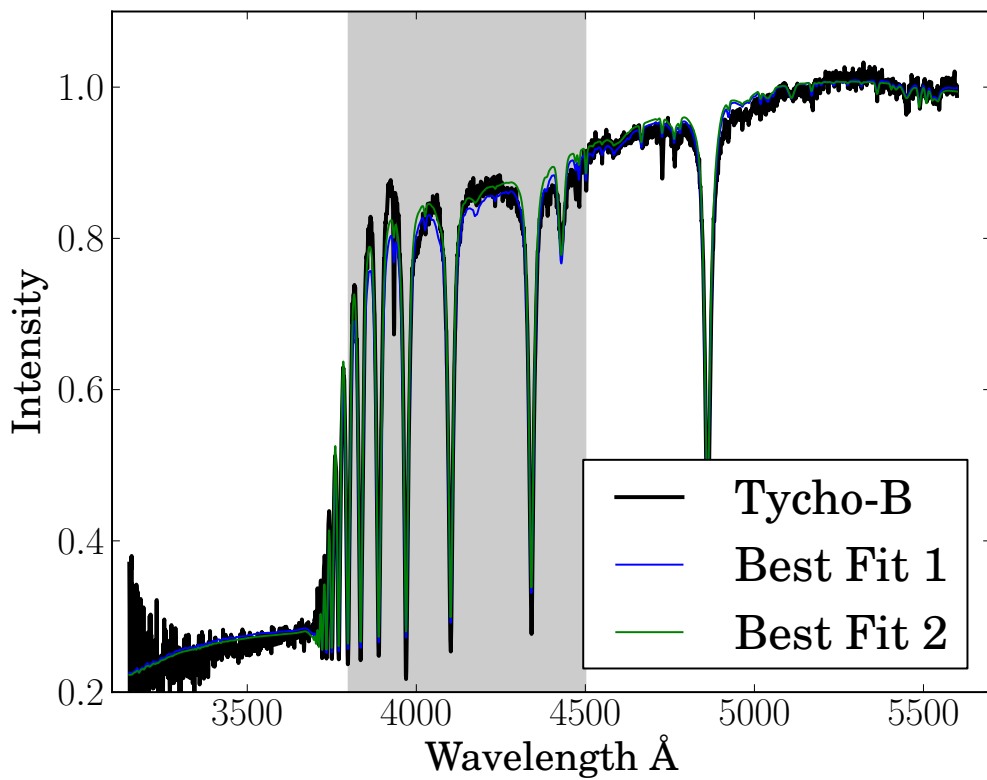


**Figure 3.5** The plot shows the normalized spectrum of Tycho-B with the fit which excluded the spectral region between  $3800 - 4500 \text{ \AA}$ (Best Fit 1) and the fit with the problematic region (Best Fit 2). The region is marked with a gray shade.

**Table 3.6** Distances, Ages and Masses of candidate stars

Name designation	Mass $M/M_{\odot}$	$\Delta M/M_{\odot}$	Age Gyr	$\Delta \text{Age}$ Gyr	Distance kpc	$\Delta \text{Distance}$ kpc
Tycho-A	2.4	0.8	0.7	2.3	1.4	0.8
Tycho-B	1.8	0.4	0.8	0.3	1.8	0.8
Tycho-C	0.9	0.4	10.0	3.4	5.5	3.5
Tycho-E	1.7	0.4	1.4	1.1	11.2	7.5
Tycho-G	1.1	0.2	5.7	2.1	3.7	1.5

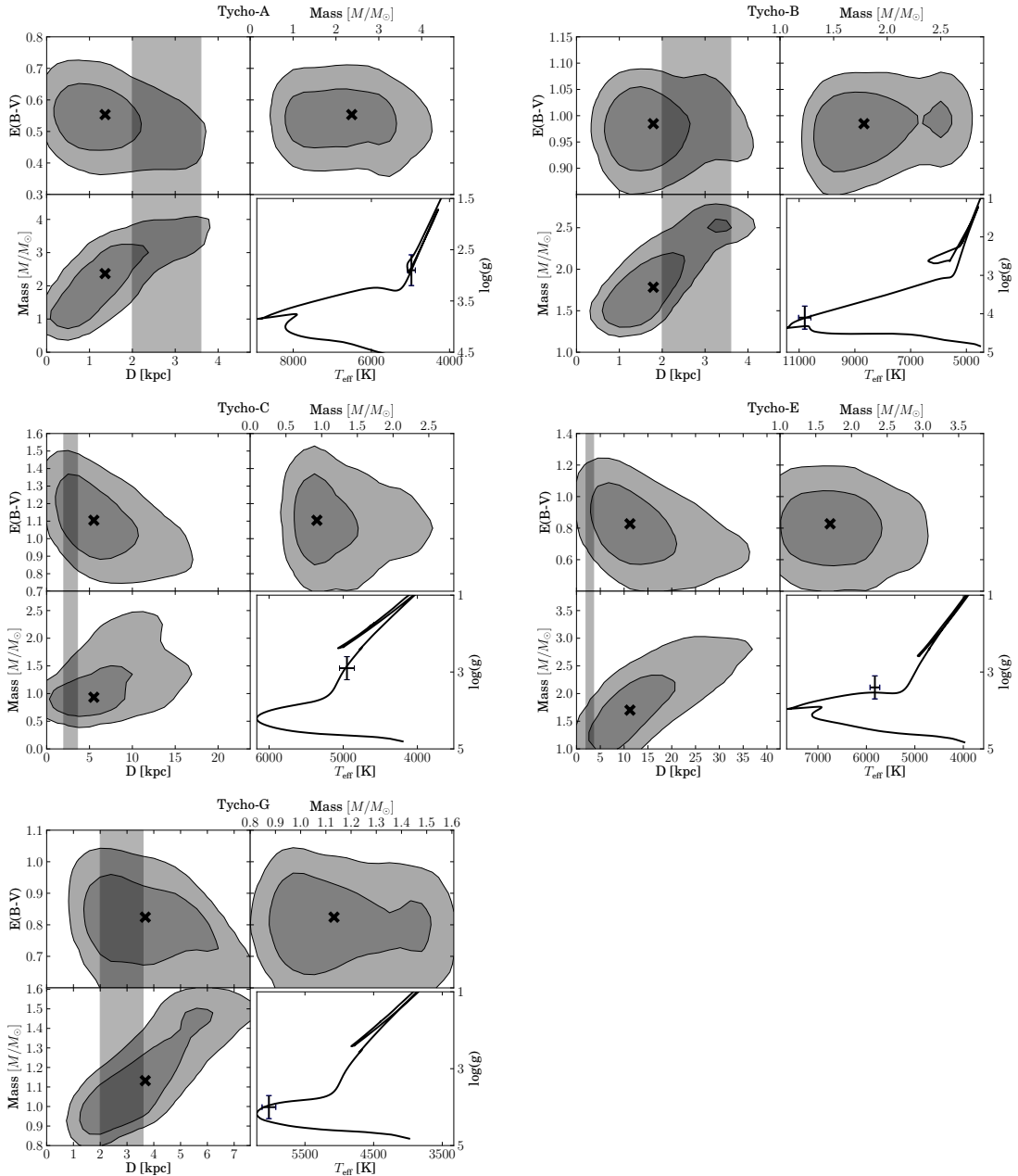


**Figure 3.6** The figures show error contours for distance, extinction and mass of the candidates. The lower right shows the optimal isochrone (Pietrinferni et al., 2004) for the measured values of  $T_{\text{eff}}$  and  $\log(g)$ .

### 3.4. Discussion

In our sample of six stars we find no star that can be unambiguously identified as a donor star for SN1572. On the other hand none of the stars in the sample can be completely ruled out.

Tycho-A is a metal rich giant. It seems to be likely that Tycho-A is a foreground star. Its principal redeeming feature as a donor star candidate is that it is located in the geometric center of the remnant, and that it has a relatively low gravity. Tycho-A shows a very low spatial motion which is consistent with a giant donor star scenario. Its lack of rotation, however, is in conflict with said scenario. Taking all measurements into account we regard Tycho-A to be a very weak candidate.

Tycho-B's high temperature, position at the center of the remnant, high rotational velocity and unusual chemical abundance made it a highly unusual candidate in the Tycho Remnant center. Despite the *a posteriori* unlikely discovery of such a star in the remnant center, Star B's high rotational velocity coupled with its low spatial velocity, seem to be in conflict with viable donor star scenario. These scenarios predict that the donor star will tidally couple to the white dwarf star before explosion, causing the rotation and spatial motion to be correlated post explosion (as discussed in WEK09). The large rotation seen in Tycho-B should accompanied by spatial motion, which is ruled out by the observations presented here, a problem we are unable to reconcile with Tycho-B being the donor star.

Tycho-C consists of two stars which are only resolved in HST images. It consists of a brighter bluer component and a dimmer redder component (difference of one magnitude in all colors) (RP04). In our analysis we find a satisfying solution for the spectrum and suspect that this is from the bluer brighter component. For the brighter bluer component Tycho-C is a metalpoor giant, probably located beyond the remnant. Tycho-C similar to Tycho-A might be compatible with a giant donor star scenario. It's lack of rotation and kinematics, however, make it an uninteresting candidate.

Tycho-D is roughly ten times dimmer than the close star Tycho-C ( $\approx 0.6''$ ). Our tools to measure stellar abundances are not effective for spectra with a S/N less than 10. We however compared the stars by over plotting them and determined that Tycho-D is similar to Tycho-C. Similar to Tycho-C we believe Tycho-D to be a very weak candidate.

Tycho-E is the most distant star in this set (11.2 kpc). It seems to be similar to Tycho-G in temperature, however is a subgiant. It is located 7'' from the geometric center and has no unusual stellar parameters or kinematics. [Ihara et al. \(2007\)](#) have looked at iron absorption lines in stellar spectra made by the remnant and found Tycho-E to be unusual. They suggest that a star in the background would show blue and redshifted iron lines, a star inside the remnant would only show blueshifted iron lines. A foreground star will not show any iron features from the remnant. [Ihara et al. \(2007\)](#) suggest that Tycho-E only shows blue-shifted lines and thus is suggested as being in the remnant. We believe however that Tycho-E is located far behind the remnant and suggest that a low column density on the receding side of the remnant could cause a lack of red-shifted iron features. In summary, a lack of rotation, kinematics and distance make it a very weak candidate.

Tycho-G is located 30'' from the X-Ray center which makes it the most remote object to the center in this work. This work confirms the radial velocity measured by GH09 and WEK09.

Figure 3.2 shows the expected distribution of radial velocities from the Bescançon model of Galactic dynamics. Tycho-G is not a significant outlier at the distance of the remnant as well as behind. In addition, this work has analysed the proper motion of stars around the center of SN1572. Figure 3.1 shows Tycho-G to be a slight outlier, but also shows other stars to be outliers. The kinematic features of a donor star might easily be lost in the kinematic noise of the Galaxy. WEK09, however, suggested using post-explosion stellar rotation as a possible feature for a donor star. This work suggests that Tycho-G has a rotation below the instrumental profile. We find Tycho-G to be a sub-giant star with roughly solar temperature and metallicity. GH09 measure a slight Ni enhancement, which they believe to originate in the contamination from the ejecta. Figure 3.4 compares our measurement of Tycho-G to the distribution of Ni and finds it to be consistent with this distribution. In addition, we could not measure a significantly enhanced Lithium-abundance as suggested in GH09. Finally, we have measured the distance to Tycho-G and believe it to be behind the remnant. Although our error bars make it consistent with the remnant.

In summary, we acknowledge that Tycho-G has unusual kinematics. However, this kinematic predicts rotation for Tycho-G which we do not observe (there are caveats however, see WEK09). We have not found a satisfying explanation for Tycho-G's large distance to the geometric center. We suggest that Tycho-G has the features consistent sub-giant background interloper.

### 3.5. Conclusion

This work did not detect an unambiguously identifiable donor star candidate. We acknowledge that Tycho-B and Tycho-G have unusual features, but there has been no conclusive explanation for all their parameters. Further theoretical predictions are needed to make a more precise distinction between donors and unrelated stars.

Our observations provide a case that the Tycho SNR does not have a MS, SG, or RG donor star, but other possibilities remain. These include a Helium donor, such as the so-called Sub-Chandra explosions discussed by [Livne & Arnett \(1995\)](#); [Sim et al. \(2010\)](#). These progenitor systems might leave behind a very faint and fast moving He star. Such a progenitor would probably evade detection, and would likely not leave behind traces, such as CSI with the remnant, or early light curve anomalies ([Kasen, 2010](#)). However, deep multi-epoch wide field optical images should catch any such star speeding away from the remnant center - these are observation not yet taken. Finally, a double degenerate progenitor, in most cases, does not leave behind a remant , and is consistent with finding no donor star in Tycho SNR.

SN 1006 and Kepler are two other [SN Ia](#) remnants in the Milky Way. SN 1006 is far from the plane and shows no signs of [CSI](#). Kepler SNR, while far from the galaxy plane, shows [CSI](#) with its remnant, and has all the indications of what might be expected from a Single Degenerate scenario of MS or lower gravity star ([Chiotellis et al., 2011](#)). Observations of these remnant will better establish if there is a continued pattern to the unusual stars in SN Ia remnant centers, or whether the lack of viable donor stars persists in multiple systems.

### **3.6. Acknowledgments**

PYRAF, scipy numpy matplotlib ipython suite, kudritzki, peter wood (for fxcor), Jorge, Onken with HIRES stuff, Amanda with differential rotation

### **3.7. Line list**

**Table 3.7** Measured equivalent widths from the Keck HIRES spectra

$\lambda$ (Å)	$\chi$ (eV)	$\log gf$ (dex)	Source	Tycho-A (dex)	Tycho-G (dex)	Tycho-C (dex)	Tycho-E (dex)
5082.35	3.658	-0.59	Reddy03	6.31	6.44		6.2
5088.54	3.85	-1.04	Reddy03	6.19	6.33		
5088.96	3.68	-1.24	Reddy03	6.21			
5094.42	3.83	-1.07	Reddy03	6.1			
5115.4	3.834	-0.28	Reddy03	6.22			
5682.20	4.10	-0.47	RC02	6.34			
5748.351	1.68	-3.26	RC02	6.33		5.74	
5749.297	3.94	-1.99	RC02	6.38			
5847.01	1.676	-3.41	Reddy03	6.26		5.55	
6007.31	1.68	-3.34	RC02	6.2		5.45	
6053.685	4.23	-1.07	RC02	6.33			
6086.28	4.26	-0.52	RC02	6.25	6.22		
6108.116	1.68	-2.44	RC02	6.26	6.11	5.33	
6111.08	4.088	-0.81	Reddy03	6.33		5.38	
6130.14	4.266	-0.94	Reddy03	6.31			
6175.37	4.089	-0.55	Reddy03	6.25	6.35	5.7	
6176.82	4.09	-0.26	Reddy03	6.3	6.27	5.43	6.01
6177.25	1.83	-3.51	Reddy03	6.23			
6186.71	4.10	-0.97	RC02	6.33	6.23		
6204.61	4.09	-1.11	Reddy03	6.32			
6322.17	4.15	-1.17	RC02	6.31			
6370.346	3.54	-1.94	RC02	6.37			
6378.26	4.154	-0.83	Reddy03	6.3		5.81	
6482.80	1.93	-2.63	RC02	6.2		5.38	
6598.60	4.23	-0.98	RC02	6.3		5.74	
6635.12	4.42	-0.83	RC02	6.37			
6643.64	1.68	-2.03	Reddy03	6.48	6.02	5.34	5.97
6767.772	1.83	-2.17	RC02	6.35	6.19	5.67	
6772.32	3.658	-0.97	Reddy03	6.31			
6842.037	3.66	-1.47	RC02	6.4	6.36		
7030.011	3.54	-1.73	RC02	6.42			
7122.197	3.54	0.048	RC02	6.33		5.34	
7261.918	1.95	-2.7	RC02		6.26		
7327.648	3.8	-1.77	RC02	6.38	6.44		
7409.35	3.8	-0.1	RC02			5.24	
7414.502	1.99	-2.57	RC02		6.2	5.57	6.03
7422.275	3.63	-0.129	RC02	6.47		5.32	5.84
7574.048	3.83	-0.58	RC02	6.3	5.97	5.12	
7748.89	3.7	-0.38	Reddy03	6.42	6.17	5.41	6.27
7788.93	1.95	-2.42	RC02			5.87	6.33
7797.59	3.9	-0.35	Reddy03	6.41	6.16	5.59	6.2
7917.44	3.74	-1.5	RC02		6.14		



# CHAPTER 4

---

## SN1006

### 4.1. Introduction

Schweizer & Middleditch (1980) identified an unusual O-Star (now called Schweizer-Middleditch Star, henceforth SM-Star) near the centre of SN1006. After successful identifications of neutron stars in both the Vela Remnant and the Crab Remnant this was thought to be the third identification of a stellar remnant in ancient supernovae. Subsequent UV spectroscopy follow-up of the SM-Star by Wu et al. (1983), showed strong FeII with a profile broadened by a few thousand km s<sup>-1</sup>. In addition, Wu et al. (1983) identified redshifted SiII, SiIII and SiIV lines. Their conclusion was that these absorption lines stem from an expanding iron core surrounded by a Silicon shell (similar what theoretical models suggest for a SNe Ia). This places the SM-Star behind the remnant and it is thought to be unrelated to SN1006.

SN 1006 is the closest of the young SN Ia remnants. Its distance has been determined to 2.2 kpc by using optical proper motion methods and radial velocity measurements from the remnant expansion (Winkler et al., 2003). The remnant of SN 1006 has been very well studied in many aspects. Absorption lines of the remnant plasma can be seen in background UV sources. This has enabled Winkler et al. (2005) to sketch the inner structure of the ejecta. A few tenth of a solar mass of iron suggests that this event was a SN Ia. The lack of a neutron star, similar to those found in SN II remnants, also suggests a thermonuclear event.

SN 1006 provides the perfect site for a donor star search. High extinction values that introduce additional challenges to stellar analysis (as seen in the SN 1572 remnant) are not present. The extinction, estimated for the background SM-Star, is relatively low at E(B-V) = 0.1 (Wu et al., 1993; Winkler et al., 2003). These serendipitous conditions for the SN 1006 remnant led us to launch a photometric and spectroscopic campaign to search for the donor star. The photometric observations were taken at Siding Spring Observatory with the 2.3m Telescope imager. The spectroscopic search area was determined by the center of the SNR1006 and a radius (see Figure 4.1). For the center we have opted to adapt a center determined by the mean of the X-ray and radio center presented in Winkler et al. (2003). As a radius we have opted to use 120'', which translates into 1200 km s<sup>-1</sup> at the distance

of SN 1006. We do believe that this generously chosen radius takes uncertainties of the center as well as the donor star scenarios into account. The spectroscopic observations were undertaken with the FLAMES multi-object spectrograph.

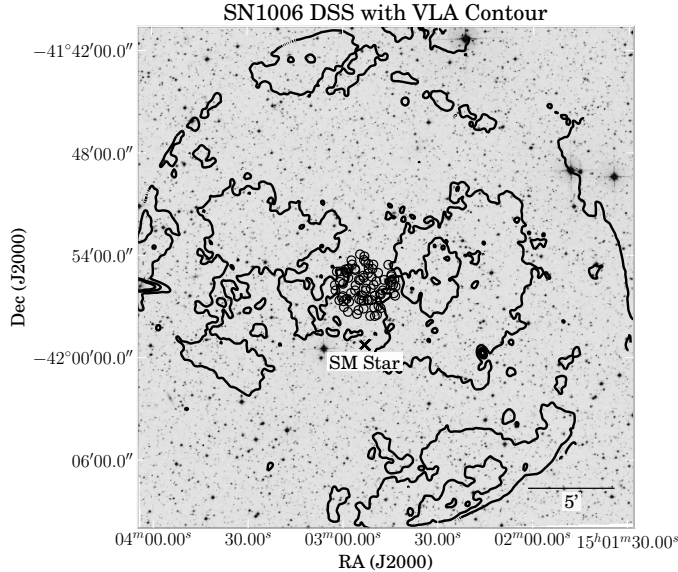


**Figure 4.1** example caption

We present photometry as well as high-resolution spectroscopy of the stars in SN1006 (for an overview see Figure 2.1. In Section ?? we outline the observations as well as data reduction of the photometric and spectroscopic data. Section 3.3 is split into five subsections. We first describe the photometric analysis and radial velocity measurements. The complete analysis of the data has not been done and we mainly present our technique. We conclude this chapter in Section 3.5 and discuss the possible implications of our initial find. In addition, we will describe future work including the final analysis of the data

## 4.2. Observations and Data Reduction

For our spectroscopic survey we selected 79 stars in a 120 "radius (this corresponds to  $780 \text{ km s}^{-1}$  at a distance of 2.2 kpc) around the centre of SN1006 ( $\alpha = 15^{\text{h}}02^{\text{m}}22\text{s}.1$ ;  $\delta = -42^{\circ}05'49''$ ). We observed targets to a maximum magnitude of R=18, this translates to a limiting luminosity of  $L = L_{\odot}$ . The surviving donor scenarios described in Marietta et al. (2000) and Pakmor et al. (2008) should be easily visible at that photometric depth. The VLT instrument FLAMES provides high resolution (R=25,000) and a large field of view (25') for a considerable number of stars per setup (130 targets). We chose the wavelength region from 5139 Å to 5356 Å which contains the gravity sensitive MgB Triplet as well as many Fe-Lines to accurately measure metallicity. Fibre buttons can be placed no less than 11" apart. Thus to observe all of the program stars in the crowded central field, we split the stars over three different setups. The first two setups were observed five times with 2775 s each. We deliberately chose bright stars for the last setup so that it only had to be observed three times with 2775 s each. As only the central 120" were crowded we placed spare fibres on

**Table 4.1** Flames Observations of SN1006 program stars

ObsID	MJD d	FWHM "	Airmass	Setup name	$v_{\text{helio}}$ correction $\text{km s}^{-1}$
360737	54965.1	1.2	1.2	SN1006 1	1.5
360739	54965.1	1.2	1.1	SN1006 1	1.5
360740	54965.1	1.0	1.1	SN1006 1	1.4
360741	54985.0	0.7	1.4	SN1006 1	-7.4
360742	54964.2	1.5	1.1	SN1006 1	1.7
360743	54985.0	0.8	1.2	SN1006 2	-7.5
360745	54985.0	0.9	1.1	SN1006 2	-7.6
360746	54985.1	1.0	1.1	SN1006 2	-7.7
360747	54985.1	1.0	1.1	SN1006 2	-7.7
360748	54985.2	0.9	1.1	SN1006 2	-7.8
360749	54963.1	1.2	1.2	SN1006 3	2.4
360751	54963.1	1.1	1.1	SN1006 3	2.3
360752	54963.2	1.1	1.1	SN1006 3	2.3

three bright stars ( $R \approx 10$ ; 2mass J15032744-4204463, J15031746-4204165, J15033195-4202356) located close to the edge of the 25' field for calibration purposes. Additional spare fibres were placed on sky positions. These were determined to be far from 2MASS sources and were subsequently manually inspected using DSS images (citedss).

We requested standard daytime calibration as well as simultaneous arc exposures with four fibres for each observation block. There are 13 observation blocks with an exposure time of 2775 s each. Table 4.1 provides the Observing ID, modified julian date, mean seeing, mean airmass, setup name and heliocentric correction for all observations. Due to broken fibres not all stars where observed for the expected length of time. SN1006-31 was not observed at all in this sample (see Figure ?? for the observation of the center of SN1006. This).

We applied a cosmic ray removal tool on the raw 2D frames (?). The data was then reduced with the ESO-CPL pipeline (version 5.2.0), using the GIRAFFE instrument recipes (version 2.8.9). The only change that was made to the default parameters was the usage of the Horne extraction algorithm instead of the "Optimal"-extraction algorithm. This yielded 366 individual spectra of the candidate stars and an additional 39 spectra of the Calibration stars. In addition, the Giraffe pipeline yields error frames which were used in the fitting process described in Section 4.3.5.

Our photometry was deduced from images taken with the image at the 2.3m Telescope at the Siding Spring Observatory. All data was taken on the night of the 11th of May. We exposed for 1860 s in U-Band, 1490 s in B-Band, 788s in V-Band and 1860 s in I-Band. For calibration purposes we took images of the PG1633 and PG1047 standard star regions in the same filters. The seeing ranged between 1 and 2 ". The data was reduced in the standard way using PyRAF<sup>1</sup>. Finally an astrometric solution was fitted using astrometry

<sup>1</sup>PyRAF is a product of the Space Telescope Science Institute, which is operated by AURA for NASA.

from the 2MASS point source catalogue (Skrutskie et al., 2006).

### 4.3. Analysis

A uniform analysis of this set of data is technically challenging due to the large variation in spectral quality (see Figure ??). We have explored multiple channels and believe that, although challenging, it is possible. We measure the radial velocity using the standard technique of cross-correlation (Tonry & Davis, 1979). It is crucial in our set to measure rotation, as this is one of key features of potential donor stars. In addition, a giant star with high rotation can be incorrectly identified as a main-sequence star without rotation. We are currently trialling multiple techniques for measuring stellar rotation. For identifying the fundamental stellar parameters we use a standard grid based approach. In the next sections we will give a detailed description of the methods used, but do caution the reader that this is work in progress and subject to change for the final publication.

#### 4.3.1. Photometry

We used SExtractor (?) to measure the magnitudes of the objects in the frames. We used the Stetson magnitudes<sup>2</sup> of our standard fields PG1633 and PG1047 to calibrate our magnitudes to a standard Bessel Filter system.

The measured magnitudes were supplemented with near infrared magnitudes from the 2MASS point source catalogue. To check the photometric measurements we plotted the obtained B-V colours against the V-K colours and compared this to theoretical colours from (?) in Figure ???. SN1006-100660 presents a strong outlier in this case. Inspecting ours as well as 2MASS imagery we believe there to be a second source which would explain this behaviour.

To compute temperatures from photometric colours we used the polynomials given in (?) and assumed an [Fe/H] of 0 for all stars in the first instance. The temperature polynomial coefficients incorporating the metallicity are particularly small for the V-J colour. If V-K was not available (as 2MASS did only provide upper limits for some of our program stars) we tried to use V-J colours. The calculated temperatures were only used as a first reference and we are trying to use the spectral information in our final temperature measurement.

Table 4.2 provides an overview of the photometry. We have also included  $\theta$  a angular distance of the star to the adopted center.

#### 4.3.2. Proper motion

Do we have proper motions? We claimed to have some to an accuracy of 10 mas/yr in our ESO proposal. I will leave this section out I think.

---

<sup>2</sup>This research used the facilities of the Canadian Astronomy Data Centre operated by the National Research Council of Canada with the support of the Canadian Space Agency

**Table 4.2** SN1006 photometry

Name	RA hh:mm:ss	Dec dd:mm:ss	$\theta$ "	U mag	$\sigma_U$ mag	B mag	$\sigma_B$ mag	V mag	$\sigma_V$ mag	I mag	$\sigma_I$ mag
SN1006 01	15:02:58.27	-41:55:20.9	67.8	16.03	0.02	14.76	0.00	13.50	0.08	12.30	0.18
SN1006 02	15:02:59.95	-41:56:25.2	86.1	18.84	0.08	16.96	0.01	15.37	0.01	13.95	0.05
SN1006 03	15:02:51.80	-41:56:39.9	49.8	16.16	0.02	15.86	0.01	15.04	0.01	14.23	0.09
SN1006 04	15:02:53.35	-41:54:18.0	93.6	16.67	0.02	16.33	0.00	15.47	0.00	14.62	0.00
SN1006 05	15:02:49.97	-41:56:23.9	45.7	16.90	0.03	16.41	0.00	15.50	0.01	14.65	0.00
SN1006 06	15:02:45.68	-41:54:35.2	110.5	16.21	0.01	16.17	0.01	15.50	0.00	14.78	0.01
SN1006 07	15:02:51.19	-41:55:58.5	19.8	17.62	0.05	16.91	0.02	15.90	0.01	14.92	0.02
SN1006 08	15:02:47.00	-41:55:28.3	69.3	16.57	0.03	16.53	0.01	15.86	0.01	15.16	0.00
SN1006 09	15:02:55.07	-41:57:14.4	86.6	18.46	0.20	17.73	0.01	16.58	0.01	15.53	0.02
SN1006 10	15:03:01.87	-41:54:59.2	113.4	17.18	0.04	17.06	0.00	16.30	0.00	15.51	0.00
SN1006 11	15:02:56.05	-41:54:53.5	68.1	17.02	0.03	17.12	0.00	16.33	0.05	15.61	0.01
SN1006 12	15:02:58.83	-41:56:35.5	80.0	17.60	0.03	17.22	0.00	16.39	0.02	15.50	0.02
SN1006 13	15:02:49.22	-41:57:31.1	107.6	17.93	0.09	17.41	0.01	16.49	0.00	15.74	0.06
SN1006 14	15:02:59.24	-41:54:51.6	93.1	17.93	0.04	17.44	0.00	16.56	0.00	15.75	0.01
SN1006 15	15:03:00.33	-41:56:29.8	91.9	17.81	0.01	17.42	0.01	16.63	0.01	15.87	0.04
SN1006 16	15:02:58.09	-41:54:47.9	86.4	19.60	0.47	18.37	0.01	17.26	0.00	16.11	0.03
SN1006 17	15:03:02.49	-41:55:46.7	107.7	17.45	0.02	17.40	0.00	16.66	0.04	16.02	0.13
SN1006 18	15:02:50.99	-41:56:39.4	52.2	18.00	0.03	17.61	0.00	16.77	0.03	15.87	0.04
SN1006 19	15:02:50.12	-41:57:05.5	80.1	20.28	0.00	18.75	0.01	17.39	0.01	16.01	0.00
SN1006 20	15:02:48.03	-41:56:19.4	60.6	-	-	19.59	0.03	18.04	0.01	15.97	0.17
SN1006 21	15:02:58.44	-41:54:50.1	87.5	20.60	0.00	18.47	0.01	17.36	0.01	16.30	0.03
SN1006 22	15:02:59.95	-41:55:41.9	79.8	17.26	0.04	17.25	0.00	16.71	0.06	16.18	0.04
SN1006 23	15:02:43.94	-41:56:15.4	102.3	19.62	0.32	18.50	0.01	17.39	0.00	16.24	0.01
SN1006 24	15:02:56.14	-41:54:49.2	72.3	-	-	18.28	0.00	17.59	0.13	16.49	0.11
SN1006 25	15:02:59.79	-41:56:43.2	93.1	17.75	0.01	17.64	0.06	17.03	0.02	16.35	0.03
SN1006 26	15:02:54.92	-41:55:27.7	33.1	18.10	0.10	17.95	0.01	17.23	0.02	16.43	0.00
SN1006 27	15:02:52.72	-41:55:58.9	7.6	18.61	0.08	18.26	0.02	17.47	0.03	16.64	0.05
SN1006 28	15:02:54.86	-41:56:36.4	50.2	18.52	0.13	18.24	0.00	17.43	0.02	16.70	0.02
SN1006 29	15:02:51.84	-41:54:47.9	64.5	-	-	19.23	0.00	18.00	0.02	16.72	0.04
SN1006 30	15:02:44.71	-41:55:15.4	97.7	18.05	0.03	18.24	0.03	17.54	0.02	16.75	0.01
SN1006 32	15:02:53.61	-41:55:13.7	38.7	18.72	0.18	18.42	0.02	17.64	0.03	16.78	0.03
SN1006 33	15:02:43.38	-41:55:51.5	105.7	19.07	0.23	18.56	0.04	17.66	0.04	16.69	0.05
SN1006 34	15:02:56.13	-41:56:05.1	39.1	18.64	0.11	18.52	0.02	17.76	0.01	16.94	0.01
SN1006 35	15:02:44.66	-41:55:10.0	100.4	19.06	0.17	18.74	0.00	17.84	0.02	16.88	0.05
SN1006 36	15:02:58.70	-41:55:02.9	81.4	19.46	0.40	18.65	0.01	17.79	0.01	16.86	0.02
SN1006 37	15:02:58.96	-41:55:02.5	83.9	-	-	-	-	-	-	-	-
SN1006 38	15:02:50.29	-41:55:45.6	29.2	18.58	0.08	18.48	0.03	17.80	0.03	17.00	0.01
SN1006 39	15:02:43.76	-41:55:25.6	104.7	18.86	0.06	18.44	0.02	17.69	0.01	16.97	0.01
SN1006 40	15:02:52.23	-41:56:37.9	47.0	-	-	-	-	-	-	16.28	0.06
SN1006 41	15:02:52.06	-41:55:05.2	47.1	17.97	0.01	18.02	0.00	17.61	0.01	17.11	0.02
SN1006 42	15:02:57.08	-41:54:34.3	90.4	19.22	0.27	18.78	0.03	17.99	0.01	17.16	0.03
SN1006 43	15:02:48.27	-41:56:15.9	56.7	-	-	20.14	0.04	18.76	0.08	17.25	0.06
SN1006 44	15:02:51.96	-41:54:31.4	80.7	-	-	19.79	0.01	18.54	0.02	17.06	0.01
SN1006 45	15:02:47.43	-41:56:05.3	62.0	18.45	0.11	18.43	0.02	17.71	0.03	17.00	0.05
SN1006 46	15:02:49.93	-41:57:35.3	108.8	20.09	0.17	19.04	0.03	18.05	0.04	17.19	0.20
SN1006 47	15:02:52.86	-41:54:25.7	85.7	18.89	0.24	18.63	0.01	17.96	0.03	17.14	0.03
SN1006 48	15:02:54.52	-41:55:29.9	28.5	-	-	19.29	0.03	18.38	0.01	17.38	0.06
SN1006 49	15:02:52.83	-41:56:06.1	14.7	18.90	0.33	18.84	0.00	18.17	0.01	17.37	0.05
SN1006 50	15:02:53.93	-41:56:22.6	33.4	19.68	0.11	18.99	0.03	18.07	0.03	17.19	0.02
SN1006 51	15:02:54.58	-41:53:58.4	114.7	19.47	0.00	18.90	0.26	17.99	0.19	16.93	0.17
SN1006 52	15:03:00.97	-41:54:58.6	104.9	19.41	0.17	18.89	0.00	18.08	0.03	17.24	0.02
SN1006 53	15:02:57.45	-41:56:14.7	56.4	19.32	0.43	18.90	0.03	18.13	0.01	17.24	0.05
SN1006 54	15:02:48.09	-41:57:07.7	92.9	20.33	0.58	19.40	0.02	18.45	0.01	17.48	0.03
SN1006 55	15:02:44.67	-41:55:35.9	92.6	-	-	19.90	0.01	18.68	0.03	17.36	0.04
SN1006 56	15:02:50.38	-41:54:34.5	81.7	-	-	20.15	0.16	18.83	0.06	17.46	0.08
SN1006 57	15:02:54.15	-41:56:40.9	51.5	19.59	0.57	18.91	0.02	18.26	0.04	17.63	0.07
SN1006 58	15:02:49.42	-41:55:33.5	42.3	18.90	0.09	18.92	0.02	18.21	0.02	17.41	0.02
SN1006 59	15:02:51.38	-41:57:34.9	104.7	19.59	0.37	19.21	0.01	18.54	0.02	17.78	0.02
SN1006 60	15:02:59.64	-41:57:03.8	104.8	20.05	0.18	19.22	0.01	18.48	0.13	18.62	0.43

**Table 4.2** SN1006 photometry (continued)

Name	RA hh:mm:ss	Dec dd:mm:ss	$\theta$ "	U mag	$\sigma_U$ mag	B mag	$\sigma_B$ mag	V mag	$\sigma_V$ mag	I mag	$\sigma_I$ mag
SN1006 61	15:02:53.45	-41:57:09.2	78.0	-	-	20.49	0.05	19.24	0.02	17.82	0.07
SN1006 62	15:02:44.94	-41:55:48.3	88.3	-	-	19.38	0.02	18.53	0.01	17.54	0.01
SN1006 63	15:02:50.89	-41:55:17.4	40.5	20.19	0.15	19.41	0.00	18.55	0.02	17.62	0.05
SN1006 64	15:02:55.53	-41:57:28.3	101.4	19.45	0.28	18.87	0.02	18.51	0.03	17.87	0.08
SN1006 65	15:02:44.57	-41:55:28.2	95.3	18.79	0.04	18.93	0.03	18.38	0.04	17.63	0.05
SN1006 66	15:02:57.28	-41:54:19.6	104.3	-	-	20.02	0.03	19.09	0.02	18.00	0.03
SN1006 67	15:02:48.88	-41:55:03.4	65.4	19.69	0.38	19.11	0.03	18.37	0.01	17.57	0.01
SN1006 68	15:02:43.51	-41:56:23.9	109.2	20.65	0.00	19.60	0.04	18.75	0.04	17.94	0.01
SN1006 69	15:03:01.11	-41:56:40.2	104.3	20.07	0.00	19.59	0.03	18.59	0.17	17.91	0.09
SN1006 70	15:02:58.01	-41:56:45.0	78.6	20.38	0.57	19.49	0.01	18.73	0.03	18.00	0.06
SN1006 71	15:03:00.93	-41:55:35.3	91.6	-	-	19.95	0.02	18.84	0.02	17.92	0.25
SN1006 72	15:02:58.39	-41:57:20.6	108.5	19.34	0.00	19.90	0.11	18.85	0.11	18.01	0.14
SN1006 73	15:02:50.64	-41:54:49.5	66.7	-	-	20.00	0.04	19.04	0.06	17.92	0.12
SN1006 74	15:03:02.32	-41:56:05.2	106.6	-	-	19.88	0.08	18.76	0.16	18.21	0.02
SN1006 75	15:02:53.19	-41:54:05.5	106.0	19.23	0.11	19.07	0.03	18.34	0.03	17.50	0.03
SN1006 76	15:02:44.17	-41:55:45.8	97.0	19.56	0.09	19.40	0.02	18.70	0.03	17.91	0.08
SN1006 77	15:02:55.98	-41:55:47.4	35.2	19.58	0.20	19.22	0.02	18.56	0.05	17.69	0.02
SN1006 78	15:02:48.76	-41:56:59.9	82.3	-	-	20.87	0.10	19.53	0.01	18.06	0.05
SN1006 79	15:02:53.45	-41:56:41.7	50.7	-	-	21.53	0.06	19.90	0.02	18.04	0.05

### 4.3.3. Radial Velocity

To obtain radial velocities we employ a two step process. We first used a solar spectrum from (?) with the standard cross-correlation technique described in (Tonry & Davis, 1979) and implemented in the IRAF-task *fxcor*. The cross-correlation was performed on every single spectra. The results were then heliocentrically corrected, then averaged for each star with a sigma clipping algorithm. We note that especially for faint objects we observe a second cross-correlation peak at  $0 \text{ km s}^{-1}$  and believe that this is reflected light from the moon. We believe that this has a negligible effect on our cross-correlation and the measurement of stellar parameters. This is the current progress for radial velocity measurements. As a future step we will remeasure the radial velocity with a matching template spectrum, although we do believe that this won't change the current results significantly.

In Figure 4.2 we have compared our radial velocity measurements with the Besançon kinematic model of the Milky way (Robin et al., 2003). The selection criteria for creating the Besançon kinematic model was all stars a circle around SN 1006 with an area 1 square degree and a magnitude cut of  $V > 10$ . We compared the resulting 16400 stars to our 78 stars in the sample.

### 4.3.4. Rotational Velocity

There is a large velocity spread in the direction of SN 1006 (see Figure 4.2). This makes it hard to isolate a donor star just on kinematic features. A distinguishing feature for a donor star might be rotation (discussed in Chapter ??). The rotational velocities in Chapters ?? and 3 were all measured manually. We selected weak iron lines and stacked them to obtain a line profile, which was compared to synthetically rotationally broadened lines. This was a feasible way for six spectra, it is however not feasible for more than 300 spectra.

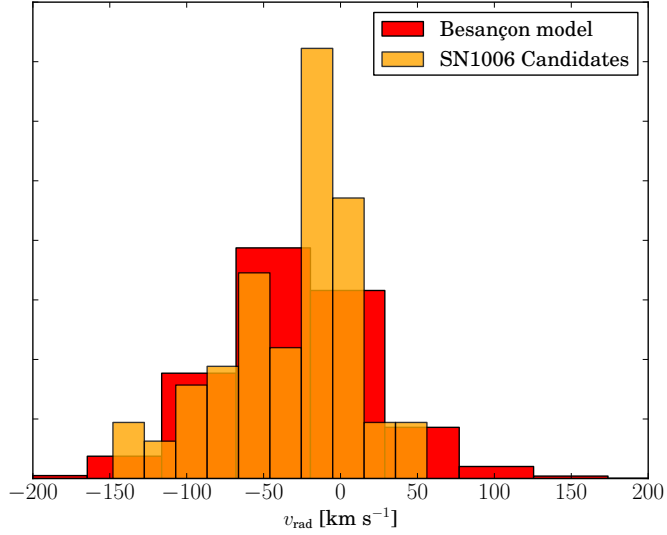


Figure 4.2 example caption

Initially we had tried to fit the rotational velocity as an additional parameter in the determination of stellar parameters. For the low signal to noise spectra the optimization algorithm suggested very high rotations. A simple manual inspection revealed that this was not the case. In fourier space (priv. communication Ken Freeman) it becomes much easier to determine repetitive structures like line profiles. Initially we tried a simple fourier transform of the spectra without using a window function. This caused a very noisy fourier spectrum, which was hard to analyse. Welch (1967), on the other hand describes a very robust method of obtaining periodic information of spectra. He suggests dividing the spectra into overlapping subsegments. These are then multiplied with a window function (in our case "Hann"-window) and transformed into the fourier domain. All fourier segments are then averaged, which provides a very clean fourier spectrum. Figure ?? shows the periodogram of synthetic spectra with different rotation and different S/N-ratios. For synthetic data this methods worked even for a S/N of roughly 5. Measuring rotation in our real data remained too difficult in the low S/N regime.

We however discovered a different way of measuring line profiles (and inferring rotation). For a description of this method we review part of the spectrum synthesis. The intrinsic spectrum ( $f_{\text{spectrum}}$ ) is created at the photosphere of the star (but already broadened by many factors like thermal broadening). A rotation of that star convolves the spectrum with a rotational broadening kernel ( $g_{\text{rotation}}$ ). The light travels to earth and then is convolved again with the instrument profile ( $h_{\text{instrument}}$ ) before being recorded on the detector. Let's assume we can create a synthetic spectra matching the intrinsic stellar one which has not been convolved by either rotation or the instrument ( $f_{\text{synthetic}}$ ). A convolution can be

described in Fourier space in the following way,

$$f_{\text{observed}} = f_{\text{spectrum}} \otimes \underbrace{g_{\text{rotation}} \otimes h_{\text{instrument}}}_{f_{\text{profile}}} \\ F(f_{\text{spectrum}} \otimes g_{\text{rotation}} \otimes h_{\text{instrument}}) = F(f_{\text{spectrum}}) \times F(g_{\text{rotation}}) \times F(h_{\text{instrument}}) \\ \Rightarrow \frac{F(f_{\text{observed}})}{F(f_{\text{synthetic}})} \approx F(f_{\text{profile}}),$$

where  $F$  denotes the fourier transform. This yields the line profile which we can roughly separate into the instrument profile (using prior knowledge about the resolution of the instrument) and a rotational kernel . This technique is by no means a new idea. It has been described by a selection of authors (e.g. Gray, 1977). This is the basic method that *fxcor* relies on. *fxcor* however only measures the peak of the profile to estimate the radial velocity. Our collaborator John Laird has used this technique to successfully extract the rotation for some of the stars (see Table ??). We are planning to combine the previously described Welch's method and this fourier cross-correlation to reliably measure rotation in low S/N data. This is currently still research in progress.

#### 4.3.5. Stellar Parameters

To get detailed stellar parameters we employ a technique using a grid in  $T_{\text{eff}}$ ,  $\log g$  and  $[\text{Fe}/\text{H}]$ . MOOG(Sneden, 1973) was used to synthesize the spectral grid using the model stellar atmospheres by Castelli & Kurucz (2003). Line wings were taken into account up to 8 Åaway from line centre, which seemed to be a reasonable compromise between grid creation time and accuracy. For the atomic lines we merged values from the VALD-2 database (Kupka et al., 2000) with adjusted values (to reproduce the Arcturus and the Sun) from ?. We used the measured molecular lines described in Kurucz & Bell (1995). The grid extends from 3500 K to 7500 K in  $T_{\text{eff}}$  with a stepsize of 250 K, in  $\log g$  it ranges from 0 to 5 with a stepsize of 0.5 and in  $[\text{Fe}/\text{H}]$  it ranges from -2.5 to 0.5 with a stepsize of 0.5 (with an extra set of points at 0.2).

We used the appropriate sections from the Solar spectrum (?) and the Arcturus spectrum ? to calibrate our spectral grid. We determined stellar parameters by first finding the best fitting grid point and then using the minimizer MINUIT to find a minimum by interpolating between the gridpoints (using Barber et al., 1996). For a more detailed explanation of the n-dimensional interpolation see Chapter ?. For the Sun we obtain stellar parameters of  $T_{\text{eff}}=5825$  K,  $\log g=4.4$  and  $[\text{Fe}/\text{H}]=-0.12$  and for Arcturus we obtain stellar parameters of  $T_{\text{eff}}=4336$  K,  $\log g=1.9$ ,  $[\text{Fe}/\text{H}]=-0.67$ . We acknowledge the error in measurement, but believe our spectral grid to be accurate enough for distinguishing a potential donor candidate against an unrelated star.

To measure our observed spectra we need to first fit the continuum. We decided for a Legendre polynomial with a maximum order of 3 and a sigma clipping algorithm. The order that gave the lowest RMS of the fit was used. After determining initial parameters we would divide by synthetic spectrum with these parameters and fit the continuum again as some parameters (like  $[\text{Fe}/\text{H}]$ ) are very continuum sensitive.

To calibrate this analysis pipeline we have measured stellar parameters for synthetically created spectra using the real sun and arcturus spectra as an input. We multiplied these spectra with an artificial continuum and introduced artificial noise to recreate a S/N-ratio of 5 (similar to the measure low S/N spectra) and added rotation in some cases. Both Solar and Arcturus spectrum were introduced into the analysis pipeline with artificially added noise and rotation. As rotation can not yet be reliably identified by our techniques (see Section 4.3.4) we sometimes obtained measurements that suggested a rotationally convolved Arcturus to be a main-sequence. As higher surface gravity broadens the wings of some spectral lines, our algorithm confused the rotational broadened lines of the artificially rotating Arcturus spectrum with gravity broadening.

In summary, we have not yet been able to reliably extract stellar parameters from the observerd spectra. Initial experiments with the low S/N spectra of individual stars often yielded the same parameters for the same star. This is a promising result and suggests, that if we can reliably determine the line profile we will be able to extract stellar parameters for the candidates.

## 4.4. Conclusions

The initial measurements of kinematics, photometric temperatures and initial rotational velocities suggest no unusual stars in the current set. None of the stars show any particularly peculiar radial velocity. We note however that the spread in radial velocity in this direction is large and that a potential donor star might not be visible as a kinematic outlier. The current measurements of rotation also do not show any strong outliers. Once we obtain measurements about evolutionary and more precise measurements about the temperatures we will be able to infer distances. The relatively low reddening of the field will make this a straightforward exercise. Distances often offer suggestive evidence for involvement (e.g. Tycho-Gin SN1572). If the further analysis does not, as currently hinted, reveal an unambiguously identifiable donor star for SN 1006 we will have have to analyze the caveats of such a find. In our opinion the determination of the center is one of the largest caveats. Measurements like [Winkler et al. \(2005\)](#) cast doubt on a precise determination of the center. Their research suggests that the center of the iron core is offset from the geometric center determined by the shocked **ISM**. This does, however, not mean that the center of mass (where a donor star would reside) is necessarily offcenter. In fact, [Maeda et al. \(2010\)](#) suggest that the innermost ejecta is offset from the center of mass, which suggests that the center of the iron core will be different than the center of mass. In summary, this caveat is probably not easily resolved and we will have to hope that our generous choice in radius around the geometric center incorporates any such errors. Other groups are also currently surveying SN1006 with in a larger but photometrically shallower field (priv. communication Pilar Ruiz-Lapuente). Their search also has not revealed any unusual star. Finally, the donor star that we are trying to find might already be to faint for our observations. Although scenarios with very faint stellar remnants exist, most current scenarios do not suggest this (see discussion in section ??.) The other very real possibility is that **SNe Ia** in general or at least SN 1006 did not have a donor star. A DD-scenario would definitley explain the observational lack of the thought after companion. Finally, the last remnant to be subjected to such an intensive search will be Kepler. Kepler seems

to be different from either SN1572 and SN1006 due to detection of interaction with CSM. Observational facts of the Kepler remnant (SN1604) as well as the description of the donor star search will be discussed in ??

# CHAPTER 5

---

## Automatic fitting of optical Type Ia Supernova spectra - the Dalek code

The last chapters (Chapters ??) were dedicated to the hunt for donor stars and did not use the measurements from the SNe Ia themselves. In this chapter we will describe the extraction of yields and energies from optical spectra as well as the automation of this process.

The two main sources of information in spectra, are the spectra themselves as well as their time evolution. There have been a few attempts to extract the details of the stellar explosions from one or two of these sources. All of them employ the technique of fitting the spectra using synthetic spectra. One of the main parts is the radiative transfer program that creates the synthetic spectra. There are several different radiative transfer-codes in the community.

Fisher (2000) wrote a very simple radiative transfer code called SYNOW. SYNOW is a highly parametrized code and thus is mainly used for line identification rather than actual fitting of SN Ia spectra. The main code used in this work is a further development of the code described in Mazzali & Lucy (1993) and Mazzali (2000), henceforth named the MLMC. Compared to the SYNOW-code the MLMC-code calculates a radiative equilibrium temperature and uses this to compute internally consistent ionization ratios. In addition MLMC takes electron scattering into account as well as allowing for photon branching.

Codes such as PHOENIX Hauschildt & Baron (1999), SEDONA Kasen et al. (2006) and ARTIS Kromer & Sim (2009) are powerful 3D radiative transfer codes. They are the most “physical” codes available but take hours to days on supercomputers to produce spectra. These codes, however, are not feasible for fitting many observed spectra as they take too long for each iteration.

The main aim of this work is to automatically fit the torrent of observed spectra expected from the current and next generation of supernova searches. We opted to use the MLMC-code as it provides a good compromise between speed and physical “realism”.

In section 5.1 we will introduce the inner-workings of the **MLMC**-code. We will discuss the properties of the parameter space on one example fit in ???. Section ?? is meant as an introduction to genetic algorithms (henceforth GA), which are the optimization strategies of choice in the automatization of the **MLMC**. We will present the current implementation of the autofitting code in Section 5.4. We have named the code Dalek for no particular reason. Finally we will conclude and give an outlook over future work of this unfinished project in section 5.5.

## 5.1. The MLMC-Code

As described in Section 1.3.4 the supernova can be divided in two different phases: the photospheric phase and the nebular phase. The **MLMC**-code only creates synthetic spectra for **SN Ia** in the photospheric phase. In this photospheric phase the supernova is treated like a sharp photosphere emitting a black-body spectrum with a fast moving ejecta-layer on top.

### 5.1.1. Radiative Transfer

Radiative transfer calculations can be described as the aim to find the wavelength dependent attenuation of a given input Flux  $F_0$ . This wavelength dependant attenuation factor is called the opacity  $\tau$ :

$$F(\lambda) = F_0(\lambda) e^{-\tau(\lambda)},$$

where  $F$  is the observed Flux and  $F_0$  is an assumed distribution of input flux before being reprocessed by a plasma which imposes the attenuation factor  $e^{-\tau}$ . There are many physical processes in supernova radiative transfer. Of those the bound-free opacity has the biggest contribution to the final spectrum. In addition, Thompson scattering is thought to have an important effect in redistributing flux. As **MLMC** is required to run fast only bound-free opacity as well as Thompson scattering is implemented in the code.

Unlike stellar atmospheres in supernova ejecta one needs to consider the photon's doppler shift in relation to the surrounding medium. One major assumption that the code makes is that of the Sobolev approximation. This means that the interaction between photon and line resonance happens only at one specific point (thus disregarding any broadening effects of the line). For example a photon in free flight from the photosphere will be able to interact with resonance lines of lower and lower frequencies. This Sobolev approximation is one important factor of making the code fast yet still reproducing the observed spectra rather well.

In addition the **MLMC** assumes the ejecta to be in homologous expansion. This means that the velocity is a linear function of the radius:

$$v = r/t.$$

Combining both the Sobolev approximation with the assumption of homologous expansion yields this relatively simple formula for line opacities:

$$\tau_{lu} = \frac{\pi e^2}{m_e c} f \lambda t_{\text{exp}} n_l \left( 1 - \frac{g_l n_u}{g_u n_l} \right),$$

where  $\tau_{lu}$  denotes the opacity going from the lower state to the upper state of an atom,  $e$  is the electron charge,  $m_e$  is the electron mass,  $f$  is the oscillator strength of the line,  $\lambda$  denotes the wavelength,  $t_{\text{exp}}$  the time since explosion,  $n_x$  the number of atoms in the state  $x$  and  $g_x$  is the statistical weight of the state  $x$ .

Although producing relatively good synthetic spectra, the assumptions of homologous expansion and Sobolev approximation have their caveats. In the case of homologous expansion it is thought to be a very good approximations in the first few minutes after the explosion. The main caveat for Sobolev approximation is that a line is not a delta-function, as assumed in the Sobolev approximation. If too strong bound-bound lines are close in frequency space it can lead to the first line shielding the second line. In summary for fast supernova fitting both approximations seem to still allow for a very well fitting spectrum.

We have discussed the propagation of the photons in the plasma but have not discussed the state of the plasma yet. The simplest assumption for the state one can make is local thermodynamic equilibrium (henceforth LTE). In this case the Boltzmann formula describes the level populations in a single ion:

$$\frac{n_j}{n_{\text{ground}}} = \frac{g_j}{g_{\text{ground}}} e^{-(\epsilon_j - \epsilon_{\text{ground}})/kT}$$

Similarly we can calculate the ionization state using the Saha-equation:

$$\frac{N_j}{N_{j+1}} = n_e \frac{U_j(T)}{U_{j+1}(T)} C_I T^{-3/2} e^{\chi/kT},$$

where  $N_x$  are the total ion population with ionization state  $x$ ,  $U_x$  is the partition function for the ionization state  $x$ ,  $n_e$  is the number density of electrons,  $C_I$  is a universal constant and all other symbols have their usual meaning. As the ionization likelihood depends on the internal electronic state of the atom the partition function sums up over these different states:

$$U_j = \sum_i g_{i,j} e^{-\frac{E_{i,j}}{kT}},$$

where  $i$  describes the excitation states,  $j$  the ionization states and  $g_{i,j}$  the statistical weight of the state  $i, j$ . The sum normally diverges slowly so one in practice just sums up until a highly excited state.

The **MLMC** uses the *nebular approximation* which will calculate the excitation and ionization state of the SNe at nearly LTE cost. In this nebular approximation they introduce a dilution factor  $W$ . This is a purely geometrical factor. Treating the photosphere as a point source the factor would result in  $W = 1/r^2$  with  $r$  being the distance from the center. As the photosphere is expanded the dilution factor has a slightly more complex formula. An important point to note is that purely theoretical at the photosphere the dilution factor is 0.5. The mean intensity for the supernova at a specific zone thus is given as:

$$J = WB(T_R),$$

where  $T_R$  is the radiative temperature. The radiative temperature is estimated in the **MLMC** by matching the mean frequency of  $B(T_R)$  with the mean frequency of the photon packets in the current zone (Wien approximation).  $W$  is chosen so that the frequency-integrated intensity matches the photon distribution.

Using  $W$  and  $J$  one now can calculate the electronic and ionization states of the plasma:

$$\frac{n_j}{n_{\text{ground}}} = W \left( \frac{n_j}{n_{\text{ground}}} \right)_{T_R}^{\text{LTE}}$$

and

$$\frac{N_j}{N_{j+1} n_e} = W \left( \frac{N_j}{N_{j+1} n_e} \right)_{T_R}^{\text{LTE}}$$

These approximations do not take into account physical processes like recombination to excited states and the influence of meta-stable levels. They do reproduce the physical state of the plasma relatively well on the other hand and allow for the fast computation of a synthetic spectrum.

### 5.1.2. Monte Carlo radiative transfer

The ejecta in the **MLMC**-code is divided into 20 concentric shells with an equal thickness in  $1/r$ , where  $r$  is the radius from the centre of the explosion. These shells have different abundances calculated at each shell midpoint from the well known empirical model W7 ([Nomoto et al., 1984](#)). There is a *stratified* version of the code that allows for different abundances in each shell. We have opted to use the simple homogeneous version as the parameter space is very complex even for this homogeneous version. We plan to extend the automatic fitting procedure to use the stratified version at a later date. In addition, we assume a time since explosion  $t_{\text{exp}}$  from the photometric maximum and a rise time estimate of 19.5 days. The photospheric velocity  $v_{\text{ph}}$ , the bolometric luminosity  $L_{\text{bol}}$  and abundances for the chosen elements are the input parameters to the **MLMC**-code.

The **MLMC** does not work with individual photons, but with photon packets. Each photon packet, described by frequency and number of photons, and contains the same energy (more photons per packet in the red than in the blue). There are two ways to treat photon interaction. For a pure scattering interaction the photon packet is absorbed at a resonance frequency and then instantaneously reemitted with the same frequency as well as number of photons into a random direction. Newer versions of the **MLMC** (used in this work), however contain a photon branching implementation. In this case the photon packet is absorbed by the atom and has the chance to be emitted through a different transition. This transition is chosen by a weighted random process. The number of photons in the packet is adjusted to conserve the co-moving energy of the packet. Our one dimensional model is divided into multiple geometric shells. They do have a density Using an initial guess of  $T_{\text{eff}}$  for the photosphere, one can calculate the plasma condition in each shell.

The Monte-Carlo simulation begins. A photon packet is emitted with a random frequency and a random angle drawn from a Blackbody distribution  $B(T)$ . An event optical depth is calculated from a uniform random distribution so that  $\tau_{\text{event}} = -\ln(z); z \in (0, 1]$ . There are three possible outcomes for the photon in each Monte Carlo step: We calculate the length of the path ( $s_e$ ) that the packet can travel freely before  $\tau_{\text{event}}$  is equal to the Thompson scattering opacity  $\tau_{\text{event}} = \sigma_T n_e s_e$ . Next we calculate the same path length for the lines  $s_l$  using as a target opacity  $\tau_e + \tau_{\text{line}}$ . If both paths are longer than the path to exit the current shell, then the photon exits the current zone and a new Monte Carlo step begins. In the case that  $s_e$  is the shortest then Thompson scattering occurs and the photon is assigned a

new direction and a new  $\tau_{\text{event}}$  is drawn and we start anew. In the case of line scattering the excited atom can de-excite through many lines. MLMC randomly chooses a downward transition for the whole packet (taking the appropriate weights into account). The number of photons in the packet is adjusted to ensure that the energy is conserved in the comoving frame.

There are two possibilities for the final fate of the photon. Either it is reabsorbed into the photosphere or is emitted from the supernova. When initializing the state of the plasma one assumes an initial guess for the photon temperature. An initializing Monte-Carlo simulation runs and records each packet status at the mid-point of each shell. This information is used to calculate a new photospheric temperature and a updated plasma conditions (level population and ionization). This procedure is repeated until the photospheric temperature converges. Once convergence is reached the actual Monte-Carlo simulation begins.

The final spectrum is not calculated using the escaping photons. Instead we calculate the optical depths from the escaping photons and then calculate the emerging spectrum using the formal integral. This has the advantage of reducing noise in the spectrum due to Monte-Carlo noise and gives very good results. A more detailed description of the code can be found in Mazzali & Lucy (1993) and Mazzali (2000).

## 5.2. Manually fitting a Type Ia supernova

When fitting manually there are several features that help guide the direction of the fit. We will attempt to explain this by using a spectrum of SN2002bo 10 days before maximum (Benetti et al., 2004). Directly measurable are the redshift of the supernova (and implied distance) and the time of the spectrum relative to maximum. We calculate the time since explosion ( $t_{\text{exp}}$ ) using the photometric maximum and assuming a rise time of 19.5 days. The other parameters are initialized using empirical data (see section ??).

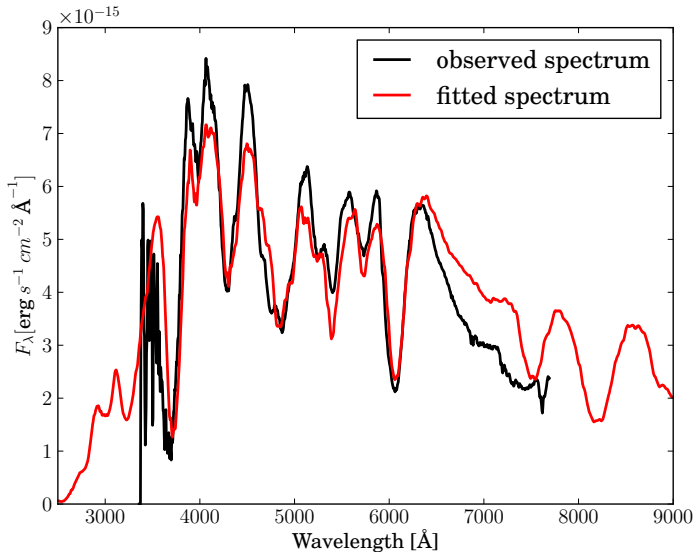


**Figure 5.1** Spectrum of SN 2002bo (Benetti et al., 2004) with MLMC-fit by Hachinger (2007). The excess in redwards of 6500 Å is a common problematic features of these fits.

**Table 5.1** Abundance parameters for best fit

Atom	Abundance
Carbon	0.08 %
Oxygen	54.9 %
Magnesium	10 %
Silicon	25 %
Sulfur	4.5 %
Calcium	1 %
Titanium	0.01 %
Chromium	0.07 %
primordial Iron	0.07 %
undecayed Nickel	1.5 %

Stephan Hachinger has kindly provided his manually obtained best fitting parameters ( for the supernova at this stage (see Figure 5.1). The best fitting parameters for this spectrum are  $\log L/L_{\odot} = 9.05$  and  $v_{\text{ph}} = 11700$ . We have listed the non-zero abundances in Table ???. Nickel is often given in terms of undecayed nickel ( $\text{Ni}_0$ ) and will then split up into its daughter nuclei  $^{56}\text{Co}$  and  $^{56}\text{Fe}$ .  $Fe_0$  designates the primordial iron abundance and is added to the iron abundance which results from the nickel decay. We assume in any further discussions in this work that cobalt is always  $^{56}\text{Co}$  and is never assumed to be stable.

In Figure 5.1 P-Cygni profiles of many features are easily visible. The calcium line in the blue can be seen to be blueshifted in relation to the model. This property is not unusual and is thought to come from high velocity calcium components at the outer edge of the ejecta. This can be often rectified in the stratified version of the MLMC-code. The next major known discrepancy is the excess of flux redwards of  $\approx 6200\text{\AA}$ . This is a common problem as the wrongful assumption of an underlying black body spectrum overestimates the flux in this region. When fitting manually often one tries to fit the depth of the lines instead of the continuum.

There are three main parameters that have the most influence on the overall spectrum fit: Luminosity, photospheric velocity and abundance in iron group elements. A large offset in  $L$  to the best fit parameter is easily visible as a large offset of the continuum (see Figure 5.2. Thus it is easy to constrain the parameter space in  $L$ .  $L$  also has influence on the temperature of the model through:

$$L_{\text{bol}} = 4\pi\sigma R^2 T^4 = 4\pi\sigma v_{\text{ph}} t_{\text{exp.}}$$

Velocity in astronomy is often measured using the doppler shift of atomic lines. In this case however it is hard to measure the photospheric velocity from atomic lines. Lines are created at different depths and thus at different velocities. This smears out the line profiles which makes fitting velocities nearly impossible using this technique. The main impact of photospheric velocity is establishing the temperature structure with the given luminosity. A model with a too high photospheric velocity will have expanded more than the observed spectrum and thus will be cooler. This results in a spectrum that is too luminous in the red and not luminous enough in the blue (see Figure 5.3). A secondary effect is that the ion population will be off. This can be determined by judging the fit of SiII lines versus the fit of SiIII lines.

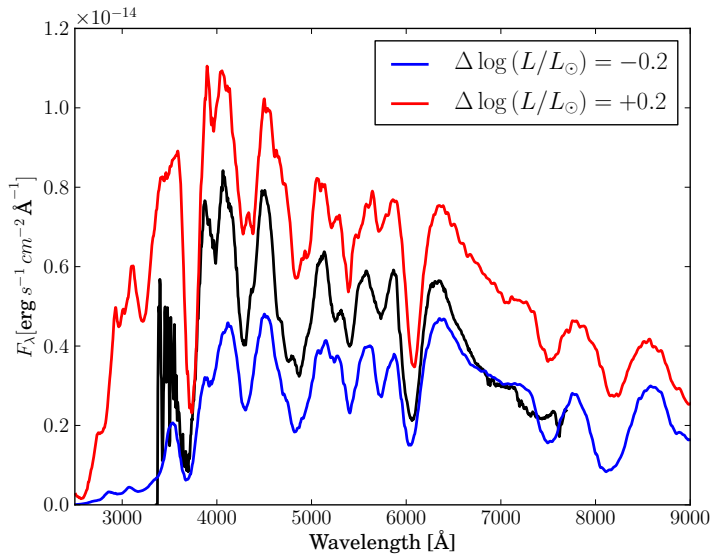


**Figure 5.2** We have perturbed the luminosity around the best fit value. The most noticeable effect is the continuum offset. There is also a slight change in the overall slope of the spectrum.

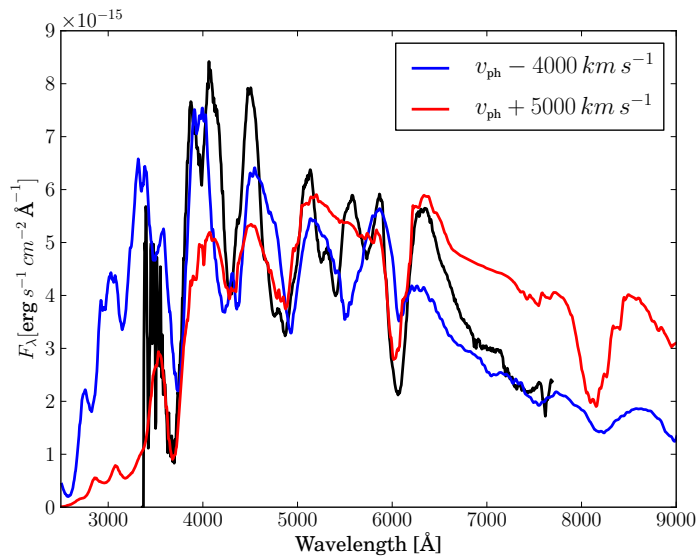


**Figure 5.3** The photospheric velocity has been perturbed around the bestfit. The slope of the spectrum changes a too small velocity produces a hot blue spectrum, a too large velocity a cold red spectrum.

The initial abundances for each fit are determined by integrating the abundances above the photosphere in the W7 model (Nomoto et al., 1984).

The IGE have a similar influence on the overall flux distribution as the photospheric velocity. We assume, as discussed previously, no stable Cobalt. The input parameters for Nickel, Cobalt and Iron are the undecayed  $^{56}\text{Ni}_0$  and the primordial  $^{56}\text{Fe}_0$ . We use the time since explosion to calculate the abundances using radioactive decay. The other important IGE s are Titanium and Chromium which have no easily identifiable single lines in the observed spectra. All IGE elements reprocess the flux heavily by absorbing in the bluewards of  $\approx 3800 \text{ \AA}$  and fluoresce in the red part of the spectrum. For example, a too high abundance will suppress the flux in the blue too much and will cause the spectrum to be over-luminous in the red (see Figure ??). Although physically different from the photospheric velocity, phenomenologically these are similar. The degeneracy is broken by identifiable Fe-Lines in the red part of the spectrum as well as the ionization balance determined by the temperature (mainly influenced by photospheric velocity and luminosity). This near degeneracy causes a very complex parameter space. We disregard the elements Scandium, Vanadium and Manganese as they seem to have little influence on the spectrum at their predicted abundances.

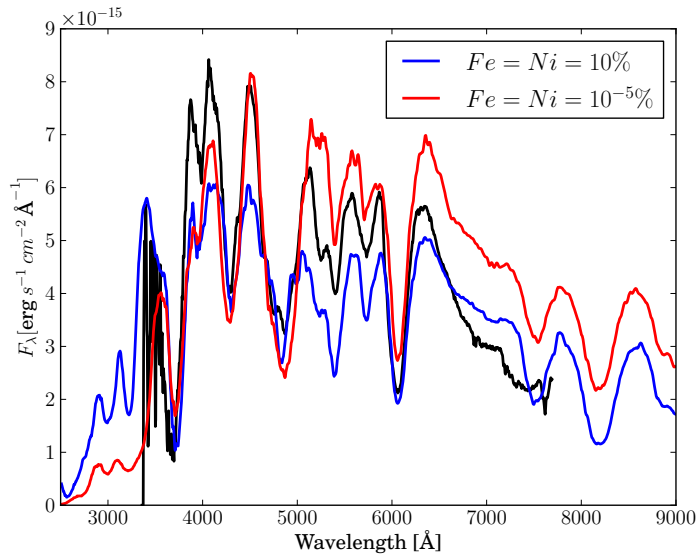


**Figure 5.4** When changing the IGE (in this case we have only changed iron and Nickel) the flux is altered in the blue and red part. Too much IGE s and there's not enough flux in the blue and too much flux in the red and vice versa.

There are six other abundances that are taken into account when fitting: Carbon, Oxygen, Magnesium, Silicon, Sulfur and Calcium (see Figure 5.5). Oxygen does not have lines except the Oxygen triplet at  $7778 \text{ \AA}$  and plays a special role in the fitting process. Oxygen acts as a buffer element and is assigned the remaining fraction that is left after all elements have been given abundances. We do acknowledge that this might physically not be correct and a change in the density structure would be more appropriate. This, however would introduce an additional free parameter and make fits much more complex.

Judging the fit of the CaII line at  $3700 \text{ \AA}$  is relatively easy and thus the calcium abundance

is usually changed first. Additionally, the choice of temperature imposed by photospheric velocity and luminosity does not have an immense influence on this line. One caveat however is that the CaII line saturates at a certain abundance. If the observed CaII line is close to that limit one can only extract a lower limit for Calcium. Silicon and Sulfur are usually the next elements to be fine-tuned. Both of these elements are linked through nuclear synthesis and we don't expect there to be more Sulfur than Silicon. We also expect no less Sulfur than a third of Silicon. Silicon also provides an important measure for temperature through the ionization balance of SiII to SiIII (see Figure 5.5). The strong MgII feature near 4300 Å helps constrains the Magnesium abundance. The weak CII feature at  $\approx 6300$  Å is the only line to provide constraints for the carbon abundance. In most SNe Ia-spectra this line is weak or not visible.

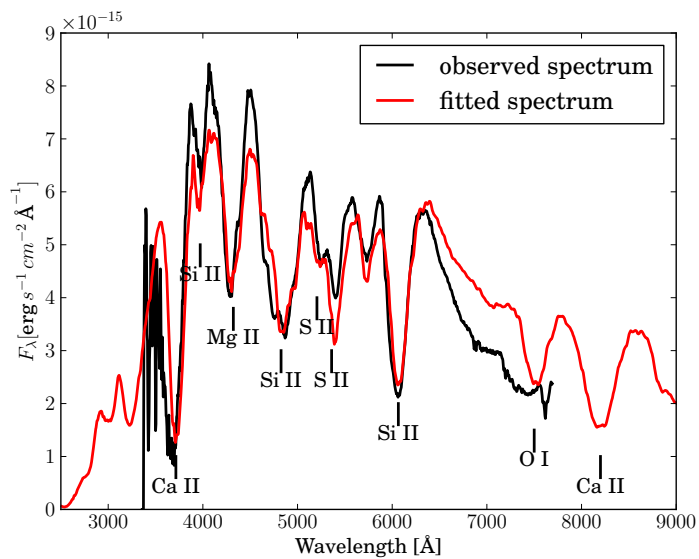


**Figure 5.5** We have identified some of the strongest lines that are scrutinized when fitting a SN Ia spectrum.

The fitting process involves first adjusting luminosity and then IGEs as well as photospheric velocity. This is followed by adjusting the other elemental abundances from the initial W7 values (Nomoto et al., 1984). After the elemental abundances are adjusted we re-adjust the luminosity, photospheric velocity and IGE. This iterative process continues until a satisfactory fit has been obtained. When closing in on the optimal fit we do observe the dilution factor. Purely theoretical we would expect this to be close to 0.5 for a “physical” fit. We do, however accept values between 0.4 and 0.7 as physical. This large range is accepted due to numerical fluctuation and approximations made by the MLMC. The parameters are often improved further by checking their time evolution through fits of photospheric spectra at different times.

In summary, the fitting of a supernova is a complex procedure and requires a lot of practice. For automating this process we initially tested simple gradient methods. These failed abysmally. We quickly discovered the search space is too complex and evaluation time takes too long (each synthetic spectrum roughly one minute on a modern computer) to use these simple methods. Research in numerical optimization techniques has made significant progress in the last decades. These areas of mathematics have yielded impressive

algorithms. Genetic algorithms are easy to implement and are intrinsically parallel. A perfect match for our problem.

### 5.3. Genetic Algorithms

Finding optimal solutions in complex search spaces is one of the main fields in numerical mathematics. They have wide ranging applications in engineering, bio sciences and physical sciences. There have been several immense advances in optimization algorithms over the last decades. Among them is the remarkable feat of quickly finding solutions for famous traveling salesman problem with simulated annealing ([Kirkpatrick et al., 1983](#)) and later with ant colony optimization ([Dorigo & Gambardella, 1997](#)).

Another major accomplishment was the development of evolutionary algorithms and subsequently genetic algorithms. The idea of an algorithm which imitates the principle of natural evolution was first introduced by [Holland \(1962\)](#). These evolutionary algorithms have since become a sizeable subfield of numerical optimization. Genetic algorithms (henceforth **GA**), a subclass of evolutionary algorithms, were further developed by John Holland's student David Goldberg. ([Goldberg, 1989](#)) is the standard textbook for **GAs**.

Optimization algorithms have two seemingly conflicting goals: exploiting good leads (optimum seeking) while still exploring the parameter space sufficiently. Simple algorithms like Hillclimbing (randomly selecting a point in the neighbourhood of the current point and then picking the more optimal point as the new basis) will exploit good leads but will neglect to explore the search space leading to the convergence on local optima. This often leads to be stuck at extrema. Whereas random searches are excellent at exploring the search space but will fail to quickly converge on an optimal solution. Which algorithm to use, naturally depends on the type of parameter space. Spaces with independent variables can be solved relatively simply by employing optimum seeking methods. Random search algorithms are suited to parameter spaces with highly co-dependant variables. Genetic algorithms do strike a balance between exploration and exploiting the current best solution. Consequently they can be applied to a wide range of different parameter spaces.

Genetic algorithms are a heuristic search technique to find optimal solutions in n-dimensional search spaces. Generally in optimization we consider the function  $f(\vec{x})$  with the multi-dimensional solution  $\vec{y}$ . In addition, we define a figure-of-merit function  $g(\vec{y}) = s$  where  $s$  is a scalar. It is the goal to find the input vector  $\vec{x}$  to maximize or minimize  $s$ . In **GAs** a single solution ( $\vec{x}$ ) is called an individual (sometimes also referred to as a genome). The individual components of the vector  $\vec{x}$  are referred to as the genes. We also differentiate between the vector representation called genotype, and the solution vector for an individual ( $\vec{y}$  using the previous notation) called phenotype. This is similar to biology where the input  $\vec{x}$  can be thought of as the DNA sequence. The phenotype in biology however does not resemble a vector. Mathematically speaking it is possible to have multiple genotypes map to one phenotype, however each genotype only maps to one phenotype. The figure-of-merit function  $g(\vec{y}) = s$  is often referred to as the fitness function. Following the notation of ([Michalewicz, 1994](#)) we introduce the population  $P(t)$  with the individuals (sometimes referred to as genomes)  $\{p_1^t, \dots, p_n^t\}$ , where  $t$  denotes the iteration (also called generation). Each individual ( $p_i^t$ ) is a data structure consisting of a vector  $\vec{x}_i$  and its corresponding fitness scalar  $s_i$ . When we speak of evaluating  $p_i^t$  we mean that we use  $g(f(\vec{x}_i)) = s_i$  to determine

the fitness. A new population (or generation)  $P(t + 1)$  is formed by choosing, in the *select step*, the more fit individuals. Some or all of the new population undergo transformations in the *recombine step*. Generically these transformations are called genetic operators. We define unary transformations, which create new individuals by small changes in single individuals called mutations. Higher order transformations called crossovers combine the traits of multiple individuals to form a next generation individual. After the new population has been created in the *recombine step*, it is evaluated (perform the computation  $g(f(\vec{x}_i)) = s_i$ ) and the *select step* begins anew.

This procedure is repeated until the best individual has reached a certain threshold fitness (see Algorithm ??).

---

**Algorithm 1** Structure of a genetic algorithm

---

```

 $t \leftarrow 0$ 
initialize  $P(t)$ 
evaluate  $P(t)$ 
while (not termination condition) do
     $t \leftarrow t + 1$ 
    select  $P(t)$  from  $P(t - 1)$ 
    recombine  $P(t)$ 
    evaluate  $P(t)$ 
end while

```

---

An optimization problem needs to have the following traits to be solvable by a GA:

- a genetic representation of the search space (e.g. a vector)
- a function (or a chain of functions) that can calculate a fitness for a genetic representation
- transformations that create a new population/generation out of selected members of the old population/generation
- a method of creating an initial population

If the problem fulfills all these requirements one can start constructing a GA. This involves multiple steps the first of which is choosing a suitable genetic representation for each solution in the parameter space.

**Genetic Representation:** There are two main ways to represent a genome: binary encoding and value encoding (sometimes called gray encoding). Binary encoding was the form of encoding used in early genetic algorithms. It offers significant advantages when trying to optimize very simple problems. In one-dimensional problems, for example, value encoding only offers one gene, whereas binary encoding, depending on the requested precision of the value, offers multiple genes. This becomes obvious in the one-dimensional minimization example:  $f(\vec{x}) = (x_0 - 3.141)^2$ . The solution vector that minimizes the problem in value encoding is  $\vec{x} = (3.141)$  using IEEE 754 floating point encoding the optimal vector is  $\vec{x} = (0, 1, 0, 0, 0, 0, 0, 0, 1, 0, 0, 1, 0, 0, 0, 0, 0, 1, 1, 0, 0, 0, 1, 0, 1, 0, 1)$ . There

are however many problems with binary encoding. The so called *hamming cliff* describes the problem that a simple bit-flip at one high encoding bit (occurring in some genetic operators like mutation) can dramatically change the encoded value (e.g. Chakraborty & Janikow, 2003). This can improve covering of search space but also can hinder the code from converging. When using binary encoding for many input variables the genomes can get incredibly long. GAs have been shown to perform poorly for very long genomes. Value encoding often is a natural way to encode the parameters of a problem. In contrast to binary encoding the genetic operators are often much more problem specific. It seems that for the moment value encoding is the preferred method in many cases (e.g. Janikow & Michalewicz, 1991; Wright, 1991; Goldberg, 1990)

Finally, an important encoding to mention is that of permutation encoding. In the famous case of the travelling salesman problem (henceforth TSP) one tries to find the shortest route between  $n$  cities. In this case each city can only be visited once and the route must end in the starting city. There are many algorithms that can solve this problem. Brute force attempts scale with  $O(n!)$  which make them unfeasible. A genetic algorithm can solve this problem by encoding the order (permutation encoding) in which the cities are visited in each genome. There are special genetic operators for permutation encoding. For the TSP there are better algorithms like dynamic programming which can solve the problem with a complexity of  $O(n^2 2^n)$  (see Figure 5.6).

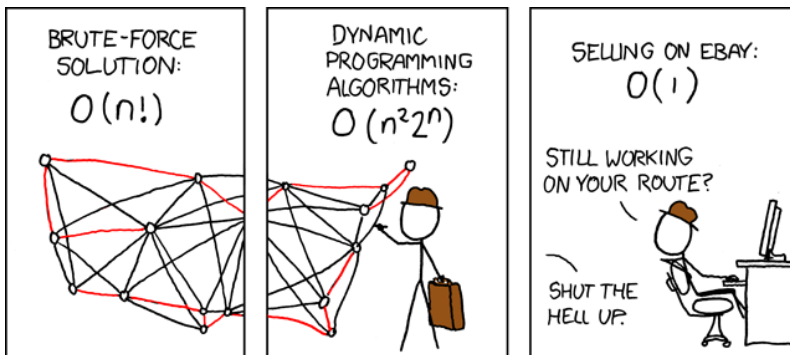


**Figure 5.6** The death of the TSP with the advent of online sales. (reproduced with kind permission by xkcd.com)

The fitness function maps the phenotype ( $\vec{y}$ ) to a scalar. Fitness functions are very problem dependent and are often hard to define. It might not always be possible to find a function that maps desirability to exactly one value (e.g. it is not possible to map desirable traits of a car to one number and optimize that). This class of problem is generally referred to as multi-objective optimization and is an active field in GA-research (Konak et al., 2006). Describing this subfield is outside the scope of this work. A GA is required to follow promising leads but also explore the parameter space. It sometimes happens that a fitness function values a small fraction of individuals extremely high when compared to the rest of the solutions. This can become a problem when this high fitness value is only tied to a few genes. For example, a right value of the first gene could cause much higher fitness than correct values of other genes in a single individual. The subsequent populations will then be reigned by the genes of this one individual which prohibits the GA to explore the search space. In GA-terms individuals with extremely high fitness based on very few genes are called "superindividuals". They can drastically reduce the genetic breadth and

often cause the **GA** to fail. One way to overcome this problem is scaling the fitness of all individuals after they have been computed. There are other steps which can be undertaken in the *select step* described later. The scaling is often a simple algebraic transformation, like linear or exponential scaling. The coefficients for this transformation are often calculated by using the average, minimal and maximal value of the fitness distribution. A specific example can be found in Section 5.4. In summary, fitness functions and scaling are a very crucial part of a successful algorithm. For a description of different scaling methods please refer to ?.

The most basic quantity to consider when choosing the initial population is that of population size. Generally the population size remains the same over the course of a **GA**. The population size should be chosen in relation to the size of the parameter space. A small population size and a large search space can lead the **GA** to find local optima rather than the global optimum. We have in our work chosen a population which is roughly 15 times bigger than the number of genes. After having chosen the population size the most basic method of selecting the initial population is to draw individuals uniformly and randomly from the entire search space. One might however know a probability distribution for the parameter space and can draw randomly weighted by the distribution (e.g. when trying to find parameters for a random star, we can rule a  $20 M_{\odot}$  white dwarf with some likelihood). An initial population that is closer to predicted optimal value will converge faster, but won't explore the parameter space that well.

Once we have evaluated the fitness for each member of the individual population the next step is the *selection step*. There are many different approaches for selecting individuals from the current population to create the next population. Before selecting individuals we can make coarse selection on the entire population. One selection that is often performed is *elitism* in which a fraction of the fittest individuals is selected to advance unaltered to the next generation. On the other hand one can discard a fraction of the least fit individuals. These discarded individuals (including their gene-combinations) won't be used in the recombination step. The remaining population is called the mating population.

After we have performed a coarse selection on the population we start with the recombination step. The first action in the recombination step is the selection of two or more individuals from the mating population and add them to a mating pool. In all our next examples we will assume a mating-pool with only two slots (similar to two parents in biological reproduction). Once the mating pool is filled a new individual is created by combining the genetic information of all members in the mating pool. There is a multitude of options for selecting members from the mating population and adding them to a mating pool (? for an overview see). The most widely used of the selection algorithms is *roulette wheel selection* (see Figure 5.7). *Roulette wheel selection* is in the class of *fitness proportional selection*. In addition to *fitness proportional selection* there is *rank selection*. In rank selection the fitness only influences the rank of the individuals (see Figure 5.8). The previous described fitness scaling and rank selection have similar effects. They do alleviate the problem of "super-individuals" that will dominate the following generations and often lead to the failure of the **GA**. Finally, in *tournament selection* we randomly select two individuals and compare those. The fitter of those two individuals is selected and added to the mating pool.

There are multiple steps for creating a new population from the current mating popula-

tion. First we select two individuals (or more) using our selection process (e.g. *roulette wheel selection*) and place them in a mating pool. The reader should notice that the same individual can be in the mating pool twice! We create one or multiple new individuals (children) from this mating pool and place them in the new population (also known as the next generation). The current mating pool is disbanded and a new one is formed. These steps are repeated until the new population has the same number as the old population (minus the number of individuals that automatically advanced to the new population through *elitism*). There are two main processes to create a new individual from a mating pool: crossover and mutation.

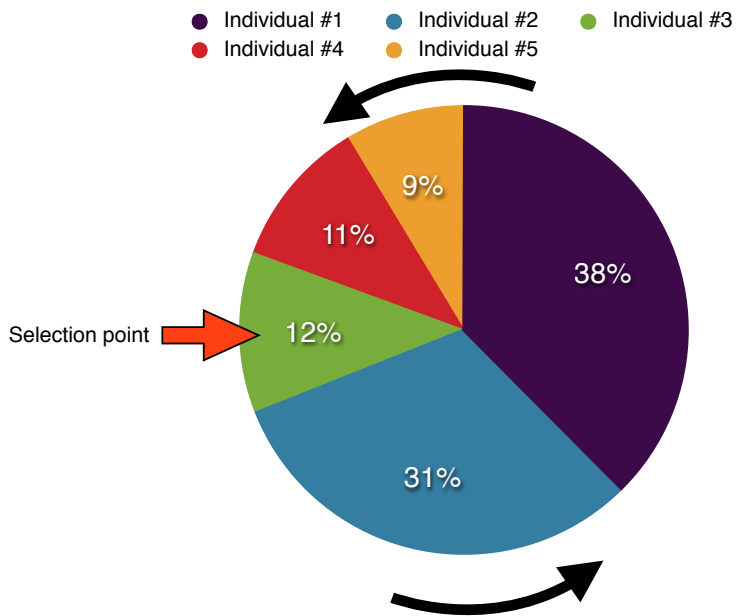


**Figure 5.7** The individual fitnesses are assigned proportional fractions on the roulette wheel. The wheel is then spun and will slowly decelerate and stop at some point. Individuals with a higher fitness have a higher chance of being chosen with this method.

To describe these two options in detail we assume a mating pool with two individuals. The simplest form of a crossover is the single-point crossover (see Figure 5.9). A random integer  $r \in [1, N - 1]$ , where  $N$  describes the number of genes per genome is selected. The new individual is created out of the first  $r$  genes from the first parent and the last  $N - r$  genes from the second parent. Now it is trivial to create a second child (using the same random number  $r$ ) from the mating pool by just switching first and second parent. Two-point crossover is very similar to single-point crossover. Two random numbers are selected and the crossover occurs at these places. Multi-point (see Figure 5.9) is essentially just a extrapolation of two point crossover. Finally, there is uniform cross-over in the case that each gene is selected randomly with equal chance from either parent. Arithmetic crossovers use a function to calculate the new gene from each of the parent genes. For a value encoding this function could be the mean. For a binary encoding the function could be the *and* operator. ???should I include example??? One can mix arithmetic and binary crossovers. For example we select the  $r$  genes from the first parent and create the last  $N - r$  genes by taking the mean of first and second parents' genes. After the new

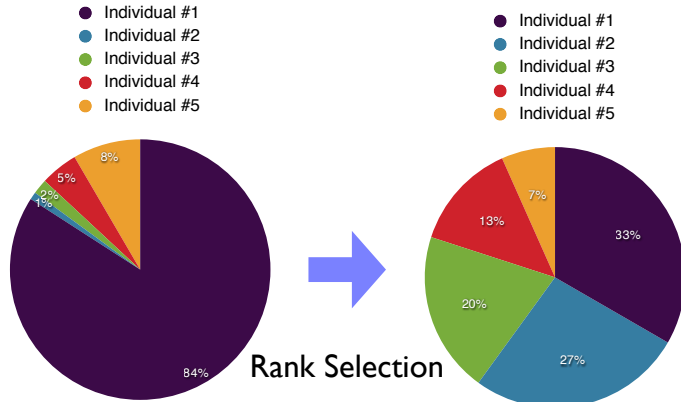


**Figure 5.8** We assign new fitness values to individuals before assigning them probabilities on the roulette wheel. The fitnesses are assigned by location in an ordered list. The least fit individual gets assigned the value 1 the fittest individual the number  $n$ , where  $n$  is the population size. This is can be viewed as a special case of fitness scaling. After the new fitnesses have been chosen we use normal roulette wheel selection to select for the mating pool in the population.

child or children have been created through crossovers they are subjected to the mutation operator. There is a chance for each individual gene (often chosen to be less than 5%) that it is altered. For bit encoding this altering is a simple inversions. There are many options for value encoding. For example one can add or multiply with a random number. Once this step is complete the children are added to the new population.

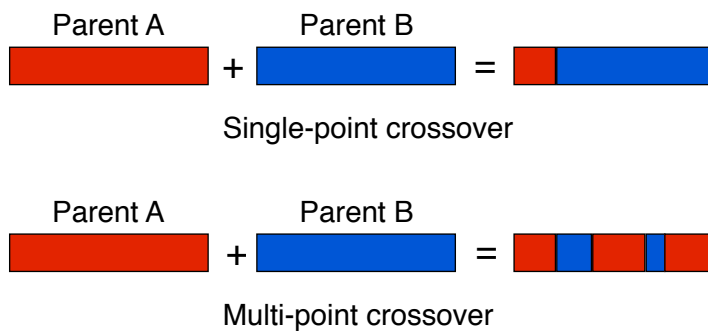


**Figure 5.9** In the single crossover a random point in the Individual is chosen. Before this point the genes are taken from the first parent and after that we use the genes from the second parent. Using the same random number it easily allows for the creation of two children by reversing the roles of first and second parent. The multi-point crossover employs multiple places in the genome where the crossover happens.

### 5.3.1. A simple example

We will illustrate the use of a **GA** on a simple astrophysical problem. The task at hand is to fit an observed spectrum with a synthetic spectrum. The input parameters for this synthetic spectrum are  $T_{\text{eff}}$ ,  $\log g$ ,  $[\text{Fe}/\text{H}]$ ,  $\alpha$ -enhancement,  $V_{\text{rad}}$  and  $V_{\text{rot}}$ . The simplest genetic representation of this is the vector  $\vec{x} = (T_{\text{eff}}, \log g, [\text{Fe}/\text{H}], \alpha, V_{\text{rad}}, V_{\text{rot}})$ .  $\vec{x}$  is the *genotype* of the individual. The resulting synthetic spectrum is the *phenotype*.

For this relatively small number of genes a population size of 75 should suffice. The first step is drawing an initial population. We will draw uniformly randomly from the search space:  $T_{\text{eff}} \in [2000, 9000]$ ,  $\log g \in [0, 5]$ ,  $[\text{Fe}/\text{H}] \in [-5, 1]$ ,  $\alpha \in [0, 0.4]$ ,  $V_{\text{rad}} \in [-100, 100]$  and  $V_{\text{rot}} \in [0, 200]$ . We compute the synthetic spectrum for each individual. The fitness of each individual is the inverse of the root-mean-square of the residuals between the observed and the synthetic spectrum. In the select step we will first advance 10 % of the fittest individuals to the next population unaltered (*elitism*). For the next population to be complete we need  $75 - 8 = 67$  individuals which are created through mating. We select 2 individuals through *roulette wheel selection* and place them in the mating pool. A single crossover point is randomly selected and the child is created. Before being placed in the new population the mutation operator is applied but has a very small chance to mutate any of the child's genes (in this case we choose 2%). This mating step (see Figure ??) is repeated 67 times. The new population now consists of the 8 fittest individuals of the old population and 67 new individuals created by mating. We will then start again to compute the synthetic spectrum and the resulting fitness for each individual of the new population. This loop is continued until one individual or a whole population has reached a preset convergence criterium.

### 5.3.2. Convergence in Genetic Algorithms

A key problem with many **GA**-implementations is the premature convergence on a local optimum. The more complex the search space and the more interlinked the parameters are, the more likely it is that traditional search routines will fail. **GAs** are inherently better at bypassing local optima but are in no way immune to this problem. A feature that separates **GAs** from traditional optimization algorithms is that they will never fully converge. The algorithm will get close to the optimum but due to continued mutation of the individuals the **GA** will in most cases not reach it. To alleviate this problem some authors suggest switching to a different algorithm when close to the optimum solution, whereas others suggest changing the mutation rate over time (see Rudolph, 1994, and references therein). A definite advantage of **GAs** is their parallel nature. Many other search algorithms require the evaluation of one solution to calculate the next step. The inherent parallel nature of **GAs** makes it easy to explore large search spaces in the era of increasingly parallel computing.

There are many advantages to using **GAs**, however one of the unsolved problems is determining a mathematical description for their convergence. The predominate schemata theory explains only a subset of the intrinsic complexity of **GAs**.

### 5.3.3. GA theory schemata theory

The schemata-theory first described by Holland (1975) is one of the accepted theoretical interpretations of GAs. There is some criticism and it is known that this theory only explains part of the complexity that are inherent to GAs (see Whitley, 1994, and references therein). We will describe the basic concepts of schemata using an example in binary encoding (notation adapted from Goldberg, 1989). A schema or similarity template is formed by adding an extra letter to the binary alphabet denoted by \*. Using the ternary alphabet 0, 1, \* we can now describe a pattern matching schemata were the \* symbol can be thought of as *don't care*-symbol. The schemata 0, 1, 0, \* for example, matches both the string 0, 1, 0, 0 and 0, 1, 0, 1. The order of a schema is defined as how many places are not filled by the \*-symbol. The given example is an third order schemata. Schematas provide a powerful way to describe similarities in a set of genomes. A whole population of solutions therefore samples a range of different schematas. Essentially low-order and above-average schemata receive exponentially increasing trials in subsequent generations of a GA. Michalewicz (1994) describe the workings of a GA in the following way: "A genetic algorithm seeks near optimal performance through the juxtaposition of low-order, high-performance schemata, called building blocks". This schemata-theory is the standard explanation for GAs, there are however some examples that violate this (see chapter 3 of Michalewicz, 1994, for some examples).

## 5.4. Genetic Algorithms to fit Type Ia Supernovae: The Dalek Code

As described in Section 5.2 the search-space for fitting SNe Ia is very complex and vast. The parameters that need to be fit are luminosity, photospheric velocity ( $v_{\text{ph}}$ ), Carbon, Magnesium ,Silicon, Sulfur, Calcium, Chromium, initial Ni ( $\text{Ni}_0$ ) and primordial iron ( $\text{Fe}_0$ ). As in the manual fitting example the time since explosion as well as the luminosity distance (for scaling purposes) are given. The evaluation for each spectrum takes roughly one minute on a modern computer which makes it hard to quickly try out different optimization strategies. We initially tried a Newton-Raphson approach with multiple phases. In the first phase the algorithm would adjust luminosity and normally came close to the optimum. In a second phase we tried to let the algorithm re-adjust luminosity, then photospheric velocity and last IGE s. This was modelled after the manual approach that is taken by Hachinger (2007) and (Hachinger, 2011). It took relatively long and would not converge. We realized quickly the search space is far to complicated for such simple methods. In addition, we were limited to one processor with this gradient method as the MLMC itself is not parallel. GAs seem the perfect choice for this problem. They are easy to implement, can easily be parallelised and are relatively immune to local minima. For most of our optimization tests we worked with the supernova SN 2002bo (Benetti et al., 2004). This supernova is believed to be a "Branch"-normal and is spectroscopically well sampled. For most of our tests we worked on the  $t_{\text{exp}}=10.4$  days spectrum, but did not make any other special assumptions about the spectrum. We have used some other spectra and will mention these where applicable.

### 5.4.1. The Dalek Code

After the failed attempts of the multi-phase Newton-Raphson fitter we launched straight into [GAs](#). As described in Section ?? one needs to first create an initial population. One can easily draw uniform randomly for luminosity and  $v_{\text{ph}}$  (within some bounds). This method does not work for the elemental abundances as the sum of the abundances needs to add up to 1. For many normal supernovae the W7-abundances ([Nomoto et al., 1984](#)) give a good starting point. A population that is distributed around the optimum value converges much quicker than a uniformly sampled one. To calculate these abundances we need to know the photospheric velocity. Using data from [Benetti et al. \(2005\)](#) we have estimated an empirical relationship between the time since explosion and the photospheric velocity (see Figure ??). This will serve as a rough first guess.

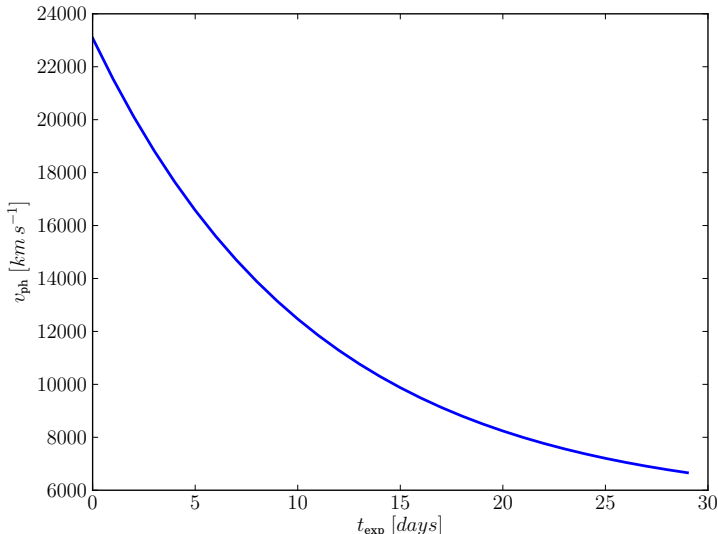


**Figure 5.10** Estimated initial guess for photospheric velocity against days after explosion.

Once we know a  $v_{\text{ph}}$ -estimate we can determine at what depth the photosphere is located in the W7-model. We use this point and integrate outwards to find our initial abundance fractions.

When creating our initial population we draw uniformly random for a preselected luminosity range (for the moment determined manually), a  $v_{\text{ph}}$ -range  $4000 \text{ km s}^{-1}$  above and below the  $v_{\text{ph}}$ -estimate and asymmetric log-normal centered on the abundance estimate from W7. Creating the abundance values brings some problems with it. There are several bounds when it comes to the initial abundance ratios. We have a minimum bound for each abundance (established as the smallest abundance an element can have by [MLMC](#)) at  $10^{-7}$  and a maximum bound which is determined by the requirements that all abundances need to add up to 1. If we would draw the abundances every time in the same order it would mean that the last element to be drawn would always have a very low chance of obtaining a high abundance value. Thus we randomize the order of drawing the elemental abundances. Before we let an individual into the initial population we also check some abundance ratios by employing generous limits that we think are allowed by explosive nucleosynthesis of a [CO-WD](#) (e.g. [Iwamoto et al., 1999](#)).

- $C < 12.5\%$
- $Si > 1\%$
- $Ca < 5\%$
- $Ti + Cr < 1\%$
- $Ni_0 < 80\%$
- $C < O$
- $1 < Si/S\text{-ratio} < 10$
- $Fe_0/Ni_0\text{-ratio} < 10$
- $Cr/Ni_0\text{-ratio} < 10$

If the newly created individual does not conform with these rules it is discarded and a new one is drawn. This process is repeated until we reach our population size which we chose to be 150.

Once the initial population is created it is distributed among the compute nodes by the DALEK code. As we need to explore a large parameter space we use a distributed computing approach. The scheduler part of DALEK code distributes parameter sets to spectrum synthesizers working on different machines across the network. The difficulty is (and the reason that we didn't use a standard implementation like MPI) that we need the DALEK code to reach processors on many different architectures and operating systems. This enables us to harness a large fraction of the institutes computational power. For the order of execution we have chosen a very simple scheduling algorithm that maintains a FiFo batch-queue for the parameter sets and distributes them among the pool of spectrum synthesizers.

The resulting spectra are then subjected to a fitness function. The determination of the fitness function is one of the most crucial choices for the GA to work. The correct fitness function is still a field of active research in the DALEK code. As an initial approach we calculated the mean-square of the residuals remaining from subtracting the observed spectrum and the spectrum of the current individual. This approach has two main issues: For almost all observed spectra in the early phase the fitted spectrum has a large continuum excess beyond 6500 Å(see Figure 5.1). We still regard the line depth and line shape to be correct. As described previously this is a known issue of the MLMC. This large difference in the infrared means that the DALEK code will try to optimize this large offset and pay less regard to a good fit in the rest of the spectrum. To alleviate this we have tried multiple approaches. At first we tried to de-weight the fit in the problematic region. This artificially introduced weighting factor introduces another parameter which might have to change it for the GA to succeed on different spectra. This would defeat the point of an automatic fit. As a second approach we tried to fit and subtract the continuum in the problematic region before creating our fitness figure. In addition, the MLMC supplies us with an estimate of the dilution factor W at the photosphere. This factor is expected to be close to 0.5 (see description in ??). Hachinger (2007) and Hachinger (2011) have found that in all cases a good fit will have a value of the dilution factor between 0.4 and 0.7. We have incorporated

this into the fitness calculation and de-weight spectra with a value outside this range to a great extent. We should mention that we have tried, in addition to calculating the root-mean-square of the spectra, a number of different methods. Most notably we tried to use neural-networks to perform a goodness of fit analysis. We however abandoned this effort as the training set to calibrate neural networks requires a large number of well fitted spectra which are not available.

Once the fitness is calculated for each individual we use the method of fitness scaling to preempt premature convergence in early generations (caused by the so called “super-individuals”) as well as creating a steeper fitness gradient in later generations. We have decided to use a linear fitness scaling as described in [Goldberg \(1989\)](#):

$$f' = af + b,$$

where  $f'$  designates the scaled fitness and  $f$  the raw fitness. In all cases we want to make sure that the average of the scaled fitness  $f'_{\text{avg}}$  equals that of the average of the raw fitness  $f_{\text{avg}}$ . We will first try to find a linear relation so that the new maximum fitness  $f'_{\text{max}}$  is  $C_{\text{mult}}$  times the average fitness ( $f_{\text{avg}}$ ). We choose  $C_{\text{mult}} = 2$  as suggested by [Goldberg \(1989\)](#). This operation will scale early “super-individuals” down and the rest of the population up and preempts premature convergence. In the later phases of the [GA](#), when the fittest individuals and the bulk of the population have similar fitness values, this operation would lead to negative fitnesses for some individuals. In that case we find scaling parameters that maps the least fit individual to a fitness value of 0, while still maintaining  $f'_{\text{avg}} = f_{\text{avg}}$ . Once we have scaled the fitnesses we move to the selection process.

In the current version of the [DALEK code](#) we employ *elitism* (10% of fittest individual advance immediately to next generation). We have also experimented with other modifications to the mating population, but found them to be subpar. The mating pool we have chosen has only two slots. For now we select the individuals for the mating pool using the standard *roulette wheel selection*. We use a crossover probability of 90%, this means that in 10% of the cases we do not perform crossover but the child is a copy of the first parent. If crossover occurs, we perform a uniform crossover as we felt that we do not want the ordering of the parameters to matter. We have also experimented with arithmetic crossovers by taking the mean of parents. This meant that often useful traits would entirely disappear and we switched back to uniform crossovers. We will experiment in the near future with different crossover techniques like single-point crossovers. The new individual, created by crossover, is subjected to possible mutations before being placed into the new population. The [DALEK code](#) employs different mutation strategies for the different parameters. The abundances are just multiplied by a uniform random number (we have tried gaussian random numbers) with a relatively high chance of currently 7%. As luminosity and photospheric velocity are physically different we treat them differently to the abundances. In both cases we add a uniform random number, in addition to having different mutation probabilities. After the mutation step we see if the buffer element oxygen has a negative abundance. A negative abundance implies that the other elements add up to more than 1. If oxygen has positive abundance the code goes on to check the abundance ratios. If the child passes both these tests it is placed in the new population, if not it is discarded. This process is repeated until the size of the new population (including the members of the old population that advanced through *elitism*) reaches 150.

This process of selection, recombination and mutation is repeated over many generations. We have experimented with up to a 1000 populations in one run. Our scheduler can achieve a throughput of one generation per minute (in optimal conditions where all CPUs are free). Our principal spectrum for the testing was SN 2002bo 10.4 days post explosion (see Figure 5.1). In the presented case we let the **GA** run for 188 generations. Figure 5.11 shows how the genetic algorithm over many generations improves the fitness of the individuals.

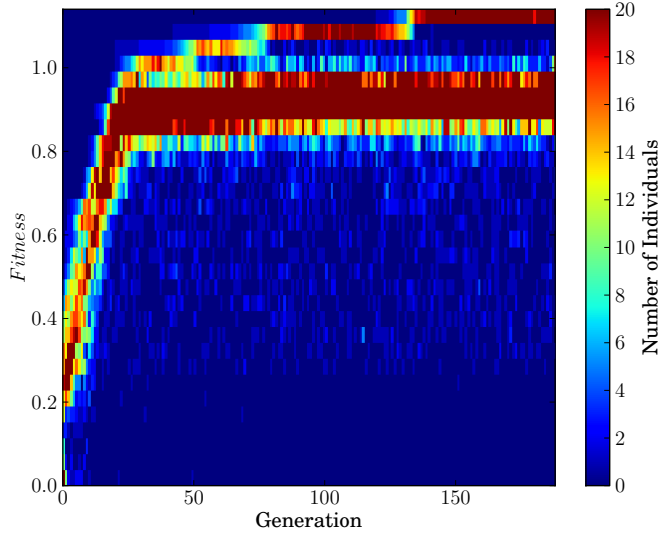


**Figure 5.11** Evolution of fitness of in the generations. In later generations there is a clear divide between the members that have advanced through elitism and the bulk of the population. This suggests a too high mutationrate or the convergence of the algorithm.

The step-pattern is very common in genetic algorithms: One individual has a favorable mutation and it takes several generations for the others to catch up. During the last generations one can clearly see that there is a gap between bulk of the population is and the top 10%. This gap is caused by the contrast of relatively high mutation in the main individuals against the mutation free advancement of the top 10% (*elitism*).

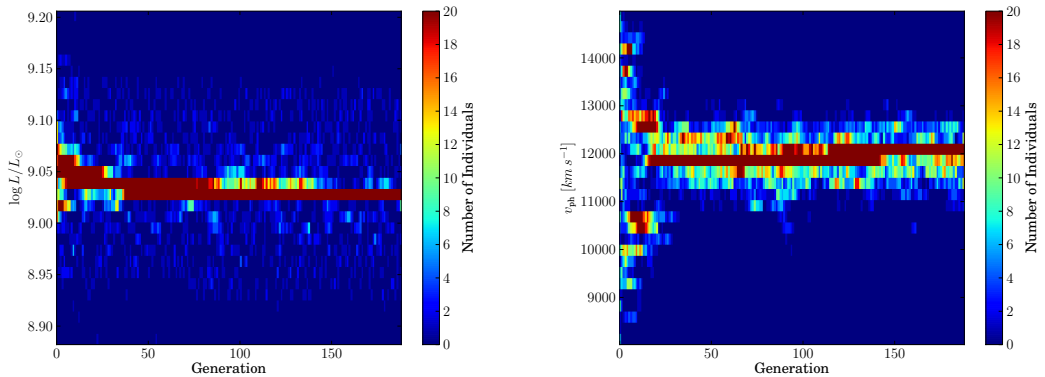


**Figure 5.12** The evolution of both luminosity and photospheric velocity shows that even at late phases of the algorithm there are still new combination that are being trialled. The very quick convergence in both cases however is a bit worrisome and will be analysed in future experiments.

Figure 5.12 gives a good overview of how the genetic algorithm process through the search space. In our example the algorithm converges relatively fast (after roughly 30 generations). Even though there is a “main”-population the algorithm still tries out different combinations. Currently we still have the problem that for certain initial random seeds the algorithm does not find the global optimum but converges prematurely on a local optimum. We believe the quick convergence seen in Figure 5.12 might be evidence for this. This again is an area of active research and two experts in evolutionary optimization joined our team recently to address this problem.

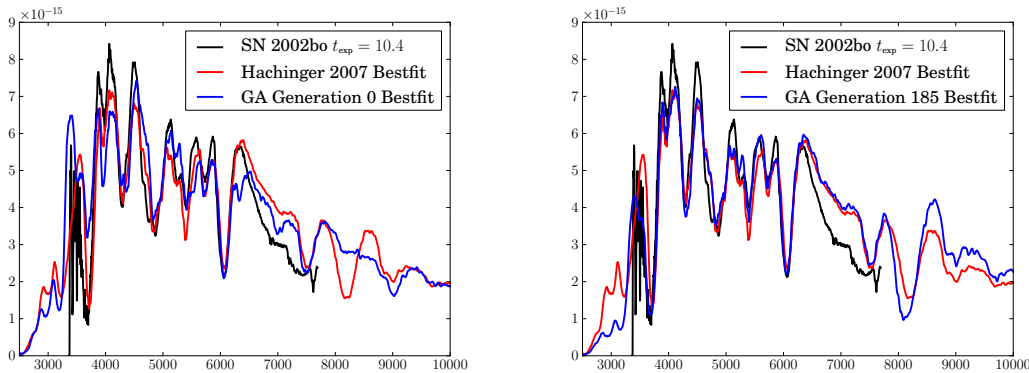


**Figure 5.13** The best individual of the first generation (left) and the best individual after 185 generations (right). This initial result demonstrates that GAs are able to conquer this problem. A more stable convergence and thorough exploration of the parameter space is however necessary to use this technique on a set of supernova spectra.

Although there are still many outstanding problems we can show that the GAs are able to solve the SNe Ia fitting problem. In Figure ?? we show the best fit in the first generation as well as the best-fit in the last generation. As comparison we show the best fit obtained by Hachinger (2007). The GA has been successful in reproducing the main features of the SNe Ia-spectrum. The de-weighting in the infrared is working very well. We are currently trialing the current code on different spectra with mixed results.

## 5.5. Conclusion

GAs are powerful tools, which can easily search a vast parameter space in parallel and avoid local optima. The intrinsic parallel structure has been a tremendous advantage in our experiments. We have shown that GAs can successfully solve the problem and fit a SNe Ia-spectrum. We do acknowledge that our current implementation does not reliably work on all spectra and there remains lots of fine-tuning work to be done. This tweaking is very common in GA implementations, but often requires experts in numerical optimization for speedy advancement. James Turner and Irene Mosner are experts in evolutionary optimization (their research focuses on differential evolutionary algorithms) and are currently exploring with our help the search space. On a different front we are currently exploring to optimize the exploration speed. Even on current high-end machines the MLMC takes one minute per synthetic spectrum per CPU. One of the ideas is creating a parameter grid around all or some of our search area. We could then use fast and efficient

interpolation techniques (one of these is described in Chapter ??) and explore different settings for our genetic algorithm much more quickly.

Over the course of this project we have realized that the field of numerical optimization has made huge strides in the last decades. Most of the new algorithms are not well known in astronomy and are used even rarer. On the other hand experts in the field of numerical optimization are often in desperate need for “real world” applications. They are more than willing to apply their knowledge to problems in our field. We strongly believe that there is an important ground for collaboration that would benefit both sides immensely.



# CHAPTER 6

---

## Conclusions and Future Work

A lot of the aspects of **SN Ia**physics have been solved. We are very certain that this phenomenon is powered by the nuclear burning of degenerate Carbon/Oxygen fuel. The lack of hydrogen in the spectra of **SNe Ia**suggests that the progenitors are white dwarfs as they do not posses an extensive hydrogen envelope. The question that remains is: How and why do these objects explode?

### 6.1. Single or Double Degenerate?

The initial idea for this thesis was simple: High resolution spectroscopy and high precision astrometry of close and young remnant should reveal the suggested donor star. At this time the only viable scenario was the SD-scenario. DD-scenarios were almost unanimously believed to lead to accretion induced collapse and not a **SN Ia**. The first project was to confirm Tycho-G as the progenitor of SN1572 and then move on and find the progenitors in both SN1006 and SN1604.

The observations however started to show a completely different picture. The very unusual kinematics claimed for Tycho-G([Ruiz-Lapuente et al., 2004](#)), was only slightly unusual. The Besançon model suggested the unusual velocity to be very usual if Tycho-G was an uninvolved background interloper (see Section [2.6.1](#)). We have realized that kinematics is definitely not conclusive evidence for a progenitor hunt, at most it is suggestive.

The SD-scenario in most cases suggests **RLOF** as the mass transfer. A consequence of this mass transfer mode is tidal coupling of the donor. Tidal coupling also implies that the rotation of the donor post-explosion is coupled to its escape velocity (see Section ?? and Figure [2.2](#)). For our search a serendipitous coincidence is that most low-mass stars do not rotate. Our work in Chapter ?? suggested that Tycho-Gdoes not have a unusually high rotation. Further work with better data (see Chapter [3](#)) established this. It is not entirely without caveats: the rotation might vanish post-explosion when the star puffs-up. In addition, the observable is not the rotation but the projected rotation, which is the intrinsic rotation diminished by a factor  $\sin i$ . Ironically, after the establishment of rotation as a donor star feature, we discovered a star with an unusually high rotation which was

kinematically very normal (see Chapter 3). No other stars in SN1572 and SN1006 (from preliminary analysis) show any unusually high rotation.

Finding donor stars seems much harder than we initially thought. Both SN1572 and SN1006 don't have any strong candidates. We do acknowledge unusual stars in these remnants, but all of them have believable alibis which do not involve a **SN Ia** explosion. Only one star in the well studied remnant of SN1572 has so far eluded our spectroscopic scrutiny. This star (Tycho-A2 by our nomenclature) has an unusual proper motion according to our HST astrometry (see 3.1). In addition it is located very close to the X-raycenter of SN1572. Unfortunately it hides 0.4'' away from the 4 magnitudes brighter Tycho-A (see Figure 6.1). This makes it impossible to obtain ground-based optical spectroscopy, but offers the possibility for challenging infrared observations aided by adaptive-optics. We are currently running a GNIRS-based campaign to obtain the fundamental stellar parameters, radial velocity and rotation.

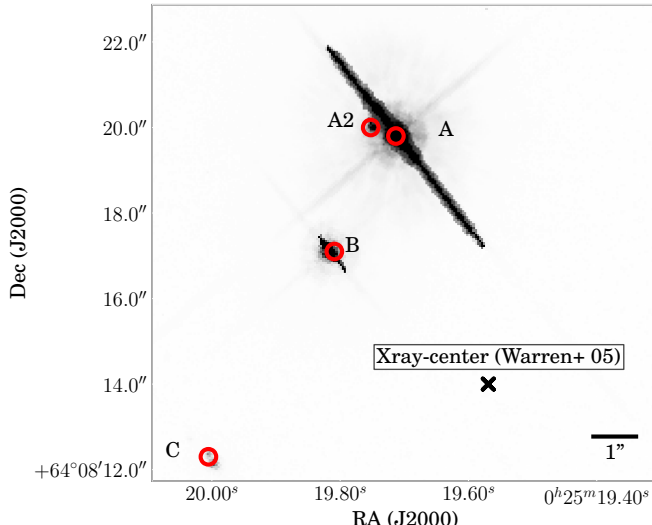


**Figure 6.1** Overview of inner region of the remnant of SN1572. All labelled stars except Star-A2 have existing high-resolution spectra. Tycho-A2 is located very close to Tycho-A (0.6''). Spectroscopy can only be obtained with adaptive optics in the infrared.

The bottom line for both SN1572 and SN1006 seems to be: No bright progenitors. There are as always caveats, but we do think that with current theoretical knowledge and current instrumentation it is not worthwhile to scrutinize these remnants further. The only exception is to undertake photometrically deep observations of these remnants and look for a hot white dwarf.

## 6.2. The curious case of Kepler

The last of the young remnants and the most distant one (? estimates a distance of  $\geq 6$  kpc). The morphology of this remnant is not as clean and spherical as for SN1006 and SN1572 (see Figure ??). For a long time SN1604 (Kepler's supernova) was also believed to be a **SN Ib**, but prominent iron emission in X-rayspectra (Reynolds et al., 2007) suggests this event

to be a **SN Ia**([Hughes et al., 1995](#)). SN1604 also shows an abundance in nitrogen which is unusual for a **SN Ia**. [Blair et al. \(1991\)](#) and [Sollerman et al. \(2003\)](#) suggest that the remnant itself posseses a very high systemic velocity of  $\approx 250 \text{ km s}^{-1}$ . A recent study by [Chiotellis et al. \(2011\)](#) suggests that a SD-scenario with an AGB star as a donor would explain all the observed peculiarities. They make the prediction that this star should be visible and very bright post-explosion.

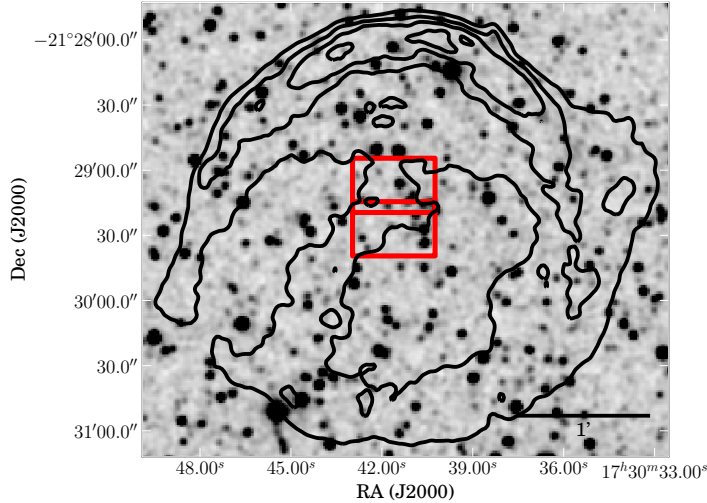


**Figure 6.2** VLA contours of Kepler's remnant (SN1604) overlaid on a 2MASS image. The red rectangle show the overlapping north and south field of our WiFeS observing campaign.

We have obtained data with the WiFeS integral field spectrograph. The field of view for this instrument. is rectangular with dimensions of  $25'' \times 38''$ . We have two overlapping fields that cover all stars at a projected velocity of  $1300 \text{ km s}^{-1}$ (assuming a distance of 6 kpc). Extracting stellar spectra from our poor seeing data ( $> 1.5''$ ) is technically challenging and we have not invested much time in this project.

### 6.3. Divide et impera

Maybe finding the progenitors of **SNe Ia** is too difficult using our current techniques. It might be much easier to employ the successful “Divide et Impera” - “Divide and Conquer” strategy. By asking many very small questions it might be easier to uncover on the truth than to try to solve this problem at once. We believe that one of these important questions is the mass at which **CO-WD** explode. There are currently two main scenarios. The favored scenario is the explosion of the **CO-WD** close to  $M_{\text{Chan}}$  ( $1.38 M_{\odot}$ ). As shown in Chapter 1 the burning of a  $1.38 M_{\odot}$ **CO-WD** only produces the right abundance pattern when introducing a delayed detonation. When exploding a  $1 M_{\odot}$ **CO-WD** this problem does not exist, a detonation of such a star produces the right optical photospheric spectrum. The main problem with these sub-Chandrasekhar mass explosions is that there exists no caveat free theory for the ignition yet. One key to find the explosion mass of any given **SN Ia** might be the abundance of stable in nebular spectra. In the Chandrasekhar mass case

there should be more stable iron, in the case of a sub-Chandrasekhar mass there should be less.

## 6.4. Dalek

The title of this thesis suggests that **SN Ia**-progenitors and their explosions are mutually exclusive fields of research. In the previous section we have however shown that the mass of the white dwarf does have an influence on the yield. This mass is again linked to different progenitor channels. The analysis of spectra might not only help us constrain the elemental yields and explosion energies, but also give us insight into the progenitors.

In Chapter 5 we describe a project to automate the analysis of **SN Ia**-spectra. The currently manual operated **MLMC**-code is ideal for automating as it strikes the right balance between speed and realism. We researched several numerical optimization strategies for this project before settling on **GAs**. For now we have successfully fitted only one supernova spectrum. We are currently fine-tuning the algorithm and have enlisted the help of experts in the **GA**-field.

## 6.5. Trouble in Paradise

During the work of this thesis the field of **SN Ia**-research has changed significantly. When we started the donor star search there seemed little doubt in the community about the SD-scenario. Over the recent years the SD-channel has been seriously shaken and there has been some newfound support for the DD-channel. The renaissance of the DD-scenario, however often comes from the face that the merging of two white dwarfs doesn't provide as strong predictions as the SD-scenario. This contention has reinvigorated the field of **SN Ia**-progenitors and makes it a challenging and intriguing area to work in.

New transient and all sky surveys will soon start drowning us in a deluge of data. Currently the astronomical community is ill equipped to deal with such large amounts of data. This is not surprising as most astronomers are experts in physics and not data processing. This problem is not unique to astronomy, more and more fields are gathering much more data than is ever processable by individuals. We believe this is a great opportunity to start cross-disciplinary research. The fundamentals of science (e.g. pattern recognition) are definitely not unique to individual areas. New areas of science like eScience are trying to provide techniques and tools for scientists irregardless of the field.

We have tried to conduct cross-disciplinary research in automatically fitting **SNe Ia**-spectra. Stephan Hachinger (the expert in manual fitting) and me initially have tried using the methods that were taught to us during our undergraduate years in physics (e.g. Newton-Raphson). These methods are still useful for very simple problems, however do not scale to today's highly non-linear problems with many co-dependant variables. Sam Inverso, a computer scientist working many in the area of neuro-science, joined us first and helped us do our first baby-steps in **GAs**. His help has advanced the **DALEK code** to its present state. In the last half year two new members have joined the team, whose research is in numerical optimization. They are very interested in applying their techniques to "real world" problems, which are scarce in the optimization community.

This work definitely tries to show: Multidisciplinary research is not only a buzzword, but can advance individual fields of science much faster than they could advance in isolation.



---

# Glossary

**[Fe/H]** iron abundance relative to the sun. 54, 56, 57, 66, 70, 87, 88, 108

**AGB** asymptotic giant branch. 28

**AM CVn** AM Canum Venaticorum star (white dwarf accreting hydrogen poor matter from a companion star; see Nelemans (2005)). 25, 28

**CO-WD** Carbon/Oxygen White Dwarf. 21–26, 90, 99

**CSI** circum-stellar interaction. 60

**CSM** circum-stellar medium. 7, 20, 27, 71

**DALEK code** Automatic SN Ia spectrum fitting code. 91, 92, 100

**DTD** delay time distribution. 10, 17, 28

$\log g$  surface gravity. 53, 54, 56, 57, 70, 87, 88, 108

**GA** genetic algorithm. 73, 82–85, 87–89, 91, 92, 94, 100

**GRB** gamma ray burst. 4, 5, 14

**IGE** iron group element. 12, 13, 21, 80, 81, 89

**IME** intermediate mass element. 12, 22

**ISM** inter-stellar medium. 12, 16, 17, 71

$L_{\text{bol}}$  bolometric luminosity. 76

**LMC** Large Magellanic Cloud. 16, 17

$M_{\text{Chan}}$  Chandrasekhar mass ( $1.38 M_{\odot}$ ; see Chandrasekhar (1931)). 21, 25, 26, 28, 99

**MLMC** Mazzali & Lucy SN Ia spectrum synthesis code. 73–76, 78, 81, 89–91, 94, 100

**NSE** nuclear statistical equilibrium. 22

**ONe-WD** Oxygen/Neon White Dwarf. 21, 26

**P Cygni** a hypergiant luminous blue variable with strong winds. often referred to as a description for line profiles. 12

**RLOF** Roche Lobe Overflow. 25–27, 97

**SN Ia** Type Ia supernova. 5–7, 9–17, 21–29, 47, 48, 60, 63, 71, 73, 74, 80, 89, 94, 97–100

**SN Ib** Type Ib supernova. 7, 98

**SN Ib/c** Type Ib/c supernova. 7, 9, 14, 16, 18

**SN II** Type II supernova. 6, 7, 9, 11, 13–16, 18–20, 63

**SN IIb** Type IIb supernova. 7

**SN III** Type III supernova. 7

**SN IIP** Type IIP supernova. 7, 15

**SNR** supernova remnant. 27, 28, 63

**SSS** supersoft X-Ray source. 25, 27

$t_{\text{exp}}$  time since explosion (measured in days). 78, 89

$T_{\text{eff}}$  effective temperature - Temperature of a blackbody emitting the same total energy..  
53, 54, 56, 57, 70, 76, 87, 88, 108

**TSP** Travelling Salesman Problem. 84

$v_{\text{ph}}$  photospheric velocity of a supernova. 76–78, 89, 90

---

## Bibliography

- Abramovici, A., et al. 1992, Science, 256, 325 ([ADS entry](#))
- Aldering, G., et al. 2002, in Presented at the Society of Photo-Optical Instrumentation Engineers (SPIE) Conference, Vol. 4836, Society of Photo-Optical Instrumentation Engineers (SPIE) Conference Series, ed. J. A. Tyson & S. Wolff, 61–72 ([ADS entry](#))
- Alekseev, E. N., Alekseeva, L. N., Krivosheina, I. V., & Volchenko, V. I. 1988, Phys. Lett., B205, 209
- Aller, L. H., et al. 1982, Landolt-Börnstein: Numerical Data and Functional Relationships in Science and Technology (Berlin: Springer) ([ADS entry](#))
- Altavilla, G., et al. 2004, MNRAS, 349, 1344 ([ADS entry](#))
- Anderson, J., & King, I. R. 2006, PSFs, Photometry, and Astronomy for the ACS/WFC, Tech. rep. ([ADS entry](#))
- Arnett, W. D. 1969, Ap&SS, 5, 180 ([ADS entry](#))
- . 1982, ApJ, 253, 785 ([ADS entry](#))
- Asplund, M., Grevesse, N., Sauval, A. J., & Scott, P. 2009, ARA&A, 47, 481 ([ADS entry](#))
- Baade, W. 1938, ApJ, 88, 285 ([ADS entry](#))
- Baade, W., & Zwicky, F. 1934, Proceedings of the National Academy of Science, 20, 254 ([ADS entry](#))
- Badenes, C., Borkowski, K. J., & Bravo, E. 2005, ApJ, 624, 198 ([ADS entry](#))
- Badenes, C., Borkowski, K. J., Hughes, J. P., Hwang, U., & Bravo, E. 2006, ApJ, 645, 1373 ([ADS entry](#))
- Badenes, C., Bravo, E., Borkowski, K. J., & Domínguez, I. 2003, ApJ, 593, 358 ([ADS entry](#))
- Barbary, K., et al. 2010, ArXiv e-prints ([ADS entry](#))

- Barber, C. B., Dobkin, D. P., & Huhdanpaa, H. 1996, ACM TRANSACTIONS ON MATHEMATICAL SOFTWARE, 22, 469
- Barbon, R., Ciatti, F., & Rosino, L. 1979, A&A, 72, 287 ([ADS entry](#))
- Baron, E., Bethe, H. A., Brown, G. E., Cooperstein, J., & Kahana, S. 1987, Physical Review Letters, 59, 736 ([ADS entry](#))
- Baron, E., Cooperstein, J., & Kahana, S. 1985, Physical Review Letters, 55, 126 ([ADS entry](#))
- Beals, C. S., & Blanchet, G. H. 1937, PASP, 49, 224 ([ADS entry](#))
- Benetti, S., et al. 2004, MNRAS, 348, 261 ([ADS entry](#))
- . 2005, ApJ, 623, 1011 ([ADS entry](#))
- Bessell, M. S. 2007, PASP, 119, 605 ([ADS entry](#))
- Bessell, M. S., Castelli, F., & Plez, B. 1998, A&A, 333, 231 ([ADS entry](#))
- Bianco, F. B., et al. 2011, ArXiv e-prints ([ADS entry](#))
- Bildsten, L., Shen, K. J., Weinberg, N. N., & Nelemans, G. 2007, ApJ, 662, L95 ([ADS entry](#))
- Bionta, R. M., Blewitt, G., Bratton, C. B., Casper, D., & Ciocio, A. 1987, Physical Review Letters, 58, 1494 ([ADS entry](#))
- Blair, W. P., Long, K. S., & Vancura, O. 1991, ApJ, 366, 484 ([ADS entry](#))
- Blake, C., et al. 2011, MNRAS, 951 ([ADS entry](#))
- Brahe, T., & Kepler, J. 1602, *Tychonis Brahe Astronomiae instauratae progymnasmata : quorum haec prima pars de restitutione motuum SOLIS et lunae stellarumque inerrantium tractat, et praeterea de admiranda nova stella anno 1572 exorta luculenter agit.*, ed. Brahe, T. & Kepler, J. ([ADS entry](#))
- Branch, D., Fisher, A., & Nugent, P. 1993, AJ, 106, 2383 ([ADS entry](#))
- Burrows, A., Livne, E., Dessart, L., Ott, C. D., & Murphy, J. 2007, ApJ, 655, 416 ([ADS entry](#))
- Caccin, B., Cavallini, F., Ceppatelli, G., Righini, A., & Sambuco, A. M. 1985, A&A, 149, 357 ([ADS entry](#))
- Canal, R., Méndez, J., & Ruiz-Lapuente, P. 2001, ApJ, 550, L53 ([ADS entry](#))
- Cannon, R., Hambly, N., & Zacharias, N. 2001, in Astronomical Society of the Pacific Conference Series, Vol. 232, *The New Era of Wide Field Astronomy*, ed. R. Clowes, A. Adamson, & G. Bromage, 311-- ([ADS entry](#))
- Cardelli, J. A., Clayton, G. C., & Mathis, J. S. 1989, ApJ, 345, 245 ([ADS entry](#))
- Cassam-Chenaï, G., Hughes, J. P., Ballet, J., & Decourchelle, A. 2007, ApJ, 665, 315 ([ADS entry](#))

- Castelli, F., & Kurucz, R. L. 2003, in IAU Symposium, Vol. 210, Modelling of Stellar Atmospheres, ed. N. Piskunov, W. W. Weiss, & D. F. Gray, 20P-+ ([ADS entry](#))
- Castelli, F., & Kurucz, R. L. 2004, ArXiv Astrophysics e-prints ([ADS entry](#))
- Chakraborty, U. K., & Janikow, C. Z. 2003, Information Sciences, 156, 253 , evolutionary Computation ([Link](#))
- Chandrasekhar, S. 1931, ApJ, 74, 81 ([ADS entry](#))
- Chiotellis, A., Schure, K. M., & Vink, J. 2011, ArXiv e-prints ([ADS entry](#))
- Colgate, S. A. 1974, ApJ, 187, 333 ([ADS entry](#))
- Colgate, S. A., Moore, E. P., & Carlson, R. 1975, PASP, 87, 565 ([ADS entry](#))
- Di Stefano, R. 2010, ApJ, 719, 474 ([ADS entry](#))
- Di Stefano, R., Kong, A., & Primini, F. A. 2006, ArXiv Astrophysics e-prints ([ADS entry](#))
- Di Stefano, R., Voss, R., & Claeys, J. S. W. 2011, ArXiv e-prints ([ADS entry](#))
- Dorigo, M., & Gambardella, L. M. 1997, Ant colonies for the travelling salesman problem
- Eggleton, P. P. 1983, ApJ, 268, 368 ([ADS entry](#))
- Einstein, A. 1918, Sitzungsberichte der Königlich Preußischen Akademie der Wissenschaften (Berlin), Seite 154-167., 154 ([ADS entry](#))
- Ensman, L., & Burrows, A. 1992, ApJ, 393, 742 ([ADS entry](#))
- Filippenko, A. V., Li, W. D., Treffers, R. R., & Modjaz, M. 2001, in Astronomical Society of the Pacific Conference Series, Vol. 246, IAU Colloq. 183: Small Telescope Astronomy on Global Scales, ed. B. Paczynski, W.-P. Chen, & C. Lemme, 121-+ ([ADS entry](#))
- Filippenko, A. V., et al. 1992, AJ, 104, 1543 ([ADS entry](#))
- Fink, M., Röpke, F. K., Hillebrandt, W., Seitenzahl, I. R., Sim, S. A., & Kromer, M. 2010, A&A, 514, A53+ ([ADS entry](#))
- Fisher, A. K. 2000, PhD thesis, THE UNIVERSITY OF OKLAHOMA ([ADS entry](#))
- Foley, R. J., et al. 2003, PASP, 115, 1220 ([ADS entry](#))
- Galama, T. J., et al. 1998, Nature, 395, 670 ([ADS entry](#))
- Garavini, G., et al. 2007, A&A, 471, 527 ([ADS entry](#))
- Garnavich, P. M., et al. 2002, in Bulletin of the American Astronomical Society, Vol. 34, American Astronomical Society Meeting Abstracts, 1233-+ ([ADS entry](#))
- Gaskell, C. M., Cappellaro, E., Dinerstein, H. L., Garnett, D. R., Harkness, R. P., & Wheeler, J. C. 1986, ApJ, 306, L77 ([ADS entry](#))
- Gerardy, C. L., et al. 2004, ApJ, 607, 391 ([ADS entry](#))

- Ghavamian, P., Raymond, J., Hartigan, P., & Blair, W. P. 2000, ApJ, 535, 266 ([ADS entry](#))
- Gilfanov, M., & Bogdán, Á. 2010, Nature, 463, 924 ([ADS entry](#))
- Goldberg, D. E. 1989, Genetic Algorithms in Search, Optimization, and Machine Learning, 1st edn. (Addison-Wesley Professional) ([Link](#))
- . 1990, Complex Systems, 5, 139
- Goldstein, B. R. 1965, AJ, 70, 105 ([ADS entry](#))
- Gooch, R. 1996, in Astronomical Society of the Pacific Conference Series, Vol. 101, Astronomical Data Analysis Software and Systems V, ed. G. H. Jacoby & J. Barnes, 80–+ ([ADS entry](#))
- Gray, D. F. 1977, ApJ, 211, 198 ([ADS entry](#))
- Gutiérrez, J., Canal, R., & García-Berro, E. 2005, A&A, 435, 231 ([ADS entry](#))
- Guy, J., et al. 2007, A&A, 466, 11 ([ADS entry](#))
- Hachinger, S. 2007, Master's thesis, TU München
- . 2011, PhD thesis, TU München
- Hachinger, S., Mazzali, P. A., Taubenberger, S., Pakmor, R., & Hillebrandt, W. 2009, MNRAS, 399, 1238 ([ADS entry](#))
- Hachisu, I., Kato, M., & Nomoto, K. 1996, ApJ, 470, L97 ([Link](#))
- Hachisu, I., Kato, M., & Nomoto, K. 1999b, ApJ, 522, 487 ([ADS entry](#))
- . 2008, ApJ, 683, L127 ([ADS entry](#))
- Hachisu, I., Kato, M., Nomoto, K., & Umeda, H. 1999a, ApJ, 519, 314 ([Link](#))
- Hamilton, A. J. S., & Fesen, R. A. 1988, ApJ, 327, 178 ([Link](#))
- Hamuy, M., et al. 1993, AJ, 106, 2392 ([ADS entry](#))
- Han, Z. 2008, accepted for publication in ApJL ([Link](#))
- Han, Z. 2008, ApJ, 677, L109 ([ADS entry](#))
- Han, Z., & Podsiadlowski, P. 2004, MNRAS, 350, 1301 ([Link](#))
- Hanbury Brown, R., & Hazard, C. 1952, Nature, 170, 364 ([ADS entry](#))
- Hancock, P., Gaensler, B. M., & Murphy, T. 2011, ArXiv e-prints ([ADS entry](#))
- Harkness, R. P., et al. 1987, ApJ, 317, 355 ([ADS entry](#))
- Hartwig, E. 1885, Astronomische Nachrichten, 112, 360 ([ADS entry](#))
- Hatano, K., Branch, D., Fisher, A., Baron, E., & Filippenko, A. V. 1999, ApJ, 525, 881 ([ADS entry](#))

- Hauschildt, P. H., & Baron, E. 1999, Journal of Computational and Applied Mathematics, 109, 41 ([ADS entry](#))
- Hayden, B. T., et al. 2010, ApJ, 722, 1691 ([ADS entry](#))
- Heiter, U., et al. 2002, A&A, 392, 619 ([ADS entry](#))
- Herbig, G. H. 1966, ZAp, 64, 512 ([ADS entry](#))
- Herbig, G. H. 1967, in IAU Symposium, Vol. 31, Radio Astronomy and the Galactic System, ed. H. van Woerden, 85— ([ADS entry](#))
- . 1975, ApJ, 196, 129 ([ADS entry](#))
- . 1995, ARA&A, 33, 19 ([ADS entry](#))
- Hernandez, J. I. G., Ruiz-Lapuente, P., Filippenko, A. V., Foley, R. J., Gal-Yam, A., & Simon, J. D. 2009, ApJ, 691, 1 ([ADS entry](#))
- Hibbins, R. E., Miles, J. R., Sarre, P. J., & Herbig, G. H. 1994, in The Diffuse Interstellar Bands, ed. A. G. G. M. Tielens, 31— ([ADS entry](#))
- Hillebrandt, W., & Niemeyer, J. C. 2000, ARA&A, 38, 191 ([ADS entry](#))
- Hirashita, H., Buat, V., & Inoue, A. K. 2003, A&A, 410, 83 ([ADS entry](#))
- Hirata, K., Kajita, T., Koshiba, M., Nakahata, M., & Oyama, Y. 1987, Physical Review Letters, 58, 1490 ([ADS entry](#))
- Holland, J. H. 1962, J. ACM, 9, 297 ([Link](#))
- . 1975, Adaptation in Natural and Artificial Systems (Ann Arbor, MI, USA: University of Michigan Press)
- Horne, K. 1986, PASP, 98, 609 ([ADS entry](#))
- Hubble, E. 1929, Proceedings of the National Academy of Science, 15, 168 ([ADS entry](#))
- Hughes, J. P. 2000, ApJ, 545, L53 ([ADS entry](#))
- Hughes, J. P., et al. 1995, ApJ, 444, L81 ([ADS entry](#))
- Iben, Jr., I., & Tutukov, A. V. 1984, ApJS, 54, 335 ([ADS entry](#))
- Iben, I. J. 1997, in NATO ASIC Proc. 486: Thermonuclear Supernovae, ed. P. Ruiz-Lapuente, R. Canal, & J. Isern (Dordrecht: Kluwer), 111 ([ADS entry](#))
- Ihara, Y., Ozaki, J., Doi, M., Shigeyama, T., Kashikawa, N., Komiyama, K., & Hattori, T. 2007, PASJ, 59, 811 ([ADS entry](#))
- Iliadis, C. 2007, Nuclear Physics of Stars, ed. Iliadis, C. (Wiley-VCH Verlag) ([ADS entry](#))
- Ilkov, M., & Soker, N. 2011, ArXiv e-prints ([ADS entry](#))
- Iwamoto, K., Brachwitz, F., Nomoto, K., Kishimoto, N., Umeda, H., Hix, W. R., & Thielemann, F.-K. 1999, ApJS, 125, 439 ([ADS entry](#))

- Jafry, Y. R., Cornelisse, J., & Reinhard, R. 1994, *ESA Journal*, 18, 219 ([ADS entry](#))
- James, F., & Roos, M. 1975, *Comput. Phys. Commun.*, 10, 343
- Janikow, C. Z., & Michalewicz, Z. 1991, in Proc. of the 4th International Conference on Genetic Algorithms, ed. R. K. Belew & L. B. Booker (Morgan Kaufmann), 151–157
- Jeffery, C. S., Woolf, V. M., & Pollacco, D. L. 2001, *A&A*, 376, 497 ([ADS entry](#))
- Jenniskens, P., & Desert, F. 1994, *A&AS*, 106, 39 ([ADS entry](#))
- Jha, S., Riess, A. G., & Kirshner, R. P. 2007, *ApJ*, 659, 122 ([ADS entry](#))
- Jones, E., Oliphant, T., Peterson, P., et al. 2001, SciPy: Open source scientific tools for Python ([Link](#))
- Justham, S. 2011, *ApJ*, 730, L34+ ([ADS entry](#))
- Justham, S., Wolf, C., Podsiadlowski, P., & Han, Z. 2008, submitted
- . 2009, *A&A*, 493, 1081 ([ADS entry](#))
- Kaiser, N. 2004, in Presented at the Society of Photo-Optical Instrumentation Engineers (SPIE) Conference, Vol. 5489, Society of Photo-Optical Instrumentation Engineers (SPIE) Conference Series, ed. J. M. Oschmann Jr., 11–22 ([ADS entry](#))
- Karle, A. 2008, in International Cosmic Ray Conference, Vol. 4, International Cosmic Ray Conference, 835–838 ([ADS entry](#))
- Kasen, D. 2006, *ApJ*, 649, 939 ([ADS entry](#))
- . 2010, *ApJ*, 708, 1025 ([ADS entry](#))
- Kasen, D., Röpke, F. K., & Woosley, S. E. 2009, *Nature*, 460, 869 ([ADS entry](#))
- Kasen, D., Thomas, R. C., & Nugent, P. 2006, *ApJ*, 651, 366 ([ADS entry](#))
- Keller, S. C., et al. 2007, *PASA*, 24, 1 ([ADS entry](#))
- Kepler, J. 1606, *De Stella nova in pede Serpentarii*
- Kepler, S. O., Kleinman, S. J., Nitta, A., Koester, D., Castanheira, B. G., Giovannini, O., Costa, A. F. M., & Althaus, L. 2007, *MNRAS*, 375, 1315 ([ADS entry](#))
- Kerzendorf, W. E., Schmidt, B. P., Asplund, M., Nomoto, K., Podsiadlowski, P., Frebel, A., Fesen, R. A., & Yong, D. 2009, *ApJ*, 701, 1665 ([ADS entry](#))
- Kirkpatrick, S., Gelatt, C. D., & Vecchi, M. P. 1983, *Science*, 220, 671 ([Link](#))
- Kirshner, R. P., & Kwan, J. 1974, *ApJ*, 193, 27 ([ADS entry](#))
- Klein, R. I., & Chevalier, R. A. 1978, *ApJ*, 223, L109 ([ADS entry](#))
- Kobayashi, C., Umeda, H., Nomoto, K., Tominaga, N., & Ohkubo, T. 2006, *ApJ*, 653, 1145 ([ADS entry](#))

- Konak, A., Coit, D. W., & Smith, A. E. 2006, Reliability Engineering & System Safety, 91, 992 ([Link](#))
- Kowal, C. T. 1968, AJ, 73, 1021 ([ADS entry](#))
- Krause, O., Tanaka, M., Usuda, T., Hattori, T., Goto, M., Birkmann, S., & Nomoto, K. 2008, Nature, 456, 617 ([ADS entry](#))
- Kromer, M., & Sim, S. A. 2009, MNRAS, 398, 1809 ([ADS entry](#))
- Kupka, F. G., Ryabchikova, T. A., Piskunov, N. E., Stempels, H. C., & Weiss, W. W. 2000, Baltic Astronomy, 9, 590 ([ADS entry](#))
- Kurucz, R., & Bell, B. 1995, Atomic Line Data (R.L. Kurucz and B. Bell) Kurucz CD-ROM No. 23. Cambridge, Mass.: Smithsonian Astrophysical Observatory, 1995., 23 ([ADS entry](#))
- Leonard, D. C. 2007, ApJ, 670, 1275 ([ADS entry](#))
- Lesaffre, P., Podsiadlowski, P., & Tout, C. A. 2005, Nuclear Physics A, 758, 463 ([ADS entry](#))
- Li, W., et al. 2003, PASP, 115, 453 ([ADS entry](#))
- . 2011, MNRAS, 412, 1441 ([ADS entry](#))
- Li, X.-D., & van den Heuvel, E. P. J. 1997, A&A, 322, L9 ([Link](#))
- Livne, E., & Arnett, D. 1995, ApJ, 452, 62 ([ADS entry](#))
- Maeda, K., Taubenberger, S., Sollerman, J., Mazzali, P. A., Leloudas, G., Nomoto, K., & Motohara, K. 2010, ApJ, 708, 1703 ([ADS entry](#))
- Mannucci, F., Della Valle, M., & Panagia, N. 2006, MNRAS, 370, 773 ([ADS entry](#))
- Mannucci, F., Della Valle, M., Panagia, N., Cappellaro, E., Cresci, G., Maiolino, R., Petrosian, A., & Turatto, M. 2005, A&A, 433, 807 ([ADS entry](#))
- Maoz, D., & Badenes, C. 2010, MNRAS, 407, 1314 ([ADS entry](#))
- Maoz, D., Sharon, K., & Gal-Yam, A. 2010, ApJ, 722, 1879 ([ADS entry](#))
- Marietta, E., Burrows, A., & Fryxell, B. 2000, ApJS, 128, 615 ([ADS entry](#))
- Matheson, T., Filippenko, A. V., Ho, L. C., Barth, A. J., & Leonard, D. C. 2000, AJ, 120, 1499 ([ADS entry](#))
- Mazzali, P. A. 2000, A&A, 363, 705 ([ADS entry](#))
- Mazzali, P. A., & Lucy, L. B. 1993, A&A, 279, 447 ([ADS entry](#))
- Mazzali, P. A., Röpke, F. K., Benetti, S., & Hillebrandt, W. 2007, Science, 315, 825 ([ADS entry](#))
- Mazzali, P. A., Sauer, D. N., Pastorello, A., Benetti, S., & Hillebrandt, W. 2008, MNRAS, 386, 1897 ([ADS entry](#))

- Mazzali, P. A., et al. 2005, ApJ, 623, L37 ([ADS entry](#))
- Meegan, C. A., Fishman, G. J., Wilson, R. B., Horack, J. M., Brock, M. N., Paciesas, W. S., Pendleton, G. N., & Kouveliotou, C. 1992, Nature, 355, 143 ([ADS entry](#))
- Meikle, W. P. S. 2000, MNRAS, 314, 782 ([ADS entry](#))
- Mennekens, N., Vanbeveren, D., De Greve, J. P., & De Donder, E. 2010, A&A, 515, A89+ ([ADS entry](#))
- Michalewicz, Z. 1994, Genetic algorithms + data structures = evolution programs (2nd, extended ed.) (New York, NY, USA: Springer-Verlag New York, Inc.)
- Minkowski, R. 1941, PASP, 53, 224 ([ADS entry](#))
- Modjaz, M., et al. 2009, ApJ, 702, 226 ([ADS entry](#))
- Munari, U., Sordo, R., Castelli, F., & Zwitter, T. 2005, A&A, 442, 1127 ([ADS entry](#))
- Nelemans, G. 2005, in Astronomical Society of the Pacific Conference Series, Vol. 330, The Astrophysics of Cataclysmic Variables and Related Objects, ed. J.-M. Hameury & J.-P. Lasota, 27–+ ([ADS entry](#))
- Noguchi, K., Ando, H., Izumiura, H., Kawanomoto, S., Tanaka, W., & Aoki, W. 1998, in Proc. SPIE, Optical Astronomical Instrumentation, ed. S. D'Odorico, Vol. 3355, 354 ([ADS entry](#))
- Nomoto, K. 1982, ApJ, 253, 798 ([Link](#))
- Nomoto, K., & Kondo, Y. 1991, ApJ, 367, L19 ([ADS entry](#))
- Nomoto, K., Saio, H., Kato, M., & Hachisu, I. 2007, ApJ, 663, 1269 ([Link](#))
- Nomoto, K., Thielemann, F.-K., & Yokoi, K. 1984, ApJ, 286, 644 ([ADS entry](#))
- Nugent, P., Phillips, M., Baron, E., Branch, D., & Hauschildt, P. 1995, ApJ, 455, L147+ ([ADS entry](#))
- Nugent, P., et al. 2006, ApJ, 645, 841 ([ADS entry](#))
- Oke, J. B., Cohen, J. G., Carr, M., et al. 1995, PASP, 107, 375 ([ADS entry](#))
- Ozaki, J., & Shigeyama, T. 2006, ApJ, 644, 954 ([Link](#))
- Pain, R., & SNLS Collaboration. 2003, in Bulletin of the American Astronomical Society, Vol. 35, American Astronomical Society Meeting Abstracts, 1335–+ ([ADS entry](#))
- Pakmor, R., Kromer, M., Röpke, F. K., Sim, S. A., Ruiter, A. J., & Hillebrandt, W. 2010, Nature, 463, 61 ([ADS entry](#))
- Pakmor, R., Röpke, F. K., Weiss, A., & Hillebrandt, W. 2008, A&A, 489, 943 ([ADS entry](#))
- Patat, F., Chugai, N. N., Podsiadlowski, P., Mason, E., Melo, C., & Pasquini, L. 2011, A&A, 530, A63+ ([ADS entry](#))

- Patat, F., et al. 2007, *Science*, 317, 924 ([ADS entry](#))
- Perlmutter, S., et al. 1999, *ApJ*, 517, 565 ([ADS entry](#))
- Perryman, M. A. C., et al. 2001, *A&A*, 369, 339 ([ADS entry](#))
- Phillips, M. M. 1993, *ApJ*, 413, L105 ([ADS entry](#))
- Phillips, M. M., Wells, L. A., Suntzeff, N. B., Hamuy, M., Leibundgut, B., Kirshner, R. P., & Foltz, C. B. 1992, *AJ*, 103, 1632 ([ADS entry](#))
- Pietrinferni, A., Cassisi, S., Salaris, M., & Castelli, F. 2004, *ApJ*, 612, 168 ([ADS entry](#))
- Pinto, P. A., et al. 2006, in *Bulletin of the American Astronomical Society*, Vol. 38, American Astronomical Society Meeting Abstracts, 1017–+ ([ADS entry](#))
- Podsiadlowski, P. 2003 ([ADS entry](#))
- Podsiadlowski, P., Joss, P. C., & Hsu, J. J. L. 1992, *ApJ*, 391, 246 ([ADS entry](#))
- Quimby, R., Höflich, P., Kannappan, S. J., Rykoff, E., Rujopakarn, W., Akerlof, C. W., Gerardy, C. L., & Wheeler, J. C. 2006, *ApJ*, 636, 400 ([ADS entry](#))
- Ramírez, S. V., & Cohen, J. G. 2002, *AJ*, 123, 3277 ([ADS entry](#))
- Rau, A., et al. 2009, *PASP*, 121, 1334 ([ADS entry](#))
- Reddy, B. E., Tomkin, J., Lambert, D. L., & Allende Prieto, C. 2003, *MNRAS*, 340, 304 ([ADS entry](#))
- Rest, A., et al. 2005, *Nature*, 438, 1132 ([ADS entry](#))
- . 2008, *ApJ*, 680, 1137 ([ADS entry](#))
- . 2011, *ApJ*, 732, 3 ([ADS entry](#))
- Reynolds, S. P., Borkowski, K. J., Hwang, U., Hughes, J. P., Badenes, C., Laming, J. M., & Blondin, J. M. 2007, *ApJ*, 668, L135 ([ADS entry](#))
- Reynoso, E. M., Moffett, D. A., Goss, W. M., Dubner, G. M., Dickel, J. R., Reynolds, S. P., & Giacani, E. B. 1997, *ApJ*, 491, 816 ([ADS entry](#))
- Riess, A. G., Press, W. H., & Kirshner, R. P. 1995, *ApJ*, 438, L17 ([ADS entry](#))
- Riess, A. G., et al. 1998, *AJ*, 116, 1009 ([ADS entry](#))
- . 1999, *AJ*, 118, 2675 ([ADS entry](#))
- Robin, A. C., Reylé, C., Derrière, S., & Picaud, S. 2003, *A&A*, 409, 523 ([ADS entry](#))
- Röpke, F. K., & Bruckschen, R. 2008, *New Journal of Physics*, 10, 125009 ([ADS entry](#))
- Röpke, F. K., & Hillebrandt, W. 2005, *A&A*, 431, 635 ([ADS entry](#))
- Rudolph, G. 1994, *Neural Networks, IEEE Transactions on*, 5, 96 ([Link](#))

- Ruiter, A. J., Belczynski, K., & Fryer, C. 2009, ApJ, 699, 2026 ([ADS entry](#))
- Ruiz-Lapuente, P. 2004, ApJ, 612, 357 ([ADS entry](#))
- Ruiz-Lapuente, P., et al. 2004, Nature, 431, 1069 ([ADS entry](#))
- Saio, H., & Nomoto, K. 1985, A&A, 150, L21 ([ADS entry](#))
- Schlegel, E. M. 1990, MNRAS, 244, 269 ([ADS entry](#))
- Schmidt, B. P., Kirshner, R. P., Leibundgut, B., Wells, L. A., Porter, A. C., Ruiz-Lapuente, P., Challis, P., & Filippenko, A. V. 1994, ApJ, 434, L19 ([ADS entry](#))
- Schmidt, B. P., et al. 1998, ApJ, 507, 46 ([ADS entry](#))
- Schweizer, F., & Middleditch, J. 1980, ApJ, 241, 1039 ([ADS entry](#))
- Shigeyama, T., Nomoto, K., Yamaoka, H., & Thielemann, F.-K. 1992, ApJ, 386, L13 ([ADS entry](#))
- Sim, S. A., Röpke, F. K., Hillebrandt, W., Kromer, M., Pakmor, R., Fink, M., Ruiter, A. J., & Seitenzahl, I. R. 2010, ApJ, 714, L52 ([ADS entry](#))
- Skrutskie, M. F., et al. 2006, ApJ, 131, 1163 ([ADS entry](#))
- Smartt, S. J. 2009, ARA&A, 47, 63 ([ADS entry](#))
- Sneden, C. 1973, ApJ, 184, 839 ([ADS entry](#))
- Soderberg, A. M., Nakar, E., Berger, E., & Kulkarni, S. R. 2006, ApJ, 638, 930 ([ADS entry](#))
- Soderberg, A. M., et al. 2008, Nature, 453, 469 ([ADS entry](#))
- Sollerman, J., Ghavamian, P., Lundqvist, P., & Smith, R. C. 2003, A&A, 407, 249 ([ADS entry](#))
- Sorokina, E. I., Blinnikov, S. I., Kosenko, D. I., & Lundqvist, P. 2004, Astronomy Letters, 30, 737 ([ADS entry](#))
- Staelin, D. H., & Reifenstein, III, E. C. 1968, Science, 162, 1481 ([ADS entry](#))
- Stehle, M., Mazzali, P. A., Benetti, S., & Hillebrandt, W. 2005, MNRAS, 360, 1231 ([ADS entry](#))
- Strøger, L.-G., et al. 2004, ApJ, 613, 200 ([ADS entry](#))
- Tammann, G. A., Loeffler, W., & Schroeder, A. 1994, ApJS, 92, 487 ([ADS entry](#))
- Tanaka, M., Mazzali, P. A., Maeda, K., & Nomoto, K. 2006, ApJ, 645, 470 ([ADS entry](#))
- Tanaka, M., Mazzali, P. A., Stanishev, V., Maurer, I., Kerzendorf, W. E., & Nomoto, K. 2011, MNRAS, 410, 1725 ([ADS entry](#))
- Thomas, R. C., Branch, D., Baron, E., Nomoto, K., Li, W., & Filippenko, A. V. 2004, ApJ, 601, 1019 ([ADS entry](#))
- Tonry, J., & Davis, M. 1979, AJ, 84, 1511 ([ADS entry](#))

- Totani, T., Morokuma, T., Oda, T., Doi, M., & Yasuda, N. 2008, PASJ, 60, 1327 ([ADS entry](#))
- Tucker, B. E. 2011, Ap&SS, 40 ([ADS entry](#))
- Turatto, M. 2003, in Lecture Notes in Physics, Berlin Springer Verlag, Vol. 598, Supernovae and Gamma-Ray Bursters, ed. K. Weiler, 21–36 ([ADS entry](#))
- Turatto, M., Benetti, S., & Pastorello, A. 2007, in American Institute of Physics Conference Series, Vol. 937, Supernova 1987A: 20 Years After: Supernovae and Gamma-Ray Bursters, ed. S. Immler, K. Weiler, & R. McCray, 187–197 ([ADS entry](#))
- van den Bergh, S. 1960, ZAp, 49, 201 ([ADS entry](#))
- van den Bergh, S., & Tammann, G. A. 1991, ARA&A, 29, 363 ([ADS entry](#))
- van den Heuvel, E. P. J., Bhattacharya, D., Nomoto, K., & Rappaport, S. A. 1992, A&A, 262, 97 ([ADS entry](#))
- van Dyk, S. D., Treffers, R. R., Richmond, M. W., Filippenko, A. V., & Paik, Y. 1994, in Bulletin of the American Astronomical Society, Vol. 26, American Astronomical Society Meeting Abstracts, 1444–+ ([ADS entry](#))
- van Kerkwijk, M. H., Chang, P., & Justham, S. 2010, ApJ, 722, L157 ([ADS entry](#))
- Vogt, F., & Wagner, A. 2011, Astrophysics and Space Science, submitted.
- Vogt, S. S., et al. 1994, in Presented at the Society of Photo-Optical Instrumentation Engineers (SPIE) Conference, Vol. 2198, Society of Photo-Optical Instrumentation Engineers (SPIE) Conference Series, ed. D. L. Crawford & E. R. Craine, 362–+ ([ADS entry](#))
- Voss, R., & Nelemans, G. 2008, Nature, 451, 802 ([ADS entry](#))
- Walborn, N. R., Prevot, M. L., Prevot, L., Wamsteker, W., Gonzalez, R., Gilmozzi, R., & Fitzpatrick, E. L. 1989, A&A, 219, 229 ([ADS entry](#))
- Warren, J. S., et al. 2005, ApJ, 634, 376 ([ADS entry](#))
- Weaver, T. A., Zimmerman, G. B., & Woosley, S. E. 1978, ApJ, 225, 1021 ([ADS entry](#))
- Webbink, R. F. 1984, ApJ, 277, 355 ([ADS entry](#))
- Wehrse, R. 1974, A list of all Fraunhofer lines of the Rowland tables arranged by elements (Heidelberg: Universität) ([ADS entry](#))
- Welch, P. 1967, IEEE Transactions on Audio and Electroacoustics, 15, 70 ([Link](#))
- Whelan, J., & Iben, Jr., I. 1973, ApJ, 186, 1007 ([ADS entry](#))
- Whitley, D. 1994, Statistics and Computing, 4, 65
- Wilson, R. 1958, ApJ, 128, 57 ([ADS entry](#))
- Winkler, P. F., Gupta, G., & Long, K. S. 2003, ApJ, 585, 324 ([ADS entry](#))
- Winkler, P. F., Long, K. S., Hamilton, A. J. S., & Fesen, R. A. 2005, ApJ, 624, 189 ([ADS entry](#))

- Wood-Vasey, W. M., et al. 2008, ApJ, 689, 377 ([ADS entry](#))
- Woosley, S. E., Heger, A., & Weaver, T. A. 2002, Reviews of Modern Physics, 74, 1015 ([ADS entry](#))
- Wright, A. H. 1991, in Foundations of Genetic Algorithms (Morgan Kaufmann), 205–218
- Wu, C.-C., Crenshaw, D. M., Fesen, R. A., Hamilton, A. J. S., & Sarazin, C. L. 1993, ApJ, 416, 247 ([ADS entry](#))
- Wu, C.-C., Crenshaw, D. M., Hamilton, A. J. S., Fesen, R. A., Leventhal, M., & Sarazin, C. L. 1997, ApJ, 477, L53+ ([ADS entry](#))
- Wu, C.-C., Leventhal, M., Sarazin, C. L., & Gull, T. R. 1983, ApJ, 269, L5 ([ADS entry](#))
- Yong, D., Lambert, D. L., Paulson, D. B., & Carney, B. W. 2008, ApJ, 673, 854 ([ADS entry](#))
- Yoon, S.-C., & Langer, N. 2004, A&A, 419, 623 ([ADS entry](#))
- Yu, S., & Jeffery, C. S. 2010, A&A, 521, A85+ ([ADS entry](#))
- Zhang, B., Dai, X., Lloyd-Ronning, N. M., & Mészáros, P. 2004, ApJ, 601, L119 ([ADS entry](#))
- Zhao, F., Strom, R. G., & Jiang, S. 2006, Chinese J. Astron. Astrophys., 6, 635 ([ADS entry](#))
- Zwicky, F. 1938, ApJ, 88, 529 ([ADS entry](#))
- . 1940, Reviews of Modern Physics, 12, 66 ([ADS entry](#))

## APPENDIX A

---

### Linear interpolation in N Dimensions

INTERPOLATION is one of the most common operations in astronomy. Resampling spectra to a different wavelength grid, projecting images or interpolating physical quantities in N-dimensional fluid dynamics simulation are all examples of interpolation. Interpolation can be described as a special case of curve fitting which requires the function to go through all points.

In one dimension interpolation is relatively easy and there exist multiple methods. The simplest method is nearest-neighbour interpolation in which the algorithm picks the closest neighbour point to the point to be interpolated.

Linear interpolation is one of the most common methods of interpolation. The two neighbouring points of the point to be interpolated are found and their slope and offset is used to obtain the interpolated point.

A more sophisticated approach is the spline-method of interpolation. Splines are piecewise polynomials of n-th degree whose first and second derivation are the same at the data points.

In one dimensional space there exists an abundance of interpolation methods. This multitude of options decreases rapidly with increasing number of dimensions. We will focus on the implementation of linear interpolation in N-dimensions, although there are a few other options like nearest neighbour interpolation and radial basis function.

For our linear interpolation we have opted to use Delauney Triangulation as a interpolation method.

The interpolation involves multiple steps to arrive at an interpolation solution: At first a Delauney Triangulation is performed on the existing points. As a next step we need to find the simplex (geometric structure; a triangle in two dimensions) that contains the point to be interpolated. Finally we will use the barycentric coordinate system of the simplex to perform the actual interpolation.

## A.1. Delauney triangulation

A triangulation is the process of connecting all points in a set with straight lines without any two lines crossing (see Figure A.1). It is obvious that there many ways for a set to be triangulated. All triangulations however have the same outer boundary called the convex hull. One special kind of triangulation is the Delauney Triangulation. The Delauney Triangulation can be defined a various abstract ways and has intriguing properties.

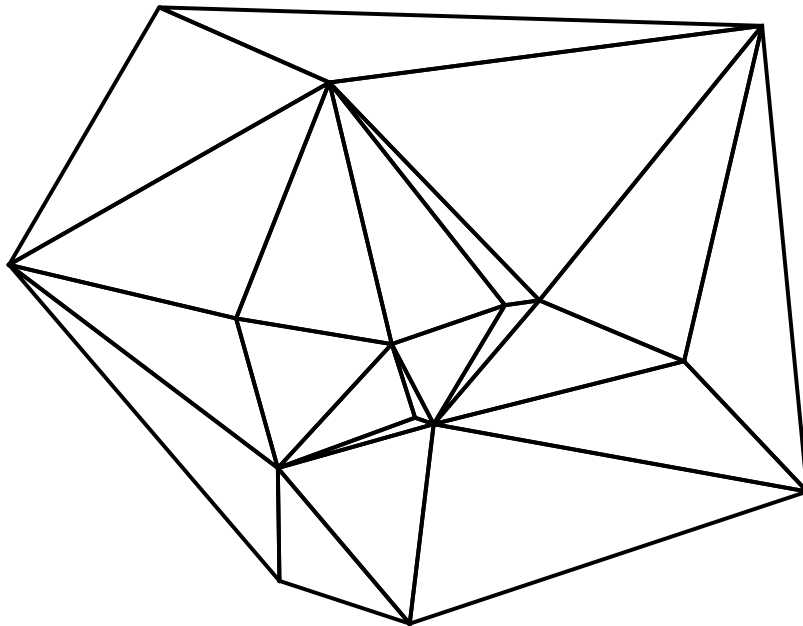


**Figure A.1** Delauney Triangulation of 20 points in two dimensions.

For a description of the process we will limit ourselves to two dimensions. This process is expandable to  $n$  dimensions in which the triangles become geometric structures called  $n$ -simplices. One such defintion is that the circum-circle of each triangle must only contain three points. Figure A.2, a simple example, shows one *legal* triangulation and one *illegal* triangulation. One can see in the *illegal* triangulation that the circum-circles of both triangles contain more than tree points. By doing a simple "edge-flip" one arrives at the Delauney Triangulation. In addition this ensures that the triangulation gives the largest minimum angle for both triangles.

Delauney Triangulation and convex hulls have a very interesting relation. It is possible construct the Delauney Triangulation in  $n$  dimensions from a convex hull of the points projected on paraboloid in  $n+1$  dimensions. Figure A.3 shows an example of a Delauney Triangulation in two dimensions constructed from the convex hull in three dimensions. To project the points onto the paraboloid one just square sums the coordinates  $n$  dimensions

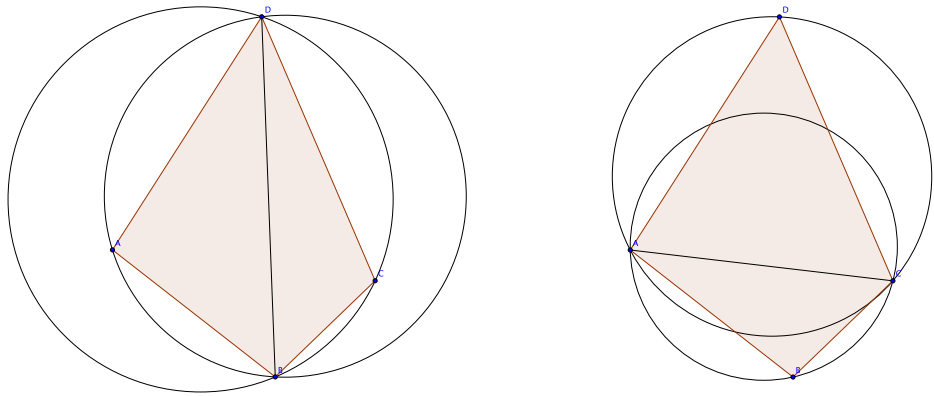


**Figure A.2** The left figure shows an "illegal" triangulation of the 4 points. Both circles include all the points. With a so called edge flip one can arrive at a "legal" triangulation.

and uses this as the coordinate for the point in  $n+1$  dimensions.

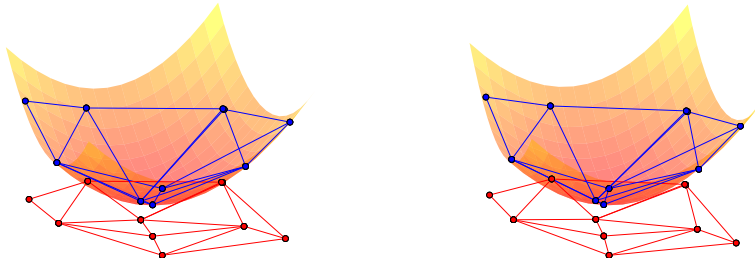
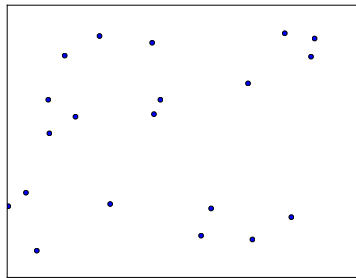


**Figure A.3** Stereogram (produced using a method described in [Vogt & Wagner, 2011](#)) of the projection of the convex hull in three dimensions to form the delauney triangulation in two dimensions.

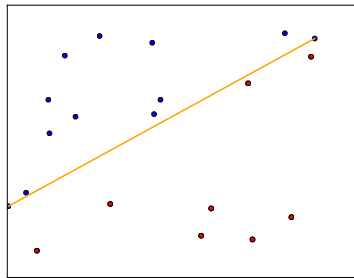
## A.2. Convex Hull

In section A.1 we have described the relation between the convex hull and the Delaunay Triangulation. There are multiple ways to construct the convex hull for  $N$  points, we will limit ourselves to the description of the Quickhull algorithm. Similar to the Quicksort algorithm it follows the divide and conquer method.

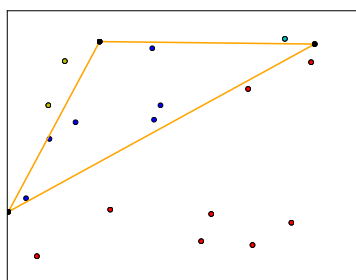
As an initial input we have  $N$  data points. Although this method works in  $n$ -dimensions,



**(a)** Twenty points for which we are trying to find the convex hull.



**(b)** We find the points with the lowest and highest x-value and connect them with a line.



**(c)** Continuing with the points on the left (same process happens recursively on the right) we find the point furthest away from the line. We then draw two more lines and build a triangle. The points inside of the triangle are not part of the convex hull and are discarded. We will repeat the current step with the two new lines of the triangle.

**(d)** We have found points of the convex hull once we can't build a new triangle anymore.

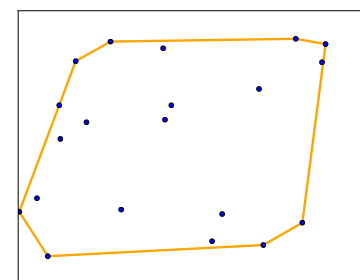


**Figure A.4** Determination of a convex hull in two dimensions.

we will show an example in two dimensions. The first operation is finding the two extreme points in the horizontal axis, which are guaranteed to be part of the convex hull. We connect these two extreme points thus creating a division between a “left” and a “right” set of point. Now the divide and conquer method begins. We will only describe what happens to the left side, but imply that the same steps are taken on the right side. We find the point furthest away from the dividing line and add it. A triangle is formed out of the two points of the initial dividing line and the additional point. All points inside the triangle do not belong to the convex hull and thus we exclude them. The triangle again divides the remaining points into two sets, one left of the triangle and one right which are again iterated over recursively.

The method is repeated until each subset only contains the start and end point of the dividing line. We have created the convex hull, which if projected to a  $d - 1$ -dimensional space provides the Delaunay Triangulation of the projected points. For this projection to work we need to construct a convex hull in more than two dimensions which uses the same technique as described.

### A.3. Barycentric coordinates system

The actual interpolation transforms the interpolant's coordinate into the barycentric coordinates of the containing triangle.

One can construct the barycenter of a triangle by drawing lines from each point to the midpoint of the opposing side (see Figure A.5).

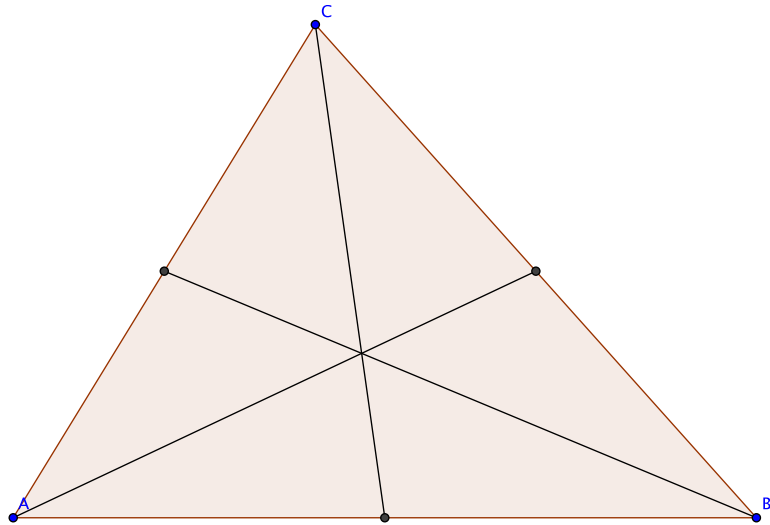


**Figure A.5** The triangle and its barycenter marked by the intersection of lines.

The coordinates of the barycenter M can simply be expressed by,

$$\vec{M} = \frac{1}{3}(\vec{A} + \vec{B} + \vec{C}).$$

Not only the barycenter can be expressed by the vectors of  $\vec{A}$ ,  $\vec{B}$  and  $\vec{C}$  but every point p inside the triangle can be expressed by,

$$\vec{p} = \alpha\vec{A} + \beta\vec{B} + \gamma\vec{C},$$

where

$$\alpha + \beta + \gamma = 1.$$

$\alpha$ ,  $\beta$  and  $\gamma$  are called the barycentric coordinates. If the point p lies within the triangle all barycentric coordinates are positive.

### A.4. Triangle Finding and Interpolation

To calculate the interpolation using barycentric coordinates we need to find the n-simplex that contains the interpolant. We use a method called directed walk (priv. comm. Pauli Virtanen). We choose a random starting n-simplex. In order to interpolate to a given point (interpolant) we calculate the barycentric coordinates for the interpolant and test if all of them are larger than 0. In that case we have found the n-simplex that contains the point. If

the n-th barycentric coordinate is negative we jump to the neighbouring n-simplex which is opposite the n-th point. This is iterated until the containing n-simplex is found or the next jump would lead outside the convex hull of the Delauney Triangulation. For the latter case the point is outside of the grid and can not be interpolated.

If this algorithm converges and the right n-simplex is found the interpolation can be easily performed using the barycentric coordinates:

$$f(\vec{p}) = \alpha f(\vec{A}) + \beta f(\vec{B}) + \gamma f(\vec{C})$$

where  $\vec{A}$ ,  $\vec{B}$  and  $\vec{C}$  are the points of the triangle.

## A.5. Conclusion

We have described the method of linear interpolation using Delauney Triangulation mainly in two dimensions. As mentioned this method is easily extensible to n dimensions. The triangles (3-simplices) become n-simplices in n dimensions (e.g. Tetrahedrons in three dimensions). The method itself however stays very similar for higher dimensions.

In this work we have made extensive use of n-dimensional linear interpolation using the implementation present in the *SciPy*-package ([Jones et al., 2001](#)), called LinearNDInterpolator. In this case creation of the convex-hull is performed by the QHULL implementation described in [Barber et al. \(1996\)](#).

We have tested the performance of the algorithm by creating a three dimensional grid with  $20 \times 10 \times 10$  gridpoints and an array of 10,000 double values at each gridpoint. On a standard 2011 MacBook Pro we have measured the initial building of the Delauney Triangulation and storing it in an appropriate data structure to 256 ms. The interpolation for random points took on average  $601 \mu\text{s}$ . This technique lends itself very well to explore large datasets even on moderately equipped machines.

We have used this technique extensively to interpolate a spectral grid in three dimension ( $T_{\text{eff}}$ ,  $\log g$  and  $[\text{Fe}/\text{H}]$ ). When trying to extract stellar parameters from an input spectrum we calculated the  $\chi^2$  for the observed spectrum with interpolated synthetic spectra from the grid. The interpolated spectra resulting from the interpolation are continuous, but not differentiable at the “ridges” of the structure. This non-differentiability at the “ridges” can be seen even in the  $\chi^2$  space. Optimizers that employ gradient methods (such as MIGRAD [James & Roos, 1975](#)) show some difficulties in some regions of the search space. We have tried to alleviate this problem by beginning the optimization from different starting points. In almost all cases this lead to the same minimum.

In summary, the presented linear n-dimensional interpolator is a very robust and quick way to explore large parameter spaces without having to compute each single point.

Future work will be directed to exploring other n-dimensional interpolators in the astrophysical context.